Flamelet Combustion Modeling and Detached Eddy Simulation of a Model Rocket Combustor with Capacitive Cooling

Wouter Holtslag
Delft University of Technology

Flamelet Combustion Modeling and Detached Eddy Simulation of a Model Rocket Combustor with Capacitive Cooling

For obtaining the degree of Master of Science in Aerospace Engineering at Delft University of Technology

Wouter Holtslag

Prof.dr. S. Hickel

M.Sc. J. Zips
Prof.dr. M. Pfitzner

Contents

List of Figures

List of Tables

Nomenclature

Abbreviations

BFS	Bacwards Facing Step
CFD	Computational Fluid Dynamics
CFL	Courant-Friedrichs-Lewy
CN	Crank-Nicolson time scheme
CV	Control Volume
DDES	Delayed Detached Eddy Simulation
DES	Detached Eddy Simulation
DNS	Direct Numerical Simulation
EVM	Eddy Viscosity Models
filteredNIGMF	filteredNoiseInflowGeneratorMassFlowRate
FV	Finite Volume
HTF	Heat Transfer
IDDES	Improved Delayed Detached Eddy Simulation
LES	Large Eddy Simulation
MSD	Modeled Stress Depletion
OFR	Oxidizer to Fuel Ratio
PDF	Probability Density function
PIMPLE	Pressure Implicit Method for Pressure Linked Equations
PISO	Pressure Implicit Splitting of Operators
RANS	Reynolds Averaged Navier Stokes
RSM	Reynolds Stress Models
SA	Spalart-Allmaras turbulence model
SGS	Sub-Grid Scales
SIMPLE	Semi-Implicit Method for Pressure Linked Equations
WM	Wall Modelling
WMLES	Wall Modelled LES

Symbols

Greek Symbols		
α	Thermal diffusivity	$[m^2/s]$
δ_{ij}	Kronecker delta	$[-]$
Δ	Filter width	$[m]$
Δ_x	Wall parallel grid spacing	$[m]$
ϵ	Dissipation rate	$[m^2/s^3\ ]$
κ	Turbulent kinetic energy	$[m^2/s^2\ ]$
λ	Thermal conductivity	$[W/(m \cdot K\ ]$
ν	Kinematic viscosity	$[m^2/s^1]$
ν_t	Eddy viscosity	$[m^2/s^1]$
$\tilde{\nu}$	Spalart-Allmaras variable	$[m^2/s^1]$
ρ	Density	$[kg/m^3]$
σ	Viscous stress tensor	$[kg/m^3]$
τ_{ij}	Stress tensor	$[kg/ms^2]$
$\boldsymbol{\tau_w}$	Wall shear stress	$[N/m^2]$
ϕ	Generic scalar quantity	$[-]$
χ	Scalar dissipation rate	$[1/s]$
Ψ	Low Reynolds number correction	$[-]$
$\boldsymbol{\omega_t}$	Vorticity at trip point	$[1/s^1]$
ω_c	Chemical production rate	$[mol/(L \cdot s]$
Mathematical Symbols		
∇	Nabla operator	$[-]$
C	Progress variable	$[-]$
C_{DES}	DES model constant	$[-]$
c_p	Specific heat capacity	$[KJ/(kgK)]$
d	Wall distance in SA model	$[m]$
$\tilde{d}$	DES length scale	$[m]$
D	Diffusion coefficient of the scalar dissipation rate	$[-]$
Da	Damköhler number	$[-]$
e	Total specific energy	$[m^2/s^1]$
f_B	Blending function	$[-]$
f_e	Elevating function	$[-]$
g	Gravity	$[m/s^2]$
G	LES filter	$[-]$
h_i	Local cell sizes	$[m]$
h_k	Specific enthalpy of species k	$[J/Kg]$
h_s	Sensible enthalpy	$[J/Kg]$
k	Von Kármán constant	$[-]$
M	Mach number	$[-]$
p	Pressure	$[N/m^2]$
$\boldsymbol{\dot{q}}$	Wall heat flux	$[W/m^2]$
r_d	Delaying DDES length scale	$[m]$
Re	Reynolds number	$[-]$
$\boldsymbol{S}$	Vorticity magnitude	$[1/s]$
$\overline{S}$	Mean shear rate	[1/s]

T	Temperature	$[K]$
u	Velocity	$[m/s]$
u_τ	Friction velocity	$[m/s]$
$\langle \boldsymbol{u} \rangle$	Mean velocity	$[m/s]$
u^+	Non dimensionalized velocity in wall units	$[-]$
$\boldsymbol{u'}$	Velocity fluctuation	$[m/s]$
$\bar{\boldsymbol{u}}$	Filtered velocity	[m/s]
$\tilde{\boldsymbol{u}}$	Favre averaged velocity	[m/s]
$\boldsymbol{u''}$	Subgrid scale velocity	[m/s]
$y+$	Dimensionless wall distance	$[-]$
Y_k	Species mass fraction	$[-]$
Z	Mixture fraction	$[-]$
Z''	Variance of the mixture fraction	$[-]$

CHAPTER 1

Introduction

Hydrocarbon fuels are currently being investigated as a fuel for rocket combustion. The combination of methane and oxygen has been identified as a promising propellant combination. This is due to the fact that it has high specific impulse, high density at common tank pressures, favorable cooling properties and also low cost in production and handling.

Furthermore, the knowledge of combustion and heat transfer at high pressures with methane is not as well developed as with hydrogen. Due to this fact SFB-TR40 has launched a research initiative to gain more knowledge in this field. SFB-TR40 is a research body consisting of multiple universities and companies in Germany. A single element rocket combustor has been constructed and will provide further research with experimental pressure and heat flux data. There is especially interest in the heat transfer near the injector and the wall area.

Reynolds Averaged Navier Stokes (RANS) simulations and Large Eddy Simulations (LES) have been performed at the Institute for Thermodynamics at the Universität der Bundeswehr München. The simulations were done using the open source software OpenFOAM. The simulations showed some considerable differences such as mixing behavior, pressure fields and the wall heat flux. LES better predicted the mixing field and combustion efficiency, while RANS more accurately predicted the wall heat flux. This is due to the fact that resolving the near wall area with LES is computationally very expensive, therefore this was done not sufficiently done.

A promising solution to this issue is to use LES in the channel while modelling the near wall area with RANS. It is sought to combine the good results for the mixing behavior and pressure field of LES with the better wall heat flux results of RANS. Close to the wall RANS allows for high aspect ratio cells which is used to bring down the computational cost of the simulation. The method that will be used is the Detached Eddy Simulation which makes use of introducing a turbulent length scale which is dependent on the wall distance. Using this new length scale a switch is made between using RANS or LES.

The Steady Laminar Flamelet Model (SLFM) will be used to model combustion. This model views turbulent flames as thin, laminar one dimensional flamelets which are embedded into the

turbulent flame. The flamelet is represented by a counterflow diffusion flame. The flame structure is defined by the scalar dissipation rate, this accounts for strain effects and is also linked to the velocity gradients of the flame. The main computational advantage of using the flamelet model is to decouple the chemical structure of the flame from the turbulent flow. This is done by introducing another quantity, the scalar mixture fraction and it is a measure of the amount of fuel in a given mixture.

1.1 Turbulence Simulation

A number of options are available in simulating turbulence. These are RANS, LES and a hybrid method that makes use of both techniques. The three approaches will be explained in the sections below.

1.1.1 Reynolds Averaged Navier Stokes

The main idea behind RANS simulations is to view the Navier Stokes equations in a Reynolds Averaged sense and then solve the equations for the mean solution. The solution is first averaged and then decomposed into a mean value and a fluctuation. The mean value and the fluctuation are then substituted into the Navier Stokes to obtain the RANS equations.

The underlying RANS model in the hybrid approach that will be used in this thesis in the Spalart-Allmaras (SA) model. This is a one equation Eddy Viscosity Model (EVM) that is solved for the eddy viscosity. The SA model is robust and also computationally efficient because it solves just one transport equation. The disadvantages are that it is not very accurate for predicting flow reattachment and free shear layers.

1.1.2 Large Eddy Simulations

With LES the turbulent scales of the flow are filtered and only the larger eddies are computed directly. The smaller scales are modeled on the other hand. Due to the accurately resolving of the flow LES can be much more accurate than RANS, the downside is that it is usually computationally more expensive. An important concept here is the turbulent energy cascade. Here the largest turbulent scales are produced through eternal input, they then pass on energy to the smaller scales through an energy cascade. The smaller scales lose energy through dissipation and exact an energy drain on the larger scales.

1.1.3 Hybrid Methods

The hybrid method makes use of RANS as well as LES. Three methods will be considered here, which are Detached Eddy Simulation (DES), Delayed Detached Eddy Simulation (DDES) and Improved Delayed Detached Eddy Simulation (IDDES). DES was first devised in 1997 by S. Spalart and P. Allmaras. The motivation to develop this method is that resolving the near wall area with LES sometimes results in restrictively high computational costs, especially in high Reynolds number flows. So therefore, a new length scale is introduced to an existing SA RANS model. With this adjustment the model will act as a RANS model when the distance to the wall is smaller than the

grid spacing and as a LES model when it is not.

DDES and IDDES are further developed improvements to the first model. The main issue that was being solved was that DES was displaying some errors in the case of grid refinement. When the grid spacing would be smaller than the boundary layer, the model would unwantedly switch to LES content. To solve this a delaying function was implemented which detects the boundary layer and prevents switching to LES in this case.

1.2 Combustion Simulation

The SLFM will be used to simulate combustion in this thesis. With the flamelet model a turbulent flame is seen as multiple, thin, laminar 1D structures which are present in the flowfield. The assumption of using a flamelet is justified when the Dahmköhler number is large enough, this is the ratio of the turbulence time scale to the chemical time scale. When the chemical time scale is not short enough the turbulent structures have the time to penetrate the flame and destroy it.

The flame structure is connected with only two quantities with the turbulent structure, these are the scalar dissipation rate and the mixture fraction. The former presents strain effects on the flame and defines its structure, the latter is the measure of the amount of fuel in the mixture. The current implementation of the model is such that all the flame structures are already pre-calculated and stored in libraries to save time. During the simulation runs the values for the enthalpy and species fraction are extracted for values of the scalar dissipation rate, the fuel fraction and its variance, which are supplied by the Computationdl Fluid Dynamic (CFD) solver.

1.3 The BKD-9 Combustion Chamber

The combustion chamber that will be simulated is called BKD-9 and it was constructed by TU Munich. It is a square combustion chamber which is approximately 300mm long, its height and width are 12mm. Thermocouples and pressure transducers are placed along chamber manifolds along the combustion chamber for measurements. The chamber has no cooling system, so therefore the burning time is limited to approximately 3 seconds. The wall heat flux is reconstructed through means of an inverse heat conduction problem, so the experimental values that the tests provide are the pressure and the wall heat flux. The measured temperature is then applied to the simulation as a boundary condition.

1.4 Research Objective and Approach

The objective of the research is to correctly predict the wall heat flux and pressure in the BKD-9 combustion chamber. A hybrid RANS/LES method will be used to simulate the turbulence. In essence, this is a method where RANS will be used to model the flow near the wall and LES will be used to resolve the area in the center of the channel. The SLFM will be used to simulate combustion. OpenFOAM will be used as the simulation software. The simulation results will be compared to the available experimental results. Furthermore 4 different grids will be used to quantify the error and uncertainty in simulating the combustion in the combustion chamber. The flow will be analyzed in different sections of the chamber to gain a thorough understanding of the combustion

mechanics.

At first, a general approach for the thesis can be defined. These steps can be found in the points below:

- Building of background knowledge by performing literature study. The fields of research of turbulence and combustion modelling will be investigated.
- Building of the testcases. Two testcases will be performed, a Backwards Facing Step (BFS) and a Heat Transfer (HTF) testcase. These will be done to be gain knowledge and experience in performing CFD simulations.
- Simulating the actual combustion case. As stated before, 4 meshes of different refinement will be used. The flowfield will be analyzed critically and a mesh convergence study will be performed.

1.5 Outline of the thesis

The outline of the thesis is as follows. First the theory behind turbulence modeling will be given. This includes the statement of the governing equations of the flow. Then RANS and LES content will be treated, followed by a description of hybrid methods. Next, the combustion modeling will be treated, a qualitative description of the flamelets will be given along with the theoretical background.

This will be followed by the methodology section. The software package OpenFOAM and its workings will be described. Also the implementation of the flamelet into OpenFOAM and background information on the combustion chamber will be stated. The steps that were taken to properly verify and validate the results of the thesis can be found after this. This includes a description of the testcases and the discussion of the results.

Next, the results of the simulation of the BKD-9 chamber are given. The flame structure is analyzed and a grid study is performed to investigate the effect of refining the mesh has on the final results. Next to this a critical analysis of the flow is performed. This is followed by the conclusions and recommendations section.

CHAPTER 2

Turbulence Modeling

In this section the theory of the turbulence modeling can be found. First the Navier Stokes equations are given. This is followed by the Reynolds Averaged Navier Stokes equations, the Spalart-Allmaras turbulence model and the details of Large Eddy Simulations. Lastly the general idea of the hybrid methods is stated.

2.1 Navier Stokes Equations

The Navier Stokes equations will be used to describe the motion of fluid during this thesis. The Navier Stokes equations consist of a set of 5 equations. Three of these equations describe the conservation of momentum (in three directions), one is for the conservation of mass and the final equation states the conservation of energy.

Conservation of mass:

$$\frac{\partial \rho}{\partial t} + \rho \nabla \cdot \mathbf{u} + \mathbf{u} \cdot \nabla \rho = 0 \tag{2.1}$$

Conservation of momentum:

$$\frac{\partial \rho \mathbf{u}}{\partial t} + \nabla \cdot (\rho \mathbf{u}\mathbf{u}) = -\nabla p + \nabla \cdot (\mu \nabla \mathbf{u}) + f \tag{2.2}$$

Conservation of energy:

$$\frac{\partial \rho e}{\partial t} + \nabla \cdot (\rho \mathbf{u} e) = -\nabla p \mathbf{u} + \nabla \cdot (\mu \mathbf{u} \nabla \mathbf{u}) - \nabla q + f \tag{2.3}$$

Here p is the pressure, ρ is the density, g is the gravity, u is the velocity, e is the total specific energy and ν is the kinematic viscosity. Due to the fact that the research will be performed in a high Mach (M) regime, with flows exceeding $M = 0.3$, the compressible Navier Stokes equation will be used. Furthermore the following assumptions are used in deriving the compressible Navier Stokes Equations [16].

- Galilean Invariance, which mean that the laws of motion are the same in all inertial frames

- The fluid is assumed to be isotropic
- That stress is linear in the elasticity tensor

With these assumptions, the compressible most general Navier Stokes equation can be derived [16]:

$$\frac{\partial \mathbf{u}}{\partial t} + \mathbf{u} \cdot \nabla \mathbf{u} = -\frac{1}{\rho}\nabla \hat{p} + \nu \nabla^2 \mathbf{u} + \frac{1}{3}\nu \nabla(\nabla \cdot \mathbf{u}) + g \tag{2.4}$$

Here p is the pressure, ρ is the density, g is the gravity, u is the velocity and ν is the kinematic viscosity. Furthermore, ∇ is called the Nabla operator and is defined in terms of partial operators as follows:

$$\nabla = \Big(\frac{\partial}{\partial x_1}, ..., \frac{\partial}{\partial x_n}\Big) \tag{2.5}$$

2.2 Reynolds Averaged Navier Stokes

The idea with RANS is to view the Navier Stokes equations in a Reynolds averaged sense and solve the equations for the steady mean solution. By doing this only the most important flow properties are captured. First the solution is averaged in Eq. 2.6 and then decomposed into a mean value and a fluctuation in Eq. 2.7:

$$\langle \mathbf{u}_i \rangle = \frac{1}{N}\sum_{\mu=1}^{N} \mathbf{u}_i|_\mu \tag{2.6}$$

$$\mathbf{u}_i = \langle \mathbf{u}_i \rangle + \mathbf{u}_i^{'} \tag{2.7}$$

The mean value $\langle \mathbf{u}_i \rangle$ and fluctuation $\mathbf{u}_i^{'}$ are then substituted into the Navier Stokes equation to obtain the RANS equations. In Fig. 2.2.1 the averaging of the solution over a flat plate can be visualized. The difference between the mean and instantaneous flow can be seen.

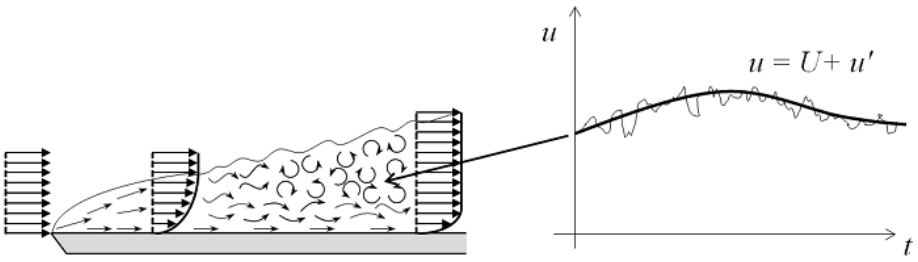

Figure 2.2.1: Time averaged solution of a fluctuating flow [1].

However with the Reynolds Averaged Navier Stokes equations there is still a closure problem due to the Reynolds stress tensor. The Reynolds stress is the component of the total stress tensor

that is obtained after averaging the Navier Stokes equations to account for the the turbulent fluctuations in fluid momentum. The task of the RANS models is to provide approximations for this stress tensor. There are two types of turbulence methods to do this. These are the EVM and the Reynolds Stress Models (RSM).

EVM are based on the observation that turbulence leads to momentum exchange. The deviator of the Reynolds stress tensor is assumed to be proportional to the mean shear rate and the proportionality factor is the eddy viscosity ν_t. The eddy viscosity is not a material property like the kinematic viscosity ν but it is a field property. RSM attempt to directly solve the model transport equations for every component of the unknown Reynolds stress tensor. In order to do this approximations of higher order correlations need to be made to simplify and close the transport equation.

2.2.1 Spalart-Allmaras Model

The RANS model that will be used with IDDES is the SA model, this is a one equation EVM that is solved for the eddy viscosity, ν_t [17]. The SA model is a robust and computationally efficient model because it only needs to solve one transport equation. On the downside it is not very accurate for flow reattachment and free shear layers. It is defined as follows:

$$\nu_t = \tilde{\nu} f_{v1} \tag{2.8}$$

Here $\tilde{\nu}$ is the Spalart-Allmaras variable, a viscosity like quantity. The transport equation is:

$$\frac{D\tilde{\nu}}{Dt} = c_{b1}[1 - f_{t2}]\tilde{S}\tilde{\nu} + \frac{1}{\sigma}[\nabla((\nu + \tilde{\nu})\nabla\tilde{\nu}) + c_{b2}(\nabla\tilde{\nu}^2] - [c_{w1}f_1 - \frac{c_{b1}}{k^2}f_{t2}][\frac{\tilde{\nu}}{d}]^2 + f_{t1}\Delta U^2 \tag{2.9}$$

In this equation S is defined as the magnitude of the vorticity:

$$\tilde{S} \equiv S + \frac{\tilde{\nu}}{k^2 v^2} f_{v2}, \quad f_{v2} = 1 - \frac{\chi}{1 + \chi f_{v1}} \tag{2.10}$$

Here d is the distance to the closest wall and the function f_w is:

$$f_w = g[\frac{1 + c_{w3}^6}{g^6 c_{w3}^6}]^{\frac{1}{6}}, \quad g = r + c_{w2}(r^6 + r), \quad r \equiv \frac{\tilde{\nu}}{\tilde{S}k^2 d^2} \tag{2.11}$$

The wall boundary for $\tilde{\nu}$ is zero at the walls. The f_{t2} function is:

$$f_{t2} = c_{t3} exp(-c_{t4}\chi^2) \tag{2.12}$$

f_{t1} is the trip function and is defined in Eq. 2.13. In this equation d_t is the distance from the field point to the wall. ω_t is the wall vorticity at the trip point, Δ is the difference in velocity in the field point and at the location of the trip. Furthermore, $g_t \equiv min(0.1, \Delta/\omega_t \Delta x)$.

$$f_{t1} = c_{t1} g_t exp(-c_{t2}\frac{\omega_t^2}{\Delta U^2}[d^2 + g_t^2 d_t^2]) \tag{2.13}$$

The constants that are used in this turbulence model are $c_{b1} = 0.1355$, $\sigma = 2/3$, $c_{b2} = 0.622$, $k = 0.41$, $c_{w1} = c_{b1}/k^2 + (1 + c_{b1})/\sigma$, $c_{w2} = 0.3$, $c_{w3} = 2$, $c_{v1} = 7.1$, $c_{11} = 1$, $c_{t2} = 2$, $c_{t3} = 1.1$, $c_{t4} = 2$. Lastly, turbulent heat transfer obeys a turbulent Prandtl number of 0.9.

2.3 Large Eddy Simulation

In this section the concept of LES will be described. LES was originally developed in the 1960's as a method to predict atmospheric flows. Since then it has grown to become one of the most promising and successful methods in computing turbulent flows. This method has become more successful also due to an increase in computing power over the years [18]. As stated before, with RANS the entire flow is modeled and solved for the average quantities. With LES however the turbulent scales are filtered and only the large scale motions, or eddies, of the turbulent flow are computed directly and the smaller Sub-Grid Scales (SGS) are modeled. In Fig. 2.3.1 the difference between the filtered velocity and the instantaneous velocity can be observed [18]. Here the mean flow is indicated with $\bar{U}$, the instantaneous velocity with U, the mean fluctuation with $\bar{u}'$, the instantaneous fluctuation with u' and the cell size is Δ.

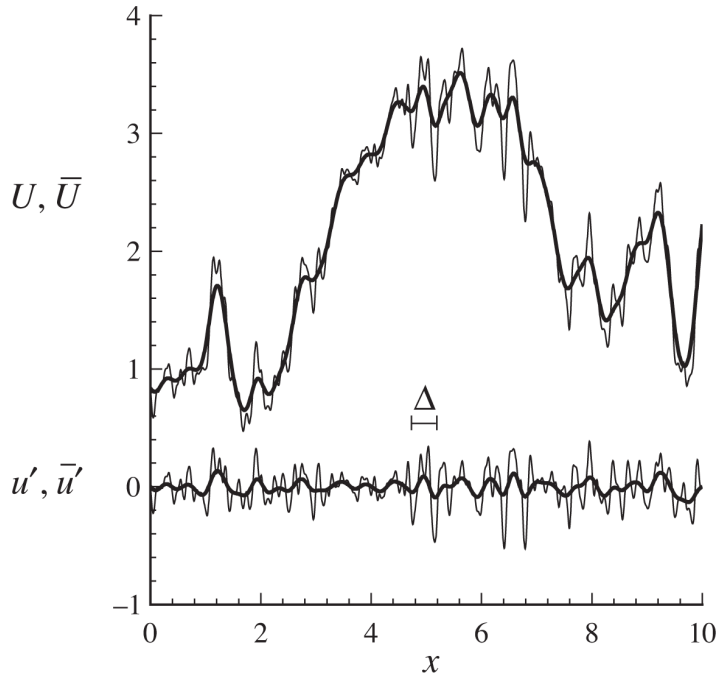

Figure 2.3.1: The difference between the filtered and instantaneous velocity [2].

As a consequence, LES can be much more accurate than RANS. The largest scales contain most of the energy in the flow. Therefore they are responsible for most of the momentum transfer and mixing. The largest scales depend strongly on geometry and are more difficult to model, while the smaller scales are easier to model. A key concept in this is the turbulence energy cascade, this is visualized in Fig. 2.3.2 where the turbulent energy is plotted against the wave number. As indicated in the figure, the largest turbulent scales are produced through external energy input. These larger scales then pass on energy to the smaller scales through an energy cascade. The smaller scales lose energy through dissipation and furthermore they exact an energy drain on the larger scales.

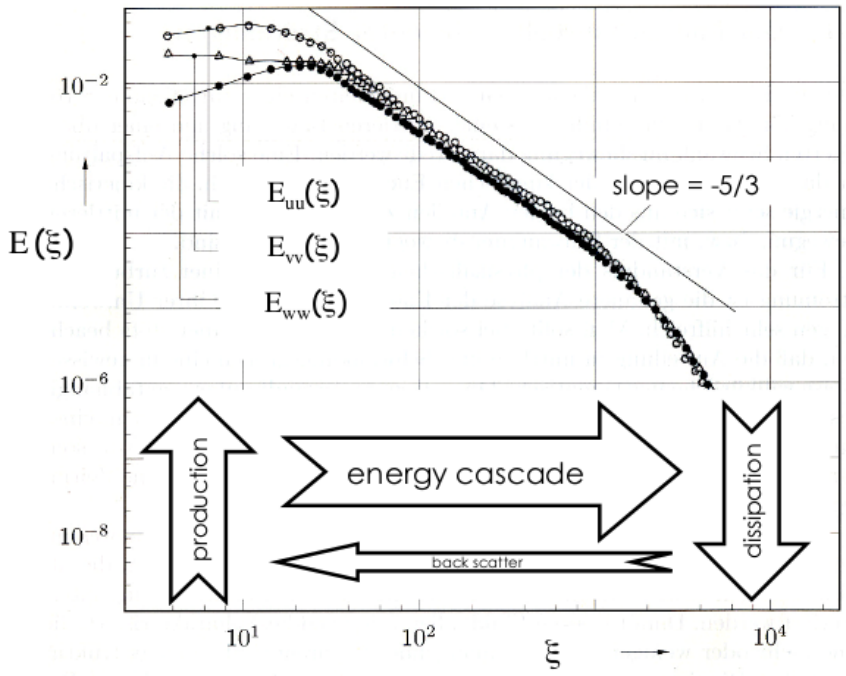

Figure 2.3.2: The turbulent energy cascade [3].

This scale separation of the large and small scales is done by filtering. Filtering can be done with a spatial filter where Δ, the filter width, can be taken as the grid width. This filter will then capture all the large scales and remove the smaller scales for modeling. An example of such a filter function is shown in Fig. 2.3.3.

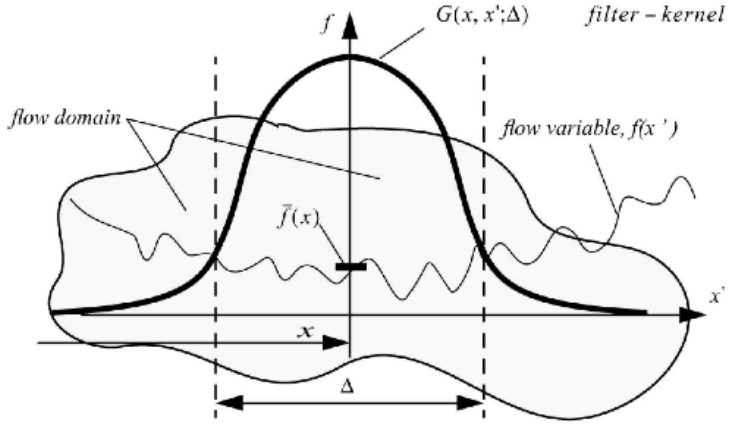

Figure 2.3.3: Representation of an arbitrary filter function [4].

The filtered velocity, $\bar{\mathbf{u}}_i$ is obtained as follows with the filter G:

$$\bar{\mathbf{u}}_i = G * u_i = \int_{\infty} \infty G(x - x')u_i(x')dx' \tag{2.14}$$

Here the filter function is defined in Eq. 2.15. This filtering operation yields the decomposition of the velocity into the filtered velocity $\bar{\mathbf{u}}_i$ and the sub-filtered velocity $\mathbf{u}_i''$, as seen below in Eq. 2.16.

$$\int_{\infty}^{\infty} G(x - x')dx' = 1 \tag{2.15}$$

$$\mathbf{u}_i = \bar{\mathbf{u}}_i + \mathbf{u}_i'' \tag{2.16}$$

Furthermore, OpenFOAM uses the implicit tophat filter for these operations. This type of filter is simply an average over a rectangular area. The top hat filter is defined as:

$$G(x, \Delta) = \begin{cases} \frac{1}{\Delta}, & \text{if } |x'| \leq \frac{\Delta}{2}. \\ 0, & \text{otherwise.} \end{cases} \tag{2.17}$$

Favre density weighted filtering operation, which is typical for filtered compressible LES, $\tilde{f} = \overline{\rho f}/\bar{\rho}$. The governing equations for filtered compressible LES are stated below:

$$\frac{\partial \bar{\rho}}{\partial t} + \bar{\rho}\nabla \cdot \tilde{\mathbf{u}} + \tilde{\mathbf{u}} \cdot \nabla\rho = 0 \tag{2.18}$$

$$\frac{\partial \bar{\rho}\tilde{\mathbf{u}}}{\partial t} + \nabla \cdot (\bar{\rho}\tilde{\mathbf{u}}\tilde{\mathbf{u}}) + \nabla\bar{p} = \nabla \cdot \tilde{\sigma} - \rho\nabla \cdot \tau_{ij} \tag{2.19}$$

$$\frac{\partial \overline{\rho e}}{\partial t} + \nabla[(\overline{\rho e} + \bar{p}\tilde{\mathbf{u}}] = -\nabla\bar{q} + \nabla(\tilde{\sigma}\tilde{\mathbf{u}}) + 0.5\nabla\bar{\rho}(\overline{\mathbf{uuu}} - \tilde{\mathbf{u}}\tilde{\mathbf{u}}\tilde{\mathbf{u}} - \tau_{kk}\tilde{\mathbf{u}}) \tag{2.20}$$

Here τ_{ij} is the subgrid-scale stress tensor and $\tilde{\sigma}$ the viscous stress tensor. τ_{ij} is defined as:

$$\tau_{ij} = \overline{\mathbf{uu}} - \bar{\mathbf{u}}\bar{\mathbf{u}} \tag{2.21}$$

As stated previously, the SA model that will be used is an EVM, where the deviator for the Reynolds stress is assumed to proportional to the mean shear rate $\overline{S_{ij}}$. Consequently the stress tensor can be written as:

$$\tau_{ij} = \frac{1}{3}\tau_{kk}\delta_{ij} + \nu_{_{SGS}}\overline{S_{ij}} \tag{2.22}$$

2.4 Hybrid Turbulence Modeling

In this section the theory behind the hybrid methods DES, DDES and IDDES will be explained. First the workings of the base model including what triggers the switch between RANS and LES content will be explained. Each subsequent version is seen as an upgrade of the previous version and is designed to resolve certain issues that played during the use of the hybrid methods. First the issues themselves and then the theory behind the improvements will be stated.

2.4.1 DES

As mentioned before, using LES to accurately resolve the near wall area requires restrictively high computational costs, especially in high Reynolds number flows. This was one of the main motivations to develop DES. For its RANS content it uses the SA model, which was created by the same authors [19]. The DES model is formulated as follows.

The SA model uses a destruction term for its eddy viscosity which is proportional to d, the distance to the closest wall. When this is balanced with the production terms then this term will adjust the eddy viscosity to scale with the local deformation rate S. Next to this, the Smagorinsky model scales its SGS eddy viscosity with S and the grid spacing Δ. Therefore if in the SA model the d is replaced with a length that is proportional to Δ a SGS model is obtained. This length scale is defined as:

$$\tilde{d} \equiv min(d, C_{DES}\Delta) \tag{2.23}$$

With this adjustment the model will acts as the SA model when the distance to the wall is smaller than the grid spacing, Δ, and as a SGS model when the wall distance is larger than the grid spacing. Basically this means that the model will switch to RANS mode when it is close to the wall and to LES mode away from the wall. The adjustable model constant C_{DES} is set by experimenting and needs to perform well in different types of flows. Just like LES, DES will act like DNS in the case of extreme grid refinement.

One of the first concerns that the authors had was that the model is dependent on defining the eddy viscosity with the wall distance and not all RANS model use this quantity in their calculation. This means that initially not every RANS model would be suited to be used in such a manner. Also the authors saw that one issue might be troublesome with the use of their model, even though they did not expect it to become a major issue as it did. This occurs when the grid spacing is of the same magnitude as the boundary layer. Furthermore the authors expressed the desire to stay in RANS mode while the wall normal spacing was decreased. This meant that the model should not unwantedly switch to RANS mode during a grid refinement process.

Next to this it was found while writing the DES paper that further problems arose with severe grid refinement. It is stated that ideally refinement will not take place to scales which are a significantly smaller than the dominant eddies. However, grid refinement sometimes leads to grids which are unnecessarily refined. It was found that if this was the case the eddy viscosity would be drastically lowered. Furthermore, the friction coefficient drops and the H factor changes.

2.4.2 DDES

In this section the literature of DDES will be discussed. The use of DES sometimes displayed incorrect behavior and DDES was formulated in response to this. This can happen in thick boundary layers and shallow separation regions. Specifically, wrong behavior can be seen when the grid spacing parallel to the wall becomes less than the thickness of the boundary layer [5].

The mixing length is defined so that if if the largest cell grid size is smaller than the distance to the wall, the model will switch to LES content. Therefore, if the cell grid spacing is smaller

than the thickness of the boundary layer the switch will happen inside of the boundary layer. This premature switch leads to a lowering of the eddy viscosity. This is due to the fact that the resolved Reynolds stresses from the LES model have not yet replaced the modeled Reynolds stresses which were computed by the RANS model. The Reynolds stresses are the component in the total stress tensor which account for the fluid fluctuations in momentum transfer. These reduced stresses can lead to a reduction of skin friction and premature separation. A modification is made by the authors to DES to shield the model from switching from RANS to LES inside the boundary layer. In the following figure the issue with ambiguous grids is made clearer.

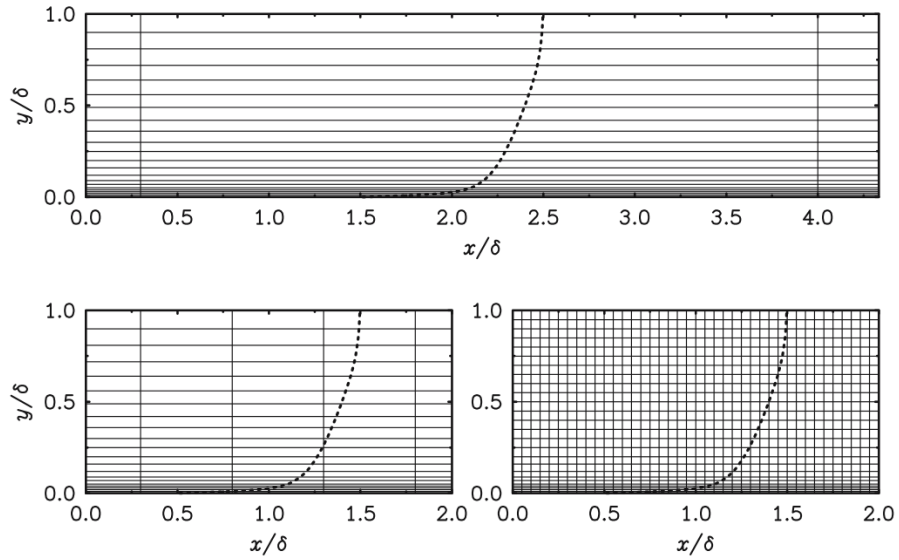

Figure 2.4.1: Gridding inside of a boundary layer [5].

In the top figure a typical grid is shown that is used for a hybrid RANS/LES model with a thin boundary layer, this is called a type I grid. Here the wall parallel spacing Δ_x exceeds the thickness of the boundary layer, therefore LES content is bypassed in this region. The bottom right grid, a type III grid, has a grid spacing which are all smaller than the boundary layer. This model will function as a LES model over the largest part of the boundary layer and only switch to the RANS model very close to the wall [5]. This type of gridding is usually done with Wall Modelled LES (WMLES). In the 1970's LES was used in combination with wall models, but moved away from this approach once computing power allowed better resolution of the near wall area. However, with current rising demands for high Reynolds number flows WMLES approaches are being explored again.

The bottom left grid is of type II and is a so called 'ambiguous grid'. Here the DES limiter is activated roughly in the upper two thirds of the boundary layer because the model will switch to LES as soon as the distance to the wall is larger than the cell dimensions. The resolution is not fine enough to support LES content at this location. As a consequence, the DES limiter will reduce the eddy viscosity and the modeled Reynolds stress without any sizeable resolved stress to restore this balance [5].

This phenomenon is called Modeled Stress Depletion (MSD). This might occur if the grid is refined starting with a type I grid. Furthermore, a grid over an airfoil might by a type I grid at a certain angle of attack , but will change to a type III grid at another angle of attack. This is due to the changing thickness of the boundary layer. In a severe case MSD can lead to Grid Induced Separation (GIS). This issue of MSD is a problem of any hybrid method. Multiple solutions have been tried out for other hybrid methods, which included making the domain zonal or using the aspect ration of the cells, but this was not very successful [5]. The solution that was used for DDES was to use shielding functions as was already proposed by Menter and Kuntz [20]. Here two shielding functions, F1 and F2, are used to identify the boundary and subsequently prevent a switch to LES inside of this area. These shielding functions have a value of 1 in the boundary layer and rapidly fall to 0 near the edge.

Since the SA model does not use an internal length scale another parameter is introduced. It is based on the already available parameter r, which is the ratio of the model length scale to the wall distance. The relation is as follows.

$$r_d \equiv \frac{\nu_t + \nu}{\sqrt{\mathbf{u}_{i,j}\mathbf{u}_{i,j}}k^2d^2} \tag{2.24}$$

Here ν_t is the kinematic eddy viscosity, ν is the kinematic viscosity, $\mathbf{u}_{i,j}$ are the velocity components, k is the von Kármán constant and d is the distance to the wall. This parameter will equal 1 in the logarithmic layer and will go to 0 near the edge of the boundary layer.

The parameter r_d is used in the following equation.

$$f_d \equiv 1 - tanh([8r_d]^3) \tag{2.25}$$

This function is formulated such that it has a value of 1 in the LES region, where r_d is many times smaller than 1, and 0 at all other locations. In order for the delaying function f_d to be effective, the DES length scale needs to be redefined.

$$\tilde{d} \equiv d - f_d max(0, d - C_{DES}\Delta) \tag{2.26}$$

When f_d is zero then $\tilde{d} = d$ and this will yield RANS content. If it is 1 then the original formulation for DES will be obtained, $\tilde{d} \equiv min(d, C_{DES}\Delta)$. With these adjustments the DES length scale does not only depend on the grid, it now also depends on the eddy viscosity field. In effect the function can refuse to go into LES if it senses that it is inside the BL. However if separation does arise then it does switch to LES and this is an essential part of the function.

Furthermore, switching between the 2 modes happens more abruptly, which makes the grey area between these two modes more narrow. DDES is also designed to have LES content grow more quickly compared to DES.

2.4.3 IDDES

The latest version of DES is IDDES. This model can give two different responses, depending on whether the inflow conditions are turbulent or not. If there are no turbulent inflow conditions then DDES is active. If there are turbulent inflow conditions then the WMLES branch of the model becomes active. The coordination of these two branches is done with a blending function [6].

When running simulations that produce RANS results as well as LES content, two different logarithmic layers are produced. The inner logarithmic layer which is the result of the RANS computations and the outer layer which is the result of the LES content. In turns out that the velocity profiles of log layers are mismatched, which results in a underprediction of the skin friction of 10 to 15 percent. In order to counter the problem with logarithmic layer mismatch a new definition for the subgrid length scale is proposed. Previously a definition was used that was just dependent on the cell sizes, however this was presenting problems.

The Smagorinsky constant ideally has different values for different types of flow. This means that using a single model constant for the entire flow cannot be correct and this motivated the search for a different definition for the sub grid length scale. Due to the presence of wall proximity effects it was decided to include the wall distance in the definition for the sub grid length scale. Three definitions for the subgrid length scale are being used. These regions are the free stream, close to the wall and the region in between these two. It will have the following form:

$$\Delta = f(h_x, h_y, h_z, d_w) \tag{2.27}$$

Here h_x, h_y, h_z are the local streamwise, wall normal and lateral cell sizes. d_w is the distance to the wall. First of all, away from the wall the length scale remains unchanged compared to the initial DES definition and is as follows.

$$\Delta_{free} = h_{max} \equiv max\{h_x, h_y, h_z\} \tag{2.28}$$

Very close to the wall the length scale should not decrease as drastically as the cell size in the wall normal direction. Therefore, it is only dependent on the wall parallel directions.

$$\Delta_{wall} = \Delta(h_x h_z) \tag{2.29}$$

Then there is a third definition for the area between these two limiting cases of h_{max} and h_{min} and will vary linearly with the wall distance, this yields:

$$\Delta = min\{max[C_w d_w, C_w h_{max}, hwn], \Delta_{max}\} \tag{2.30}$$

Here h_{wn} is the cell step in the wall normal direction and C_w is an empirical constant. The value was set to 0.15 based on a channel flow with wall resolved LES and a SGS model.

In the figure which can be found below, the two types of variation of the subgrid length scale are shown next to the classical definition of the subgrid length scale, which is the cube root of the cell volume. These values are normalized by the maximum grid step.

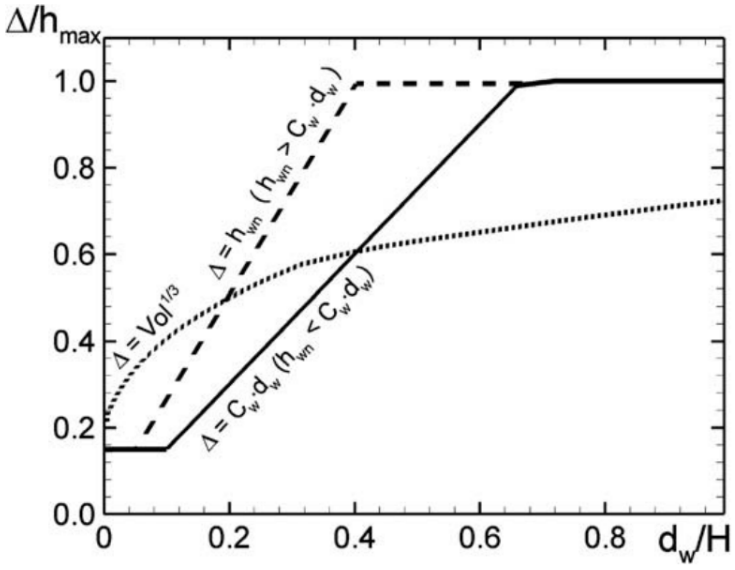

Figure 2.4.2: The two types of subgrid length scale variation and the classical cube root definition [6].

The solid line represents the variation in subgrid length scale if $h_{wn} \leq C_w d_w$. The length scale in this case will remain constant and equal to $C_w h_{max}$ as long as $d_w < h_{max}$. As soon as $d_w > h_{max}$, Δ will grow linearly with $C_w d_w$, until the value of h_{max} is reached and then it will remain constant. The dashed line indicates the variation Δ will have in the case of strong cell to cell stretching. This is used in order to prevent a violation of the physical constraint $\Delta > h_{min}$. Initially the subgrid length remain constant as long as $h_{wn} < C_w h_{max}$ and is equal to $C_w h_{max}$. The linear segment grows with a higher rate than C_w until it reaches the value of h_{max} and remains constant. This extra branch is not desirable, but if a stretching is used that is acceptable for LES then this will not lead to disaster.

DDES branch of IDDES

This branch of IDDES will only become active if there are turbulent inflow conditions and is responsible for the DDES behavior of the model. Recalling the DDES length scale, it can be stated as:

$$l_{DDES} = l_{RANS} - f_d max\{0, (l_{RANS} - l_{DDES})\} \tag{2.31}$$

In order to have a smoothly functioning hybrid model, the l_{DDES} needs to be substituted into the used RANS model instead of the l_{RANS}. The l_{LES}, or LES length scale, is defined as follows.

$$l_{LES} = C_{DES} \Psi \Delta \tag{2.32}$$

As before, C_{DES} is the model constant, Δ is the subgrid length scale and Ψ is a new low Reynolds number correction. This term is introduced in order to compensate for the activation of

low Reynolds number terms of the background RANS model while the model is in LES mode. For the SA model this function reads as:

$$\Psi = min[10^2, \frac{1 - \frac{c_{b1}}{c_{w1}k^2 f_W^*}[f_{t2} + (1 - f_{t2})f_{v1}]}{f_{v1} max(10^{-10}, 1 - f_{t2})}] \tag{2.33}$$

Here, all the quantities are the same as with the SA RANS model, except for f_W^*, which is 0.424.

WMLES branch of IDDES

This branch is only to be active when the inflow conditions are turbulent. Furthermore it is designed to be used when the grid is fine enough to resolve boundary layer dominant eddies. A new length scale is introduced to provide a seamless hybrid RANS/LES model and is defined as

$$l_{WMLES} = f_B(1 + f_e)l_{RANS} + (1 - f_B)l_{LES} \tag{2.34}$$

The length scales l_{WMLES} and l_{RANS} are the same as with the DDES formulation. f_B is an empirical blending function and is dependent on d_w/h_{max}. The function is defined as:

$$f_B = min\{2exp(-9\alpha^2), 1.0\}, \quad \alpha = 0.25 - d_w/h_{max} \tag{2.35}$$

The purpose of this function is to provide rapid switching between RANS and LES mode, within the range of wall distance of $0.5h_{max} < d_w < h_{max}$. It varies from 1 in RANS mode to 0 in LES mode.

The second function, the elevating function f_e, is empirical as well and is designed to combat log layer mismatch. Specifically it is meant to prevent excessive reduction of the RANS Reynolds stresses which have been observed in the area where the RANS and LES region interact. This function should be nearly zero and therefore passive in two specific cases:

- In the case that the resolution of the grid is good enough to perform wall resolved LES. This means that the RANS/LES interface is located at a $y+ < 15 - 20$ and so when the Reynolds stresses near the interface can be neglected.
- When the final IDDES model acts as the background RANS model.

The empirical function f_e reads as:

$$f_e = max\{f_{e1} - 1), 0\}\Psi f_{e2} \tag{2.36}$$

The function f_{e1} is defined as:

$$f_{e1}(d_w/h_{max}) = \begin{cases} 2exp(-11.09\alpha^2), & \text{if } \alpha > 0. \\ 2exp(-9\alpha^2), & \text{if } \alpha \leq 0. \end{cases} \tag{2.37}$$

This function is not dependent on the grid and provides an elevating component for the RANS part of the WMLES length scale. This elevating function is visualized in Fig 2.4.3. It can be seen that it has the same value as f_B when this is lower than 1, which means that the model is in the

RANS/LES switching region. However with decreasing wall distance, f_{e1} increases in magnitude and returns to 1 at the wall.

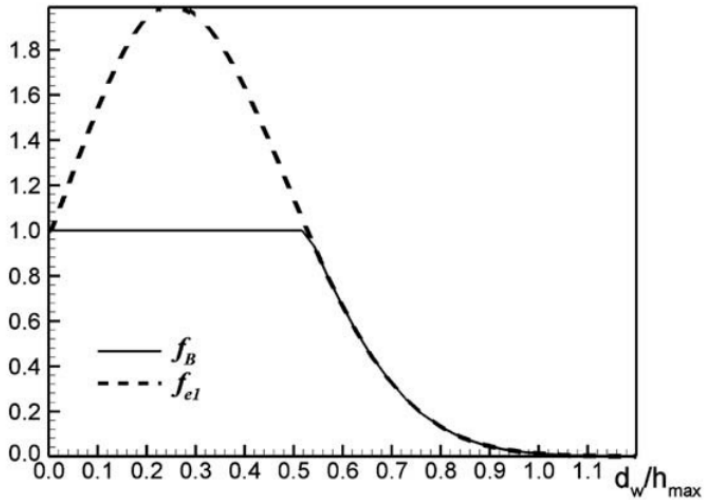

Figure 2.4.3: The profiles of the functions f_B and f_{e1} in a channel flow [6].

The function f_{e2} from Eq. 2.36 is defined as:

$$f_{e2} = 1 - max\{f_t, f_l\} \tag{2.38}$$

The two functions f_t and f_l are used to regulate the intensity with which the RANS component is elevated. These functions are formulated as follows.

$$f_t = tanh[(c_t^2 r_{dt})^3], \quad f_l = tanh[(c_l^2 r_{dl})^{10}] \tag{2.39}$$

In Eq. 2.39 the parameters r_{dt} and r_{dl} are analogues of the previously defined Eq. 2.24. Next to this c_t and c_l are model constants which are dependent on the background RANS model that is used. These constants need to be adjusted in such a way that f_{e2} is nearly zero when either r_{dt} or r_{dl} is close to unity. r_{dt} is close to 1 in the logarithmic part of the boundary layer, just like r_d. Next to this, r_{dl} is close to 1 in the laminar sublayer. When these parameters are 1 then subsequently f_{e2} and f_e are zero where it needs to be zero, e.g. when the IDDES model is in RANS mode.

The blending of the DDES and WMLES branches

By modifying the DDES length scale that was stated in Eq. 2.31 it becomes appropriate to provide adequate blending depending on the inflow conditions. The new definition for the DDES length scale is:

$$\tilde{l}_{DDES} = \tilde{f}_d l_{RANS} + (1 - \tilde{f}_d) l_{LES}) \tag{2.40}$$

The blending function is defined as:

$$\tilde{f}_d = max\{(1 - f_{dt}) f_b\}, \quad f_{dt} = 1 - tanh[(8 r_{dt})^3] \tag{2.41}$$

With Eq. 2.40 the IDDES length scale can be formulated which will use both DDES and WMLES length scales.

$$l_{hyb} = \tilde{f}_d(1 + f_e)l_{RANS} + (1 - \tilde{f}_d)l_{LES})\} \tag{2.42}$$

In the cases where there is turbulent inflow conditions, then $r_{dt} \ll 1$, which in turn results in f_{dt} of close to unity. This leads to $\tilde{f}_d$ equalling f_b and so $l_{hyb} = l_{WMLES}$ is obtained. If there are no turbulent inflow conditions then f_e will reduce to 0 and Eq. 3.12 will yield $l_{hyb} = l_{DDES}$.

2.5 Wall Functions

Next to this Wall Modeling will be used during this research. The idea with wall models is that it is too expensive to resolve the flow near the wall with LES. This technique relies on strong empiricism, but this area of the flow is generally well known. It uses these empirical laws to predict a logarithmic velocity profile near the wall. The most basic and rudimentary requirement of wall functions is to accurately predict the skin friction [8]. The wall shear stress is then used to relate to the outer velocity, which is then used by the LES model.

Generally speaking there are two types of Wall Functions [7], which are equilibrium laws and zonal models. Equilibrium laws assume that the dynamics of the wall layer are universal and also that a general law of the wall exists, as long as the equations used are averaged over a large enough area. Using this general law of the wall, the wall stress is then computed and applied some distance away from the wall. These type of equilibrium laws have been applied with success for simple flows, however they run into difficulties when they are applied to complex geometries or fully unstructured grids.

In Fig. 2.5.1, a universal velocity profile close to the wall can be observed. The fact that distinctive sublayers can be seen in this area is used by equilibrium laws to formulate a generalized law for the wall. Closest to the wall the laminar sublayer, or viscous sublayer, can be seen. This is a region close to the wall, which extends up to $y^+ = 10$. y^+ is the dimensionless wall distance and is a tool that can be used to obtain the most desired grid spacing for a certain flow. Next to this, a buffer layer exists between this and the turbulent zone, or the logarithmic region. The logarithmic region has a different velocity profile which is characterized by a logarithmic function

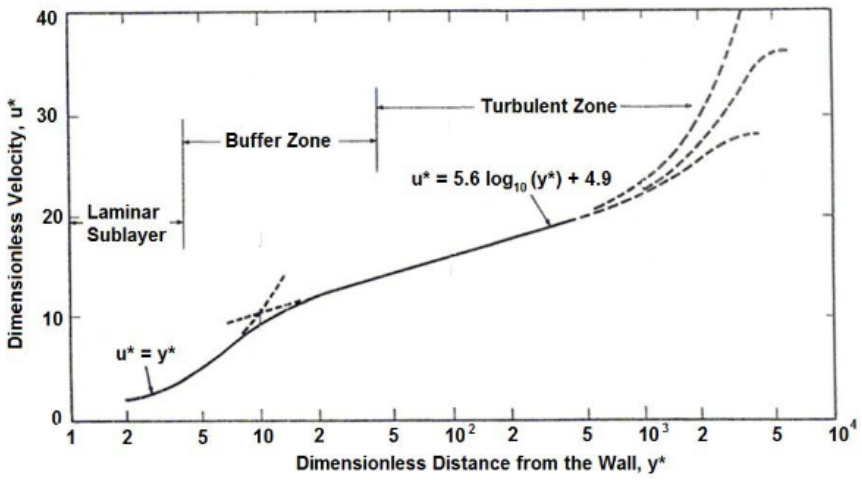

Figure 2.5.1: A universal velocity profile close to the wall [7].

In this figure the dimensionless velocity is used, this is the velocity divided by the friction velocity. This can be seen seen in Eq. 2.43. The friction velocity is a term used for non-dimensionalizing the velocity and also used for calculating y^+. τ_w is the wall shear stress. Another notation for $_*$ is u_τ.

$$u^+ = \frac{u}{u_*} \quad , u_* = \sqrt{\frac{\tau_w}{\rho}} \tag{2.43}$$

Next to this there are zonal approaches, which are essentially hybrid RANS/LES methods that are solving the filtered equations away from the wall and in the near wall region the RANS equations. As opposed to equilibrium laws, a field of equations are used instead of just a single formula for the stress and the velocity at the edge of the wall layer. One of these methods is based on the DES model and uses a single grid, only the turbulence model changes from one location to the next.

One of the issues that the use of Wall Functions or DES runs into is that, as stated in Sec. 2.4.3, the logarithmic layers of the RANS and LES mismatch at the point where they meet. In the figure below an example for such a logarithmic layer mismatch can be found.

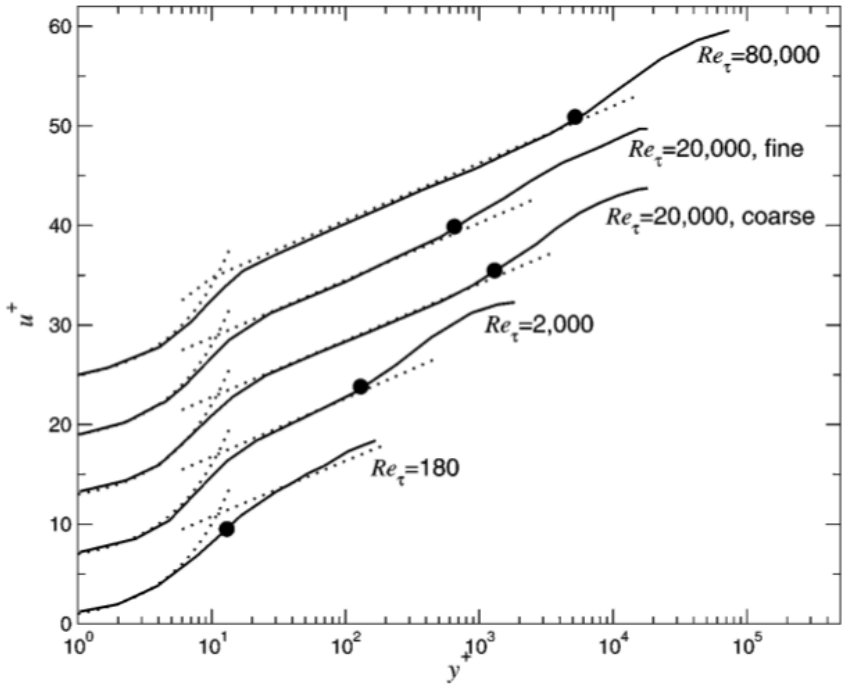

Figure 2.5.2: Mean velocities are shown in a channel flow for different Reynolds numbers. A bullet shows the location of the intersect between the RANS and LES region [8].

As can be seen in Fig. 2.5.2, the velocity gradient at the point where LES content starts is too high. This error is furthermore reflected in the skin friction coefficient, which can be underpredicted by up to fifteen percent [7]. The reason that this happens is that in the RANS region the length scales are large due to the large turbulent viscosity [21] and the resolved velocity fluctuations are weak. In the ideal case when moving away from the wall, into the LES region away from RANS content, the small scale velocity fluctuations should be quickly recovered. In the LES region the resolved velocity fluctuations should be dominant. However, the velocity field of the RANS area is affecting the velocity field at the bottom of the LES zone. As a result of this, the velocity fluctuations in this area are artificially reduced and their length scales are too large. Therefore the resolved stress is underpredicted. However, the global balance of momentum needs to be conserved, this requires the modeled and viscous stress terms to have larger values. Since these stress terms are proportional to the velocity gradient, this will be overpredicted.

In this way the interaction between RANS and LES has led to an unphysical buffer layer. A number of solutions have been tried to solve this. Grid refinement and changing the model constant of the DES model has not solved the problem, it only changed the location of the incorrect intercept. With standard DES methods this problem is not so apparent because the entire boundary layer is modeled with RANS, however when DES methods are used in a wall function fashion then this will become a problem.

CHAPTER 3

Combustion Modeling

In this section the theory behind combustion modeling can be found. First the general idea behind laminar flamelets is explained. Then the equations that govern the laminar flamelets are given, followed by a quick recap of the assumptions that are made while using the flamelets.

3.1 Laminar Flamelets

The definition of a flamelet is: 'Flamelets are thin reactive-diffusive layers embedded within an otherwise nonreacting turbulent flow field' [22]. The flamelet model considers a turbulent flame as an ensemble of thin, laminar, locally one dimensional flamelets which are embedded into the turbulent flame. A counterflow diffusion flame is a common way to represent a flamelet in turbulent flow. In Fig. 3.1.1 a counterflow diffusion flame is visualized. Two opposing fuel and oxidizer jets can be observed. The distance between the jets can be decreased, this will strain the flame and as a consequence it will depart from chemical equilibrium until it is extinguished. The flame structure is defined by the scalar dissipation rate, this term accounts for strain effects and is linked to the velocity structure of the flame. In terms of computational efficiency, the main advantage of using the flamelet model is that the turbulent flow is decoupled from the chemical structure, this is done with the mixture fraction as will be shown later.

The assumption of viewing a turbulent flame as a flamelet is justified in the case that the Dahmköhler number, Da, is large enough. This is the ratio of the residence time to the chemical time in a reacting system [22], or the turbulent time scale to the chemical timse scale. This means that for large Dahmköhler numbers the reaction times become very fast. Since the chemical time scale of the reaction is very short in this case, the chemistry is most active in a thin layer, which is also known as the fuel consumption or inner layer. If this layer is thin enough compared to the size of a Kolmogorov Eddy, which is the size of the smallest eddy in a turbulent flow, the flame is embedded within such an eddy and the assumption of flamelets is justified. However, if the Kolmogorov eddies are smaller than the inner layer of the flame then these eddies can penetrate the flame and destroy it [10].

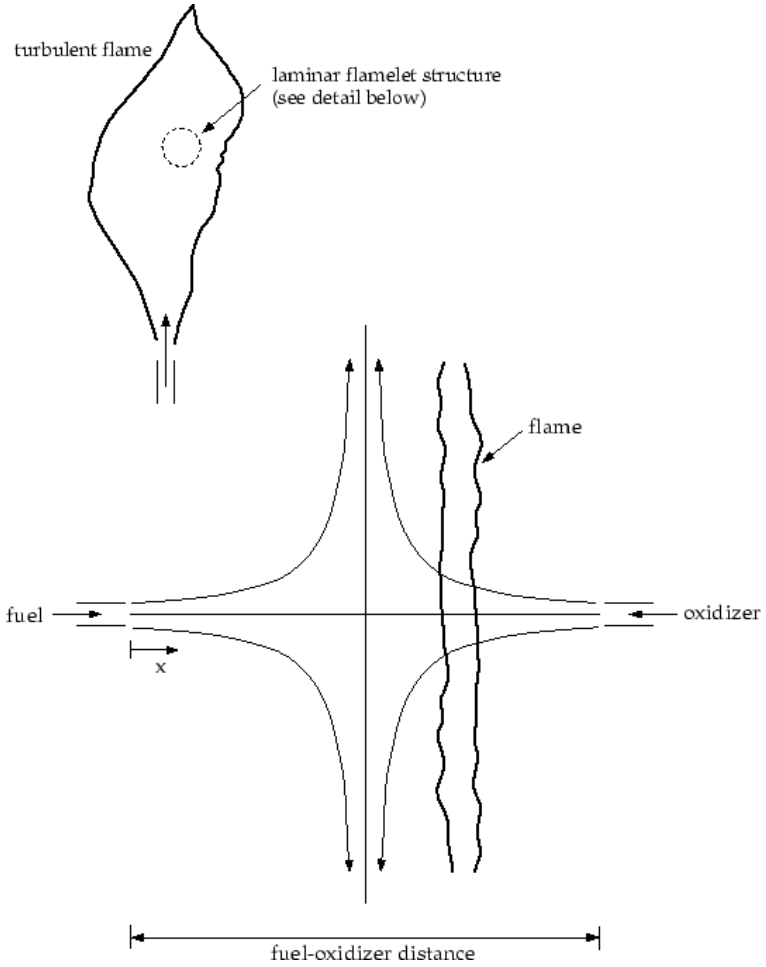

Figure 3.1.1: Laminar opposed flow diffusion flamelet [9].

With the Laminar Flamelet model, the location of the inner surface will define the flame surface. The flamelet model focuses on the location of the flame surface and not on the reactive scalars themselves so that location is dependent on a non reacting scalar. For non pre-mixed combustion this variable is the mixture fraction Z. This mixture fraction is a measure of the amount of fuel in a given mixture. It is defined in such a way that it is 1 at the fuel and 0 at the oxygen inlet.

The mixture fraction Z is non reacting and no chemical source terms are needed to calculate it. This means that it can be calculated using classical turbulent modeling assumptions. The mixture fraction will be calculated with a presumed Probability Density function (PDF) approach, which will be described later.

Once the flamelet equations have been solved then the presumed PDF approach can be used to calculate the mean values of all the reactive scalars and mean reaction rates. Furthermore, the mean values for the species mass fraction and the specific enthalpy will be stored in a tabulated library. This means that these computations will have happened beforehand and during runtime the calculated values can be accessed and used, saving computation time.

3.1.1 Laminar Flamelet Equations for Non Premixed Combustion

The governing equations for the flamelet model as derived by Peters [22] can be found in Eq. 3.1 and Eq. 3.2. Here ρ is the density, Y_k the species mass fraction, T is the temperature, c_p and h_k are the specific isobaric heat capacity and the specific enthalpy of species k. $\dot{\omega}_k$ is the chemical species source term, which is calculated with a chemistry reaction mechanism.

$$\rho\frac{\partial Y_k}{\partial t} - \frac{1}{2}\chi\frac{\partial^2 Y_k}{\partial Z^2} - \dot{\omega}_k = 0 \tag{3.1}$$

$$\rho\frac{\partial T}{\partial t} - \frac{1}{2}\rho\chi\Big(\frac{\partial^2 T}{\partial Z^2} + \frac{1}{c_p}\frac{\partial c_p}{\partial Z}\frac{\partial T}{\partial Z}\Big) + \frac{1}{c_p}\sum_{k=1}^{n} h_k\dot{\omega}_k = 0 \tag{3.2}$$

The scalar dissipation rate, χ, which defines the flame structure, can be seen as an inverse diffusion time scale and has the unit $1/s$ and can be found in Eq. 3.3. The scalar dissipation rate has a dependency on the gradient of the mixture fraction, D is the diffusion coefficient of the scalar dissipation rate.

$$\chi = 2D\Big(\frac{\partial Z}{\partial y}\Big)^2 \tag{3.3}$$

In the domain where the assumptions of the flamelet model are valid, combustion will occur in quasi laminar flow within an eddy of the turbulent flow. So inside of the flamelet, the fluctuations of Y_k, the species mass fraction, and the reaction rate ω_i do not need to be considered. Therefore the mean values for these will be used instead [22]. Furthermore the stoichiometric value for the scalar dissipation rate χ is used instead to simplify the computations, as shown by [22].

After the species mass fraction and temperature are calculated with the flamelet equations the mean values of these scalars are calculated with a presumed Favre PDF. The presumed shape PDF's to integrate the flamelets are:

$$\tilde{Y_k}(x,t) = \int_0^1\int_0^\infty Y_k(Z,t,\chi_{st})P(\chi_{st},x,t)\tilde{P}(\chi_{st},x,t)d\chi_{st}dZ \tag{3.4}$$

$$\tilde{T}(x,t) = \int_0^1\int_0^\infty T(Z,t,\chi_{st})P(\chi_{st},x,t)\tilde{P}(\chi_{st},x,t)d\chi_{st}dZ \tag{3.5}$$

This step is performed with the OpenFOAM utility *canteraToFoam*. These steps that are performed during the presumed PDF are explained more in detail in Section 3.2. The quantities that are necessary for the PDF computation, the mean mixture fraction, its variance and the mean scalar dissipation rate are to be provided by the turbulence model. The approach to compute this depends on the chosen turbulence model. For RANS two additional transport equations for the mean mixture fraction and its variance are required:

$$\frac{\partial\bar{\rho}\tilde{Z}}{\partial t} + \frac{\partial\bar{\rho}\tilde{\mathbf{u}}_i\tilde{Z}}{\partial x_i} = \frac{\partial}{\partial x_i}\Big(\mu_{eff}\frac{\partial\tilde{Z}}{\partial x_i}\Big) \tag{3.6}$$

$$\frac{\partial\bar{\rho}\widetilde{Z''}}{\partial t} + \frac{\partial\bar{\rho}\tilde{\mathbf{u}}_i\widetilde{Z''}}{\partial x_i} = \frac{\partial}{\partial x_i}\Big(\mu_{eff}\frac{\partial\widetilde{Z''}}{\partial x_i}\Big) + 2\mu_{eff}\Big(\frac{\partial\tilde{Z}}{\partial x_i}\Big)^2 - \bar{\rho}\tilde{\chi} \tag{3.7}$$

The effective viscosity μ_{eff} consists of the laminar and the turbulent viscosity and $\widetilde{Z''}$ is the mean variance of the mixture fraction The turbulent viscosity is then computed with the chosen turbulence model. The scalar dissipation rate is expressed as Eq. 3.8. k is the turbulent kinetic energy and ϵ is the corresponding dissipation rate. C_χ is a constant and is set to 2.

$$\tilde{\chi} = C_\chi \frac{\epsilon}{k} \widetilde{Z''} \tag{3.8}$$

In the case that LES is used, the equation for the mean mixture fraction is the same as Eq. 3.6, except that the effective viscosity now consists of a resolved part and a modeled part which is computed by the SGS fluctuations. The variance of the mean mixture fraction is defined as follows:

$$\widetilde{Z''} = C_Z \Delta^2 \left| \frac{\partial \tilde{Z}}{\partial x_i} \right|^2 \tag{3.9}$$

C_Z is a constant with the value of 1. Next to this the mean scalar dissipation rate is formulated in Eq. 3.10. Furthermore Eq's 3.8 and 3.10 are formulated to be used with the actual value for the scalar dissipation and not the stoichiometric value. However, the flamelets in the library are characterized by the stoichiometric value. So again the assumption is made that using the stoichiometric value for this will be valid, as is shown in [9] that this practice is acceptable.

$$\tilde{\chi} = C_\chi \frac{\mu_{eff}}{\bar{\rho}} \left| \frac{\partial \tilde{Z}}{\partial x_i} \right|^2 \tag{3.10}$$

Assumptions made with the Tabulated Laminar Flamelet Model

- Dahmköhler number must be large, this means that reaction times become very fast and most of the chemistry will be active inside of a thin layer in the flame.
- During computations only the stoichiometric value for the mixture fraction is used.
- Combustion occurs in quasi laminar flow inside of a turbulent eddy, so inside of the flamelet only the mean values for the species mass fraction and the reaction rate will be used.

3.2 The Presumed PDF Approach

The presumed PDF is an approach that assumes a suitable two parameter probability density function in advance [22]. This means that the two parameters of the probability density function are related to the known values of the Favre mixture fraction and its variance, $\tilde{Z}$ and $\widetilde{Z''^2}$. Here the joint PDF is first decomposed while assuming statistical independence:

$$P(Z, \chi_{st}) = P(Z) P(\chi_{st}) \tag{3.11}$$

The Beta function PDF is widely used in non-premixed combustion modeling and is also used here:

$$\tilde{P}(Z) = \frac{Z^{\alpha-1}(1-Z)^{\beta-1}}{\Gamma(\alpha)\Gamma(\beta)} \Gamma(\alpha+\beta) \tag{3.12}$$

In this relation Γ is the gamma function. Furthermore the two variables α and β are related to the Favre mean, $\tilde{Z}(x,t)$, and variance $\widetilde{Z''^2}(x,t)$. α and β are formulated as:

$$\alpha = \tilde{Z}\gamma, \quad \beta = (1-\tilde{Z})\gamma \tag{3.13}$$

Where γ is defined as follows.

$$\gamma = \frac{\tilde{Z}-(1-\tilde{Z})}{\widetilde{Z''^2}(x,t)} - 1 \geq 0. \tag{3.14}$$

In Fig. 3.2.1 this Beta function is plotted for a number of combinations of the Favre mean and γ. With this presumed PDF approach the mean of any quantity that is dependent only on the mixture fraction can be computed.

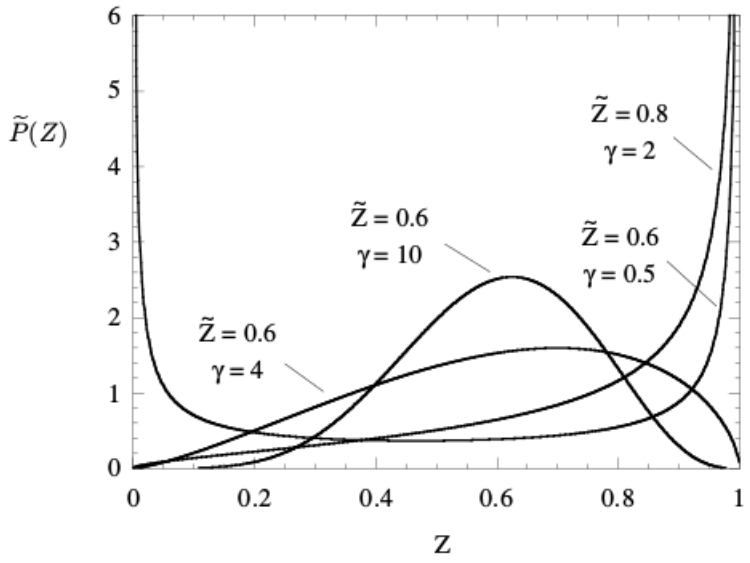

Figure 3.2.1: The Beta function for different values of $\tilde{Z}$ and γ [10].

CHAPTER 4

Methodology

In this section the methodology of the research will be stated. First the CFD software OpenFOAM will be explained. The advantages and disadvantages of the software will be quickly discussed. After this, the file structure and discretization schemes are given. This is followed by a description of the solver *rhoPimpleFoam*, which is a transient solver for laminar or turbulent flow in compressible fluids. The procedure of using the tabulated flamelet in combination with OpenFOAM and the effect of the scalar dissipation rate on the flame temperature is given next. Lastly the geometry of the combustion chamber can be found.

4.1 CFD software OpenFOAM

The software that will be used is the program OpenFOAM, which stands for Open source Field Operation And Manipulation. The reason OpenFOAM will be used for this thesis is because the in-house code of the Bundeswehr Universität already makes use of OpenFOAM. From the outset OpenFOAM is a C++ library that is used to create executables which are also known as applications. The applications are split into two categories, solvers and utilities. The solvers are designed to compute a specific problem in continuum mechanics. The utilities are designed to perform simple pre- and postprocessing tasks.

Below the advantages and disadvantages of using OpenFOAM are stated. It is important to be aware of this while making use of the program so that the software is used to its advantage and care is taken of its lesser points.

Advantages

- Open source software, the source code of the software is available and can be adjusted when desired.
- The software is free to download and operate. Other CFD software can be very expensive.
- OpenFOAM has a wide range of applications and libraries, including combustion modeling.

- Automatic parallelization, OpenFOAM has easy to use parallel processing utilities. With this the computational case can be decomposed and run on multiple clustered processors. Parallel computations allow for effective application of higher computational power.
- Growing community of users in industries.

Disadvantages

- The development community can be fragmented, which can lead to forked projects.
- Program errors are still often found and reported in the user community.
- Limited support available when running into issues.

4.1.1 Discretization

Discretization means that a continuous function is approximated by discrete sub-entities. The discretization of the domain can be split up into spatial and temporal discretization. Spatial discretization means that the solution domain is defined as a number of defined sub-volumes that fill and bound a volume of space. For transient problems such as with LES or IDDES, temporal discretization involves dividing the time domain into a finite number of time steps [4].

OpenFOAM gives a number of options that can be taken as discretization operators. The discretization schemes can be adjusted in *fvSchemes*. The options can be found in the list below.

- Discretization of time schemes. First order time derivatives, $\partial/\partial t$.
- Discretization of gradients, ∇. This is needed for evaluating diffusive terms such as the viscous stress in the momentum equation.
- Discretization of the divergence terms, which are terms of the form $\nabla\cdot$. This excludes Laplacian terms of the form $\nabla\cdot(\Gamma\nabla...)$ and includes advection terms such as $\nabla\cdot(\mathbf{u}k)$. This treatment of advective terms is one of the major challenges in CFD numerics [23].
- Laplacian schemes, $\nabla \cdot (\nu\nabla\mathbf{u})$.
- Surface normal gradient schemes, computes the gradient normal to a cell face.
- Interpolation schemes, this handles the cell to face interpolation of values. It is primarily used in the interpolation of velocity to the face centers.

In the next subsections the spatial and temporal discretization theory that OpenFOAM uses will be further elaborated on.

Spatial Discretization

OpenFOAM uses the Finite Volume (FV) method for spatial discretization. With this discretization method the entire domain is decomposed into non-overlapping control volumes. Every FV is considered as a Control Volume (CV) and for each CV the evolution of the mean values is computed. A typical CV is shown in Fig. 4.1.1, although this is a CV for an unstructured cell the principle is

the same. In this figure, d is the vector which connects the cell centres P and N. Furthermore, A is the face normal area vector which is used for the common face between the two cells. All of the main variables are defined at the cell centres P and N, but it is possible to define some interpolated values at the cell face f.

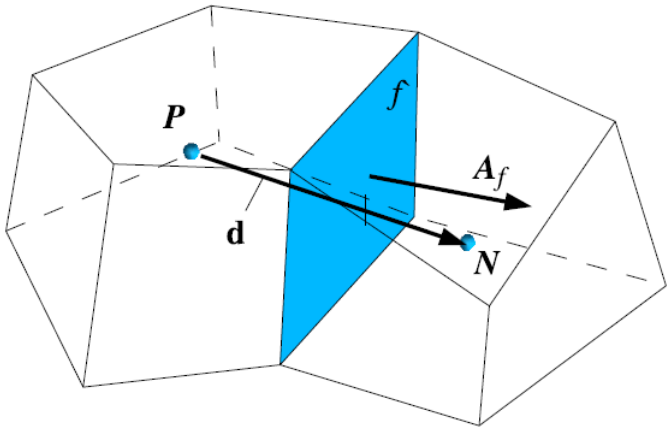

Figure 4.1.1: A control volume used for finite volume discretization [4].

After the domain is divided into CV's, the next step is to integrate the differential form of the governing equations. This is done as in Eq. 4.1, using Gauss' Divergence Theorem these volume integrals of divergences are then transformed into surface integrals with Eq. 4.2. Here ϕ is the conserved quantity and Ψ is the flux.

$$\frac{\partial}{\partial t}\int_{\bar{V}} \phi dV = -\int_{\bar{V}} \nabla \cdot \Psi dV \tag{4.1}$$

$$\int_{\bar{V}} \nabla \cdot \Psi dV = \int_{S_V} n \cdot \Psi dS \tag{4.2}$$

As an example of this approach the momentum conservation is shown in its integral form in Eq. 4.3.

$$\frac{\partial}{\partial t}\int_{\bar{V}} \rho \underline{u} dV + \int_{S_V} \rho \underline{u}\underline{u} \cdot \underline{n} dS = -\int_{S_V} p dS + \int_{S_V} \underline{\underline{\tau}} \cdot \underline{n} dS + \int_{\bar{V}} \rho \underline{F}_V dV \tag{4.3}$$

The time evolution of the cell average is determined by the fluxes. The fluxes are calculated from the known cell values ϕ. There are a number of methods that are available to compute the balance of fluxes. First of all one can use quadrature methods to compute this. Here the surface integral of the fluxes is approximated by the sum of discrete values at several points on the surface of the cell. Next to this, interpolation can be used. With interpolation ϕ at the cell surface is computed from the value of ϕ at the cell center.

OpenFOAM employs interpolation to compute the balance of fluxes. The idea behind face interpolation is further illustrated in Fig. 4.1.2. In this thesis variants of the Gauss linear scheme are used. This means that first Gauss integration is used, followed by linear interpolation of the

fluxes. Pure Gauss linear was found to be too unstable, therefore bounded schemes were used to increase the stability of the simulation. The Gauss VanLeer scheme was used in the combustion chamber simulations.

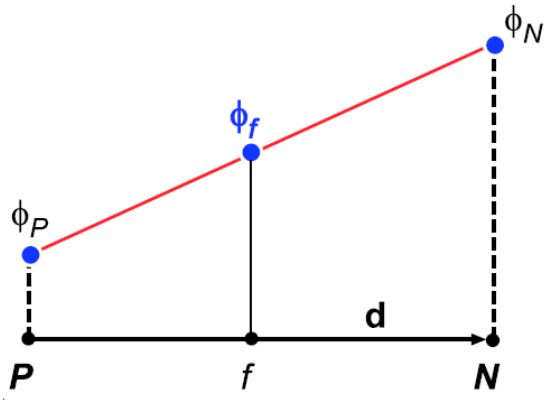

Figure 4.1.2: Face interpolation [4].

Time Discretization

A number of options are available to choose as a discretization scheme with OpenFOAM. In order to achieve high enough accuracy in the simulations, the scheme had to be second order. The OpenFOAM package offers two choices in this field. The second order Backward Differencing scheme and the Crank-Nicolson (CN) scheme. The Backwards Differencing scheme was used at first but it was found to be very difficult to use in simulations without encountering a crash, especially when turbulence was involved. The disadvantage to the CN scheme is that it is computationally more expensive to use than the Backwards Differencing scheme.

The advantage that the CN scheme offers in OpenFOAM is that even though it is a transient second order scheme, it can be bounded and stabilized in order to be practical for engineering problems [23]. This is done through an off-centering coefficient between 0 and 1. 0 corresponds to the first order Euler scheme and 1 to full CN.

The CN scheme is second order and implicit in time. It was developed by John Crank and Phyllis Nicolson in 1947 [24]. The CN method is often applied to diffusion problems. The expression for the CN scheme will be given below. Firstly, the temporal derivative and integral are stated in Eq's 4.4 and 4.5.

$$\left(\frac{\partial \phi}{\partial t}\right)_P = \frac{\phi_P^n - \phi_P^{n-1}}{\Delta t} \tag{4.4}$$

$$\int_t^{\Delta t} \phi(t)dt = \frac{1}{2}(\phi^{n-1} + \phi^n)\Delta t \tag{4.5}$$

Here, $\phi^n = \phi(t + \Delta T$ and $\phi^{n-1}\phi(t)$ indicate the value of the variable of the new and previous time respectively. The general formulation for the Crank-Nicolson time scheme is in Eq. 4.6. f

represents the solution of the field as a function of the general scalar ϕ. The full derivation that is implemented in OpenFOAM can be found in [4].

$$\frac{\phi^n - \phi^{n-1}}{\Delta t} = \frac{1}{2} \cdot (f(\phi^n) + f(\phi^{n-1})) \tag{4.6}$$

During the CN computations in OpenFOAM an extra vector is added to compute components of the mesh that are not orthogonal. The CN scheme requires the face and cell-centered values of ϕ and $\Delta\phi$ together with the diffusive and convective fluxes along for the current and new time levels. The flux and the non-orthogonal component of the diffusion term are being calculated at the new time, it is necessary to calculate inner-calculation at each time step. This results usually in a higher computational cost than for the Backwards Differencing scheme.

Next to this the Courant-Friedrichs-Lewy (CFL) condition plays a role in the stability of the simulation. It is defined as the product of the velocity and the timestep, divided by the width of a cell. It basically indicates if the flow has enough time to traverse the length of a cell in a single timestep. The formulation can be found in Eq. 4.7. To maintain stability during the simulation it should be set lower than 1, in the current simulations it is set to 0.2.

$$CFL = \frac{|u|\Delta t}{\Delta x} \tag{4.7}$$

4.1.2 OpenFOAM Solver

The solver that will be used during the computations is *rhoPimpleFoam*. It is a transient solver for laminar or turbulent flow in compressible fluids and it uses the flexible PIMPLE (PISO-SIMPLE) algorithm, which is a combination of the PISO and SIMPLE algorithms [25]. PISO stands for Pressure Implicit Splitting of Operators, this is an operation which is responsible for solving the pressure-velocity coupling. PISO includes a momentum predictor and a number of corrector steps and it is designed to conserve mass during the momentum and corrector steps.

SIMPLE stands for Semi-Implicit Method for Pressure Linked Equations and is an algorithm designed to solve the Navier Stokes equations. It is designed for use with steady state problems and does not fully resolve the pressure velocity coupling. The difference between PISO and SIMPLE is that PISO runs the pressure momentum loop more than once, for a more accurate solution. However, in PISO mode the solver is limited to a timestep that fulfills the constraint set by the CFL number. Thus by combining the advantages of both solvers the PIMPLE procedure is created.

The PIMPLE algorithm works as follows. First an approximation is made of the velocity field by solving the momentum equations. Then the mass fluxes at the cell faces is computed. The pressure equation is solved and under relaxation is applied. Next, the mass fluxes at the cell faces is applied. The velocities are corrected based on the new pressure field.

Next the pressure distribution from the previous iteration or an initial guess is used to calculate the pressure gradient. Following this, the pressure equation is solved to obtain the new pressure distribution. As a final step, the velocities are corrected and a new set of conservative fluxes are calculated. This loop is repeated until convergence is achieved in the PISO loop, after this the SIMPLE loop, where under relaxation is applied is repeated until convergence is obtained. In the

following figure the PIMPLE flowchart is shown. It can be seen that the SIMPLE algorithm is used to first solve the velocity and temperature field. Next the PISO algorithm is run to ensure the pressure-velocity coupling.

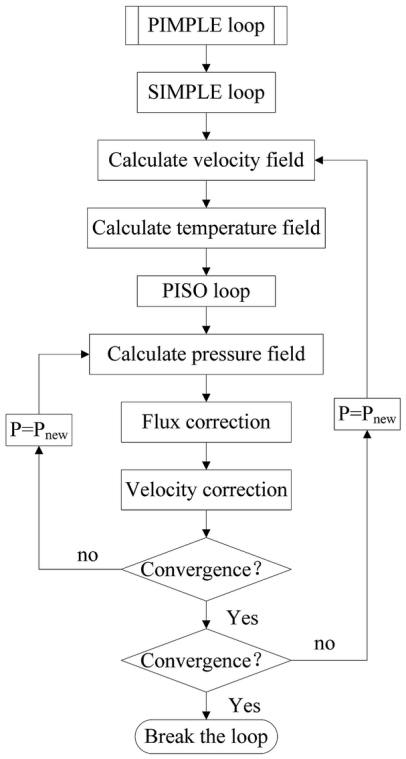

Figure 4.1.3: Flowchart of the PIMPLE algorithm [11].

4.1.3 Pressure Velocity Coupling

Due to the fact that pressure and the velocity are dependent on each other, a pressure equation is used to couple them together. This equation is based on the momentum equation. The pressure equation is formulated as:

$$a_p \bar{u}_p = H(\bar{\mathbf{u}}) - \nabla \bar{p} \tag{4.8}$$

The full derivation of this equation will not be considered in this thesis, but the details can be found in [4]. There it is given that the final form of the Navier Stokes equations can be stated as the following. The PIMPLE algorithm solves these two equations during its loop.

$$a_p \bar{\mathbf{u}}_p = H - \sum_f A \cdot \bar{p}_f \tag{4.9}$$

$$\sum_f A \cdot \left(\frac{1}{a_p}\right)_f (\nabla \bar{p})_f = \sum_f A \cdot \left(\frac{H}{a_p}\right)_f \tag{4.10}$$

4.1.4 Filtered Noise Inflow Generator

The inlet boundary condition that is used for the thesis is the *filteredNoiseInflowGeneratorMassFlowRate*. It is an inlet boundary condition that generates turbulence based on a prescribed mass flow rate. This method is used because it performs well in generating a turbulent velocity inflow field. Some other methods fail to prescribe enough energy in the inflow, as a consequence the results become similar to laminar flow. The filtered noise BC code was written by [12] as a MATLAB file.

The program requires the input of the mean velocity of the inlet, the density, the type of inlet and the location grid of the inlet. The type of inlet is either *annulus* or *pipe*, for the fuel or oxygen inlet respectively. The coordinate grid for the inlet is obtained with the OpenFOAM functionality *printPatchFaces*. The main procedure of the code can be summarized as follows.

- The generation of normally distributed random numbers with unity variance for the velocity.
- A filtering operation is imposed with a two point autocorrelation. Filtering is done to add temporal and spatial correlations to the velocity field. This is performed because a purely random velocity field dissipates too quickly.
- Scaling of the velocity is done to obtain the desired variance and covariance.
- Superposition with a mean velocity.

In Fig. 4.1.4 the various outputs of the previously described steps are visualized. The inflow generation procedure happens at every timestep. The procedure was designed to be computationally efficient because for most LES simulations the timesteps are small and thus result in a high number of timesteps for most cases. During the simulation the boundary condition linearly scales the magnitude of the velocity so that the prescribed mass flow rate into the chamber is maintained. The full derivation of the method can be found in [12].

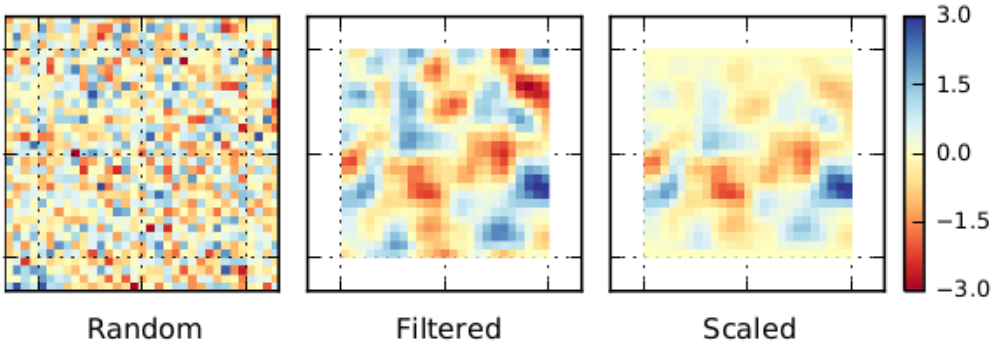

Figure 4.1.4: The outputs of the described steps to generate a fluctuating field with a prescribed autocorrelation and variance is visualized [12].

In Fig. 4.1.5 the procedure where the velocity field is mapped to the domain is better illustrated. As can be seen, two types of grids are used. A virtual grid and a patch grid. The virtual grid has a uniform grid spacing and the patch grid corresponds to the inlet patch of the domain. Then two

virtual grids are used, one for the random field and one for the filtered field. The next step is to interpolate the filtered field of the virtual grid unto the patch grid.

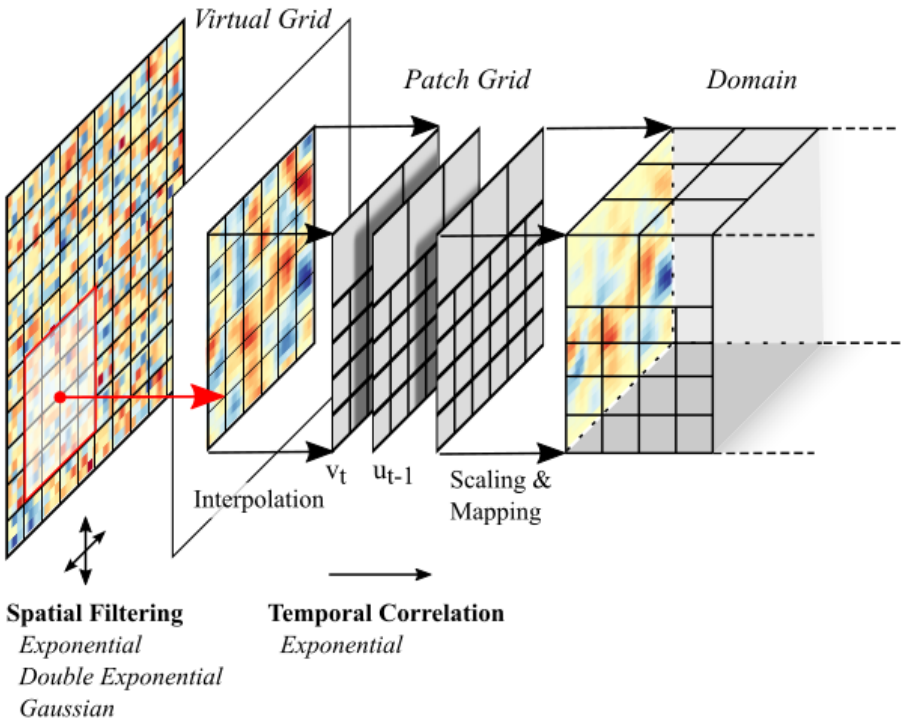

Figure 4.1.5: The steps of mapping the grid to the domain [12].

4.2 Tabulated Combustion

In this section the procedure of the flamelet combustion model and its implementation into the turbulence model will be briefly discussed. The steps that are taken can be seen below in Fig. 4.2.1. First as a pre-processing step, the flamelet equations are solved beforehand using mixing fraction Z and the scalar dissipation rate χ. Only stoichiometric values for the scalar dissipation are used to simplify the calculations. The flamelets are solved with the open source software Cantera. These equations then yield the species mass fraction Y_k and the temperature. Afterwards the flamelets are integrated using a Favre PDF, this yields the mean values for the species mass fraction and the temperature. This is done with an OpenFOAM utility called canteraToFoam.

Next to this, many thermodynamic computations are based on the specific enthalpy, h_s. The same utility, canteraToFoam, is therefore also used to compute the mean value of the specific enthalpy using the temperature. After the PDF integration and computation of h_s the mean species mass fraction and enthalpy are stored in the flamelet library as a function of the mean values of the mixture fraction and it variance $\tilde{Z}$ and $\widetilde{Z''^2}$ and the mean stoichiometric scalar dissipation rate χ_{st}. Following this, during the CFD simulation these values are provided and then the species mass fraction can be found through interpolation [10].

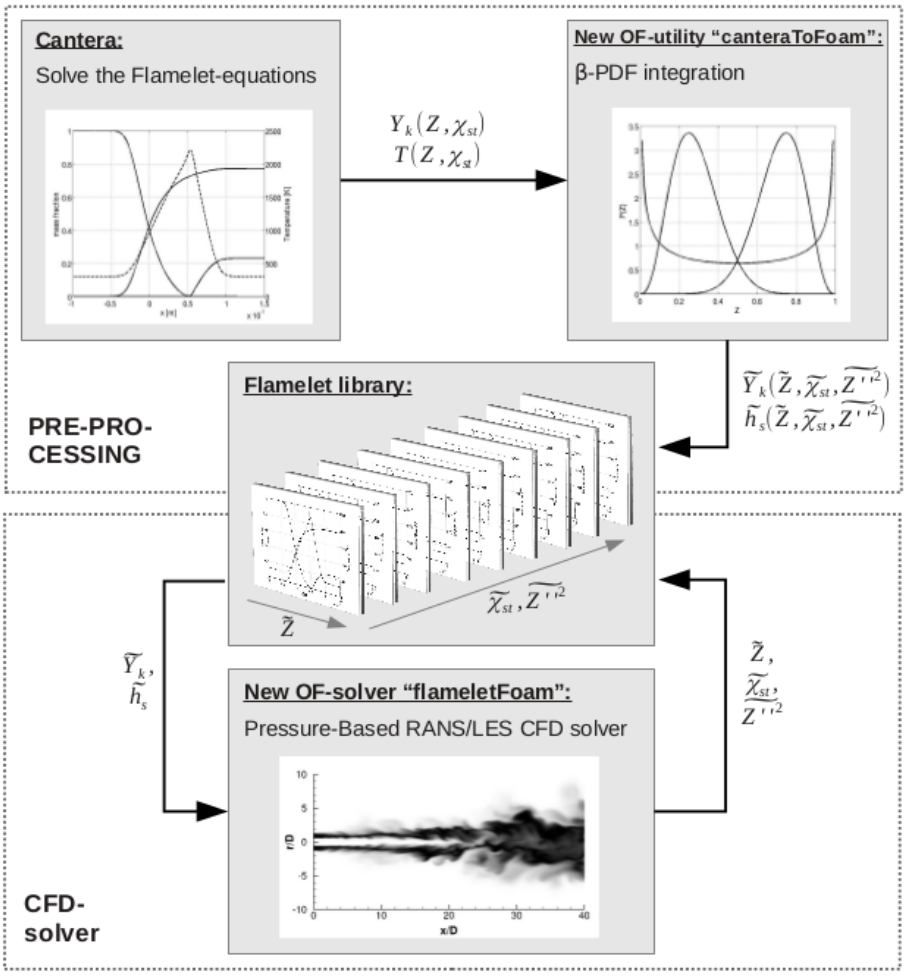

Figure 4.2.1: The schematic of the flamelet approach with a CFD solver [10].

4.2.1 The Implementation of the Scalar Dissipation Rate

The method of calculation for the scalar dissipation rate, the fuel fraction and its variance are described in Sec. 3.1.1. Unfortunately the current definition for the scalar dissipation for RANS did not function. This is due to the fact that the SA model does not work with the turbulent kinetic energy, k, and the turbulent dissipation rate, e. Therefore another solution had to be devised in order for the model to work while using RANS.

It was decided to use the LES definition for RANS instead. The justification for this was that the changes that this meant for the scalar dissipation are expected to to very small. This is because the flame temperatures vary only very little for for the values of the scalar dissipation rate that are present in the simulations of the combustor. The effect of the scalar dissipation rate on the flame temperature will be described in the next section. The further implications for this are the following:

- When the RANS formulation for the scalar dissipation rate is viewed as a Prandtl Eddy Viscosity Model, then the component $\frac{k}{\epsilon}$ would be the characteristic length. For the SA model the characteristic length would be the distance to the wall. Instead of this characteristic length now Δ is used for the LES formulation in RANS mode.
- The LES formulation was based on the assumption that information on the instantaneous gradients of the flow are included. If RANS is supplies the variables then of course part of this information will be missing.
- The effective viscosity that is used in the LES formulation now consists only of a modeled component in RANS mode.

Effect of the Scalar Dissipation Rate on the Flame

In this section the effect of the scalar dissipation rate on the flame will be investigated. Next to this, it will be shown that the flame temperature does not vary much for the range of scalar dissipation rates that are used. This will be done by looking at a number of figures where the flame temperature is plotted versus the fuel fraction for a number of scalar dissipation rates. This is computed using the same flamelet equations as in this thesis. It can be seen that for the lower fuel fractions the maximum temperature decreases for a higher scalar dissipation rate. Increasing the scalar dissipation rate from 1 to 200,000 decreases the maximum temperature from around 3500 to 3000 degrees. On the other hand, for higher fuel fractions a higher scalar dissipation increases the temperature.

The flame extinction point can be observed for high scalar dissipation rates, it can be seen for a scalar dissipation rate of 200,000 in the figure below. Here the temperature is lower for all fuel fraction regimes. Too high scalar dissipation rates provide too much strain on the flame and will force it to extinction. The value of the scalar dissipation rate in the simulations has a maximum of around 3000. It can be seen that for these values the temperatures of the flame vary minimally.

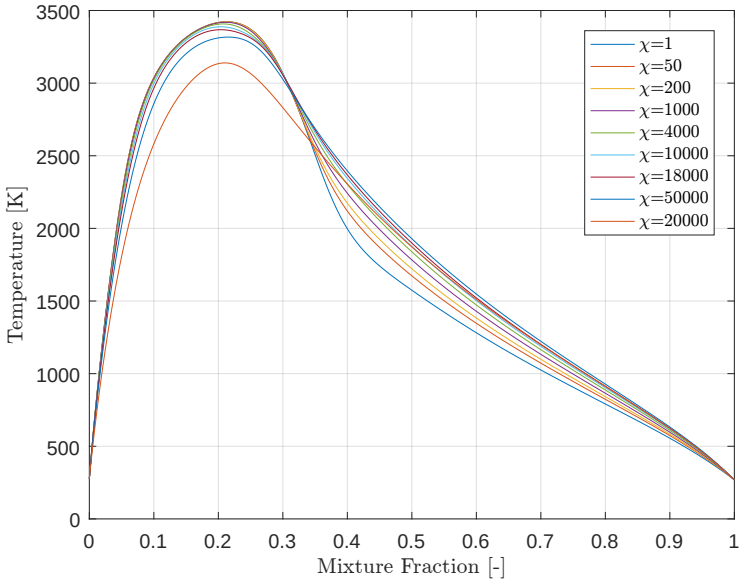

Figure 4.2.2: The flame temperature plotted against mixture for a number of scalar dissipation rates.

In Fig. 4.2.3 the maximum flame temperature is plotted against the scalar dissipation rate. Next to this, the values of the maximum scalar dissipation rate in the RANS area and the entire simulation are indicated. It can be seen that up until a scalar dissipation rate of 1000, the maximum flame temperature is barely affected. In the locations where RANS is active, the scalar dissipation rate has a maximum value of 100. The maximum overall scalar dissipation rate in the entire simulation is 3300. From this figure it can be deduced that the effect of varying the scalar dissipation rate in the boundary layer is very small.

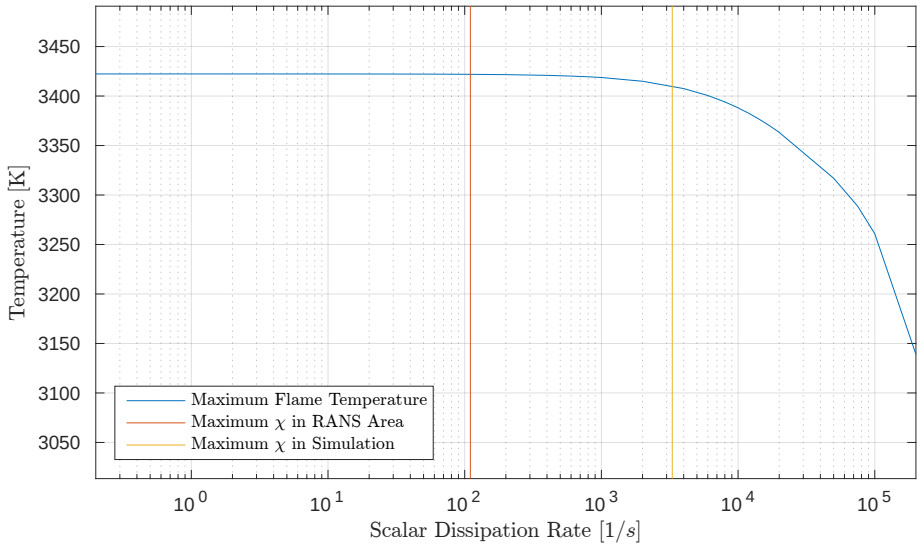

Figure 4.2.3: The maximum flame temperature plotted against the scalar dissipation rate

The air to fuel equivalence ratio, λ, is plotted in Fig. 4.2.4 This is the ratio of the actual air to fuel compared to the stoichiometric value. A value of $\lambda = 1$ indicates a mixture at stoichiometrie, $\lambda < 1$ indicates a rich mixture and $\lambda > 1$ is a lean mixture. It can be seen that the most stoichiometric mixture is obtained for a fuel fraction of 0.3 to 0.4, comparing a scalar dissipation rate of 1 to 200,000 the maximum air to fuel equivalence ratio is decreased from around 0.42 to about 0.34. For higher and lower fuel fractions the scalar dissipation rate has a smaller effect. It can be concluded from the figure that the scalar dissipation rate has a considerable effect on the stoichiometric composition on the mixture.

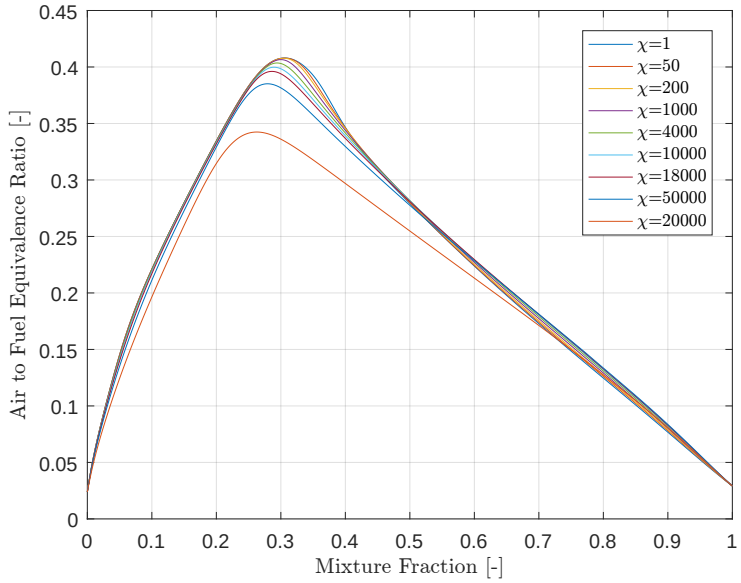

Figure 4.2.4: The air to fuel equivalence ratio plotted against the flame temperature for a number of scalar dissipation rates.

Using these graphs it is then justified to use the LES formulation to calculate the scalar dissipation rate in RANS area's. This is done based on the following points.

- For low values of the scalar dissipation rate the flame temperature does not vary strongly, this can be seen in Fig. 4.2.2. Furthermore, the scalar dissipation rate is very low in the RANS regions and so has a minimal effect on the flame temperature, as seen in Fig. 4.2.3.
- The IDDES formulation for Δ is used instead of the standard LES cube root formulation. Since IDDES is devised to have RANS in the boundary layer while using this Δ, it will be assumed to be appropriate to use it as well for the scalar dissipation rate. Furthermore, the IDDES formulation of Δ is dependent on the wall distance, just as the definition for the length scale in the Spalart-Allmaras model. This means that the length scale computed according to the IDDES definition will show correspondence with how it is calculated with the SA model.
- The scalar dissipation rate is mostly relevant in the mixing region in the free shear layer, where LES is active.

4.3 The Combustion Chamber

In this section the BKD-9 combustion chamber will be described. The chamber has been constructed by the Technical University of Munich. The geometry of the combustion chamber can be seen in Fig. 4.3.1. The material that was used for the chamber segments is oxygen free copper. The combustion chamber has a square inner cross section of 12 by 12 mm. Furthermore it consists of two chamber segments of 174 mm and 145 mm and it has a nozzle segment of 20 mm. The nozzle has an unusual geometry because of its rectangular cross section, with dimensions of 4.8mm by 12mm. It has a contraction ratio of 2.5 and a Mach number of 0.24 in the chamber.

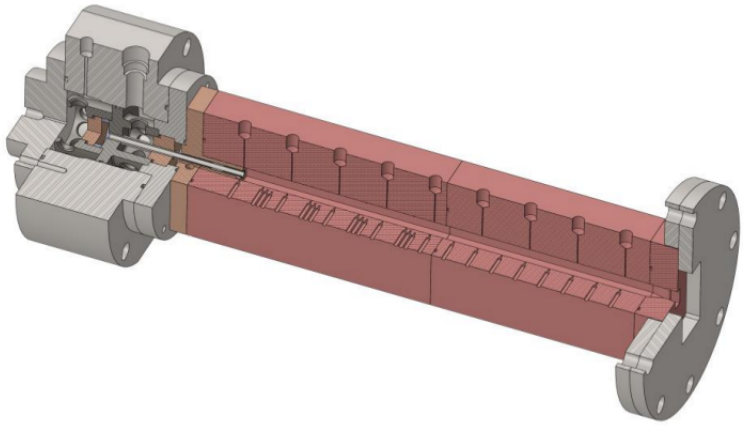

Figure 4.3.1: The geometry of the BKD9 combustion chamber [13].

The full cross section of the chamber is in Fig. 4.3.2. Ignition in the chamber is achieved by using a torch igniter using GCH4/GOX, this is mounted at the side wall of the combustion chamber perpendicular to the flow direction. Thermocouples and pressure transducers are placed in chamber manifolds along the combustion chamber for the measurements. The operating point that was chosen for the test with the combustion chamber was 20 bar and the mixture ratio was 2.6. The pressure and wall heat flux measurements are reported in Celano et al [13]. The combustion chamber has no cooling system present and therefore its temperature rises during the experimental burning time, which is 5 seconds.

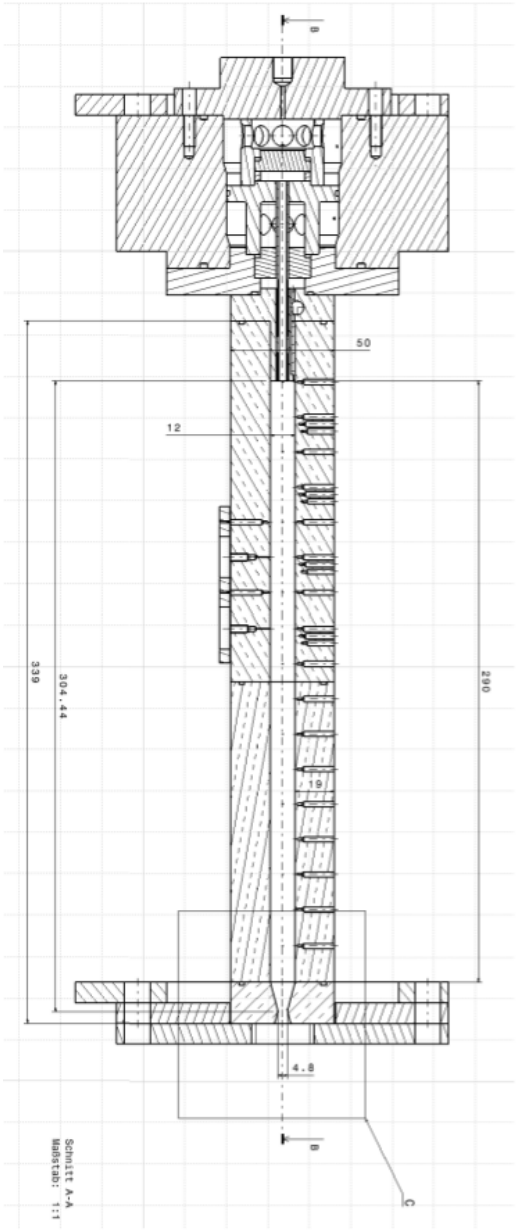

Figure 4.3.2: Cross section of the combustion chamber [13].

Chamber length	[mm]	303
Chamber internal width	[mm]	12
Chamber internal height	[mm]	12
Chamber external width	[mm]	85
Chamber external height	[mm]	50
Throat width	[mm]	12
Throat height	[mm]	4.8
Contraction ratio	[-]	2.5
Characteristic length	[mm]	749

Table 4.1: Chamber dimensions

The measured wall temperature is averaged over a period of 5 seconds, which is centered at $\frac{2}{3}$ of the burning time. Furthermore, during the tests the temperature along the temperature along the center of the channel was recorded. Using this experimental data, Celana et al [13] reconstructed the wall heat flux through means of an inverse heat conduction problem. The exact method that was used to compute the wall heat flux will be explained in Sec. 4.3.1.

The injector is a single shear coaxial injector element, which is integrated into the combustor.

The oxygen is injected in the core and high speed gaseous methane is injected around it. In order to ensure homogeneous injection conditions, considering the temperature and pressure, two porous plates were installed in the oxidizer and fuel manifolds. This can be seen in Fig. 4.3.3.

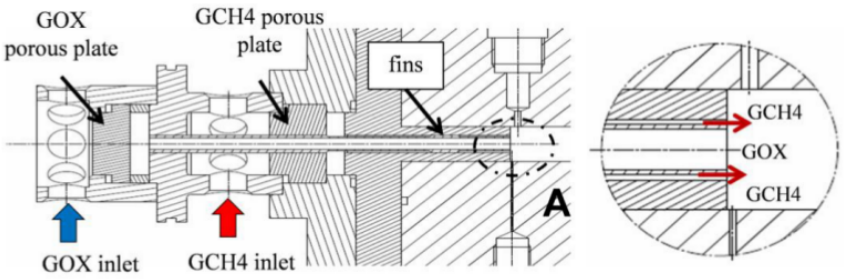

Figure 4.3.3: The shear coaxial injector [13].

In Tab. 4.2 the operating conditions for the test are given [26]. The operating pressure is 19 bar, the Oxidizer to Fuel Ratio (OFR) is 2.62, the oxidizer, fuel and total mass flow rate are 0.045, 0.017 and 0.062 respectively.

Parameter	**Unit**	**Value**
Operating Pressure	[bar]	19
OFR	[-]	2.62
$\dot{m}_{ox}$	$\frac{kg}{s}$	0.045
$\dot{m}_f$	$\frac{kg}{s}$	0.017
$\dot{m}_{tot}$	$\frac{kg}{s}$	0.062

Table 4.2: The operating conditions for the experimental tests.

4.3.1 Calculating the Heat Flux

The wall heat flux distribution along the hot wall is one of the main characteristics of an injector element. Furthermore, the flow conditions and dynamics are determined by the mixing mechanisms in the near injector field. The axial and radial temperature distributions were used to compute the wall heat flux. Steady state condition for the temperature was not achieved during the live firing tests. Measuring the temperatures proved to be very challenging due to a high sensitivity to the response time and the placement of the thermocouples [13].

A 2D unsteady heat conduction equation was solved to compute the wall heat flux and take transient effects of the temperature into account. In order to take the cumulative effects of the copper material and square corners into account, the transverse cross section of the combustion is used as the computation domain. The cross-sectional domain can be subdivided into two symmetry planes. This was then used as a control volume for the computations of the entire domain. This control volume can be seen in Fig. 4.3.4.

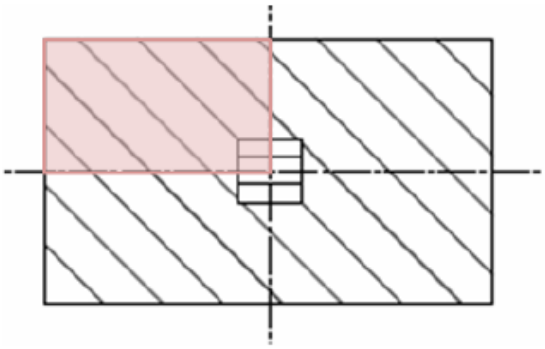

Figure 4.3.4: The control volumes for the Wall Heat Flux [13].

Heat flux boundary conditions are then imposed on the outer and inner walls. Furthermore, the outer wall is assumed to only to be subjected to natural convection with a constant heat convection coefficient. The 2D discretized heat equations that are solved are:

$$\frac{\lambda}{(\delta x)^2}(T_{i+1,j,t} - 2T_{i,j,t} + T_{i-1,j,t}) + \frac{\lambda}{(\delta y)^2}(T_{i+1,j,t} - 2T_{i,j,t} + T_{i-1,j,t}) = \frac{\rho c}{(\delta t)^2}(T_{i,j,t+\delta t} - T_{i,j,t}) \quad (4.11)$$

These equations are solved simultaneously, while marching forward in time and applying the measured temperature data. The density, conductivity and heat capacity of the copper is assumed to be constant. In order to correctly compare the experimental data with the computed data, the numerical data has been circumferentially averaged as well. This was done using the program *Tecplot*.

Sources of Error in Computing the Heat Flux

The experimental values have an error range which are unknown, but the types of errors that can be made are stated here. First of all, there are the limitations of the testing and measurement equipment etc. Then there is the in-stationary heating of the hardware. Due to the heat generated during the live fire tests, the sensors could become affected and measure incorrect data. Next to this, the assumption that the wall is only subjected to natural convection with a constant heat convection coefficient also induces errors. Lastly, the wall heat flux is recalculated from the temperature. So discretization or computational errors could have been made.

CHAPTER 5

Verification and Validation

In this section the verification procedure of the thesis is discussed. First the backwards facing step and the heat transfer testcases are discussed. For each testcase a general description is given, followed by a description of the mesh and boundary conditions, a grid study and the overall results.

5.1 Backwards Facing Step

In order to validate and become familiar with OpenFOAM a backwards facing step testcase was performed using RANS and IDDES. The backwards facing step is an interesting testcase since flow separation and reattachment are present here. The flow enters the domain and then flows over the backwards facing step. Consequently the flow separates and reattaches further downstream. Right after the step there is a recirculation zone. Furthermore, after the flow reattaches the boundary layer redevelops and grows.

NASA has testdata available for this testcase and so their data was used for this. At a number of locations before and after the step experimental data for the velocity profile is available. Next to this, testdata of the friction and pressure coefficient on the lower wall behind the step is given. The location of reattachment can be verified, since the value of the friction coefficient is zero at this point. NASA also has results available of their own CFD simulations next to the experimental data, serving as an extra point for verification. The domain is visualized in Fig. 5.2.1. The domain dimensions and flow conditions such as Mach, Reynolds number, the temperature, the pressure at the outlet and the boundary conditions were given by NASA. These specifications can also be found in the figure below.

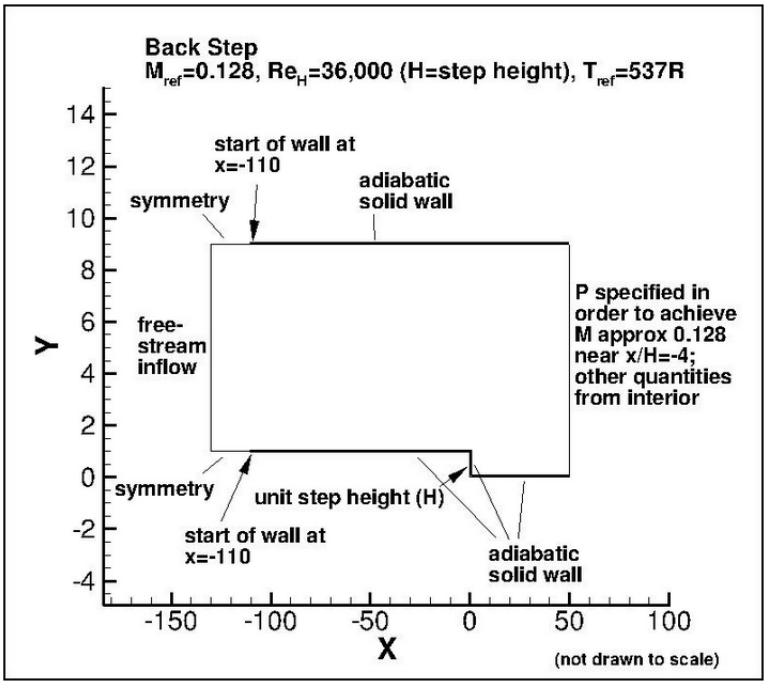

Figure 5.1.1: The domain of the backwards facing step [14].

During the simulations of the BFS 3 different turbulence models were tested: the SA model, DDES and IDDES. The SA model was chosen since it was the underlying RANS model for the hybrid models. Both DDES and IDDES were used in order to investigate the effects of the implementation of IDDES, especially the different definition of the subgrid length scale.

5.1.1 Mesh Design and Boundary Conditions

In this section the specifications of the mesh and the simulations will be given, such as the number of cells, minimum angle, y+ and boundary conditions. The mesh design for the final IDDES run is in the figure below. The most mesh refinement can be found near the walls and the step, this is done to obtain the required y+ and capture the necessary flow properties. The mesh is relatively coarse at the inlet and at the outlet in the centre of the channel to save some computational costs as this was found to have a minimal effect on the results.

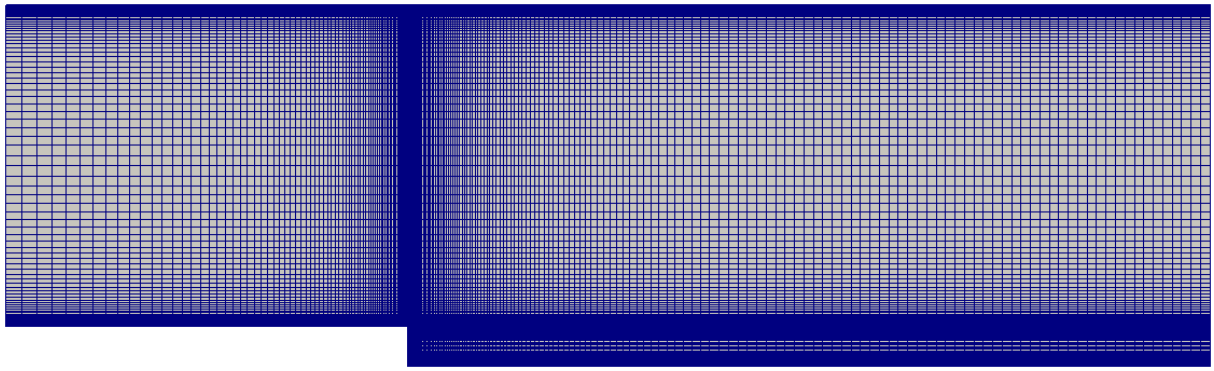

Figure 5.1.2: The mesh for the final IDDES run for the BFS.

While performing the simulations it was found that the results were very sensitive to the value of y+. Especially the friction coefficient was found to vary wildly with a small adjustment of y+, a change of less than 10% could lead to the results of the friction coefficient being completely off. Furthermore, initially many crashes were experienced with DDES and IDDES. The pressure coefficient was much less sensitive to the variations in cell height at the wall. Furthermore, it was found that grid refinement was non monotonic, as was also stated in [5].

While improving on mesh design the simulation crashed a number of times initially. It was found that the cause of the crashes was that there was too much grid refinement right after the step at the height of the wall just before the step. Due to the structure of how the blocks are constructed with OpenFOAM, if the mesh is refined at the wall before the step, then this refinement has to continue downstream. This means that consequently high grid refinement will be present in the shear layer right after the step and further downstream. The refinement at this location was found to have detrimental effects on the stability of the simulation, as soon as the cell dimensions were made larger in this location the simulation was stable again.

Furthermore, it was found that the wall parallel spacing away the step had only very little effect on the final results. This became more so as the distance to the step became larger. As stated before, the main influential factors were the value of y+ and the cell growth factor. A maximum growth factor of 1.1 was maintained in the near wall region. In the area of the centre of the channel, it was found that this value was significantly less critical. In the following table the specifications for each simulation for the BFS can be found.

Parameters	**IDDES**	**DDES**	**SA**
Number of Cells [$\cdot 10^5$]	8.15	8.15	0.37
Maximum Angle [deg]	0	0	0
Maximum Aspect Ratio [-]	66	66	399
y+ [-]	1.5	1.5	1

Table 5.1: Mesh Specifications

In the next table the boundary conditions for the SA simulations are stated. The velocity was given for the inlet, the outlet was defined with the standard inletOutlet boundary condition and for

the walls the noSlip condition was set. Concerning the pressure, for the outlet the waveTransmissive non-reflective boundary condition was used. The eddy viscosity was set to Calculated: 0 at the inlet, outlet and walls. nuTilda was set to $5.55 \cdot 10^{-5}$, using the rule of thumb that it should be three times as large as the kinematic viscosity of the flow. Furthermore it is zeroGradient at the walls and a very low value at the outlet.

Properties	**Inlet**	**Outlet**	**Wall**	**Sides**
Velocity	uniformFixedValue: 44.3	inletOutlet	noSlip	empty
Pressure	zeroGradient	waveTransmissive	zeroGradient	empty
Temperature	fixedValue: 298	zeroGradient	fixedValue: 298	empty
nut	calculated: 0	calculated: 0	calculated: 0	empty
nuTilda	fixedValue: 5.55e-5	zeroGradient	fixedValue: 1e-10	empty

Table 5.2: Boundary conditions for SA for the BFS testcase

In the following table the boundary conditions for the hybrid methods can be found. For the velocity inlet a turbulent velocity profile was imposed, for the outlet the pressureInletOutletVelocity was used. For the pressure the waveTransmissive condition was used again for the outlet. The eddy viscosity was set to zeroGradient for all boundaries except for front and back faces. nuTilda was again put to $5.55 \cdot 10^{-5}$ at the inlet. The front and back boundary conditions were set to cyclic AMI, this stands for Arbitrary Mesh Interface. This allows for a coupling condition between a pair of patches that share the same outer bounds.

Properties	**Inlet**	**Outlet**	**Wall**	**Sides**
Velocity	fixedValue: nonuniform List	pressureInletOutletVelocity	noSlip	cyclicAMI
Pressure	zeroGradient	waveTransmissive	zeroGradient	cyclicAMI
Temperature	fixedValue: 298	inletOutlet	fixedValue: 298	cyclicAMI
nut	zeroGradient	zeroGradient	zeroGradient	cyclicAMI
nuTilda	fixedValue: 5.55e-5	zeroGradient	fixedValue: 1e-10	cyclic AMI

Table 5.3: Boundary conditions for the hybrid methods for the BFS testcase.

5.1.2 Results

In the section the results are given which were obtained after running the BFS simulations. As stated before, experimental results were given for the friction and pressure coefficient and the velocity profiles at the x-locations -4, 1, 4, 6 and 10. The x-location is defined as being zero at the location of the step. In addition to this also the y+ is plotted for the lower wall so it can be seen if enough of the flow dynamics in the near wall region are sufficiently being captured.

The instantaneous velocity field for the backwards facing step is in Fig. 5.1.3. This simulation was performed with IDDES. The flow separation, recirculation zone and a number of vortices are observable in the results. Downstream of the step the flow attaches again to the bottom wall. Lastly, the growing boundary layer on the upper wall can also be seen.

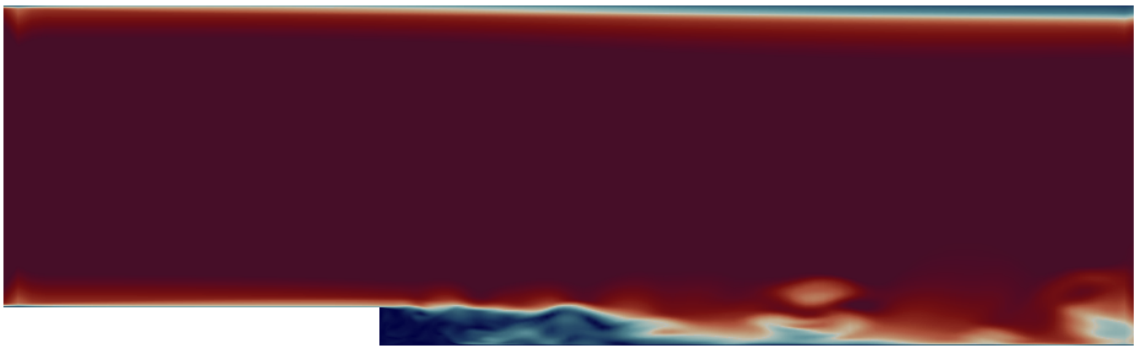

Figure 5.1.3: Instantaneous velocity over the backwards facing step

Errors could arise in the boundary layer of the flow when using the hybrid turbulence models. This manifests itself by premature switching to LES content inside of the boundary layer. The hybrid method is formulated in such a way that it will switch to LES mode if the distance to the wall is larger than the largest cell dimension. So grid refinement near the wall region might result in an unwanted switch. During the simulations for the BFS this phenomenon was encountered as can be seen in the figure below. Here the RANS and LES content is visualized in the flow domain, blue area's indicate a RANS region and red a LES region. There is LES content in the boundary layer, especially on the upper wall. Additionally a region of RANS content can be observed right above the step, where LES content should be. This will locally decrease the amount of resolved turbulence in the flow.

Figure 5.1.4: Erroneous switching between RANS and LES content in the domain.

In the next figure the results can be seen of reducing this adverse phenomenon. This was mainly done by simply increasing the cell sizes in the region of the boundary layer. The eddy viscosity and the modeled Reynolds stress in this region are then reduced without any sizeable resolved stresses

to restore this balance, as stated in Sec 2.4.2. This will lead to a reduction in skin friction and flow separation in extreme cases. In the following figure the instantaneous eddy viscosity is visualized. It can clearly be seen that the eddy viscosity is lowered in the simulation where there is LES content present in the boundary layer on both the upper and the lower wall.

Figure 5.1.5: The mean eddy viscosity with LES content in the boundary layer.

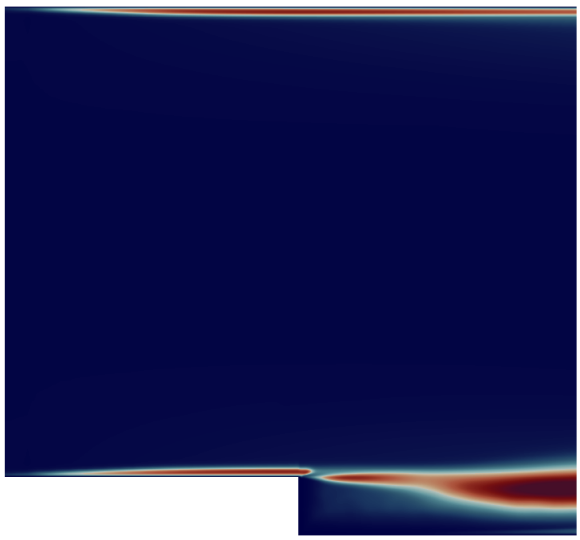

Figure 5.1.6: The mean eddy viscosity without LES content in the boundary layer.

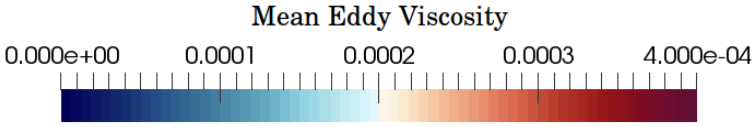

In Figs. 5.1.7 and 5.1.8 the friction and pressure coefficients can be found. The IDDES model is most accurate in predicting the friction and pressure coefficient. This difference is caused by the improved length scale which is used with the IDDES model. The SA model overshoots in predicting the pressure and friction coefficient, this is due to the fact that the one equation RANS model is not capable in correctly predicting the complex flow phenomena which occur in the BFS. The velocity profiles at location x=-4 and 1 are in Figs. 5.1.9 and 5.1.10. IDDES and DDES are both equally more accurate in predicting the profile at x=1 than the SA model.

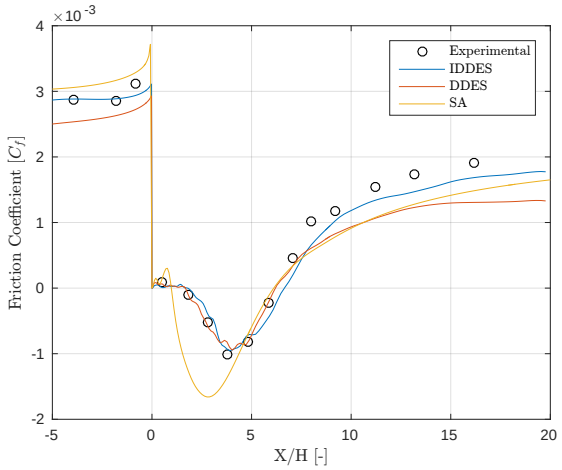

Figure 5.1.7: The friction coefficient along the lower wall.

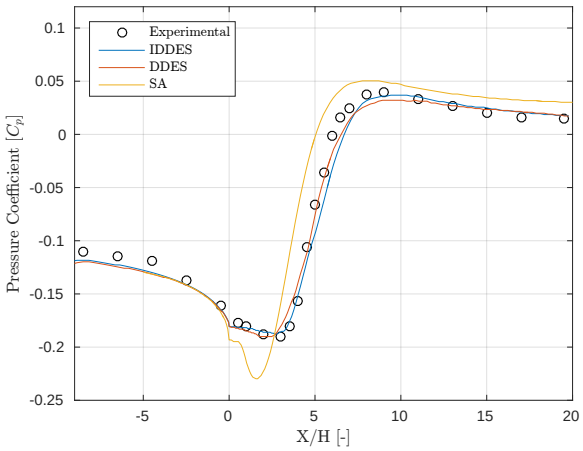

Figure 5.1.8: The pressure coefficient along the lower wall.

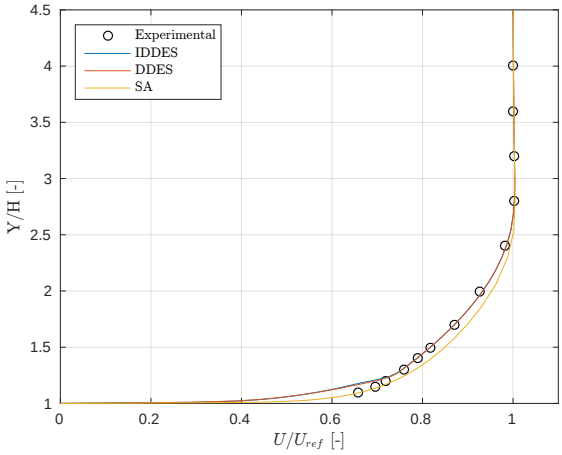

Figure 5.1.9: The velocity profile at x=-4.

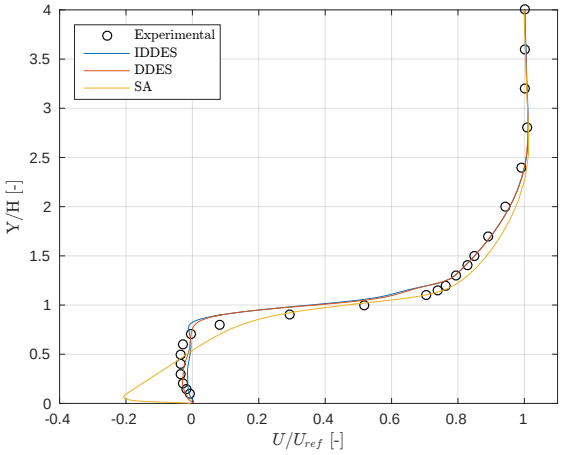

Figure 5.1.10: The velocity profile at x=1.

The velocity profile for x=4 and 6 are in Figs. 5.1.11 and 5.1.12. The results show that with IDDES and DDES the velocities are lower in the recirculation zone than with the SA model. The velocity profile for x=10 and the values for y+ along the lower wall are in Figs. 5.1.13 and 5.1.14. The IDDES model obtains the highest accuracy in predicting the velocity profile. The values for y+ show that the IDDES model results in a higher y+ even though the same mesh is used. This is because, as could be seen in the results for the friction coefficient, the use of the IDDES results in a higher wall shear stress. This higher wall shear stress, through the friction velocity, also results in a higher y+.

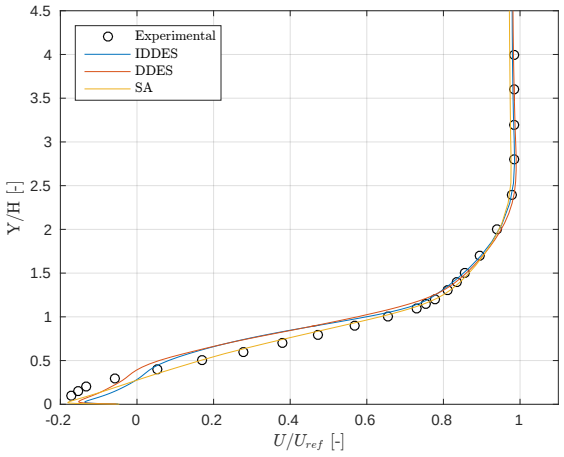

Figure 5.1.11: The velocity profile at x=4.

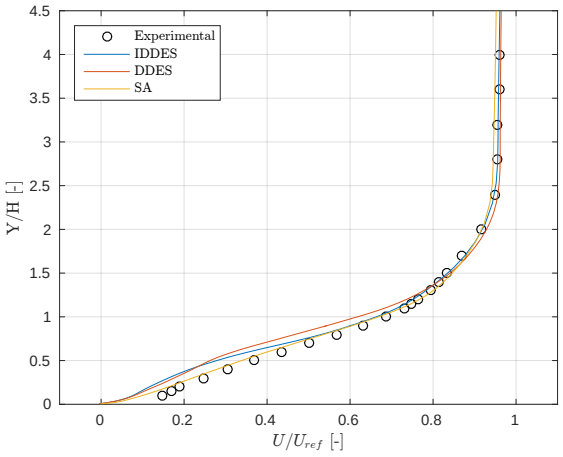

Figure 5.1.12: The velocity profile at x=6.

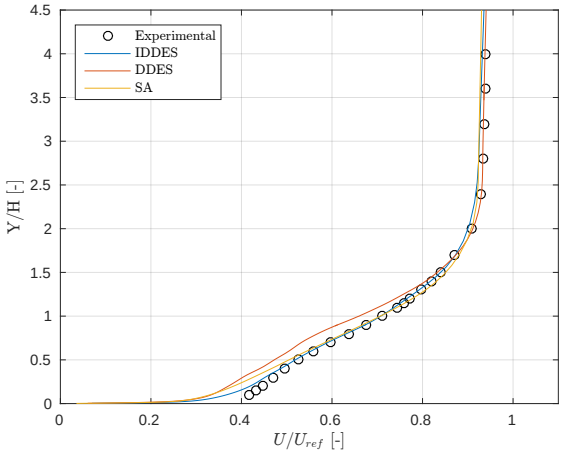

Figure 5.1.13: The velocity profile at x=10.

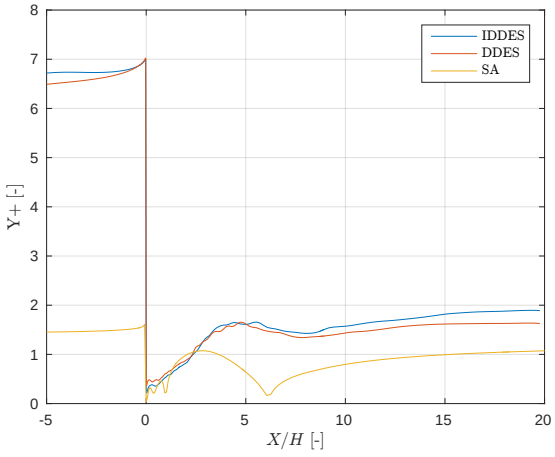

Figure 5.1.14: y+ value along the lower wall.

5.1.3 Interim Conclusion of the BFS case

The following interim conclusions can be made after performing the backwards facing step simulations.

- The IDDES model was more accurate in predicting the wall shear stress and therefore the friction coefficient than the DDES model. This was because the length scale was defined differently, now including the distance to the wall to include wall proximity effects. This new length scale counters the issues with the mismatching of RANS and LES content in the boundary layer. This mismatch could lead to an underprediction of the friction coefficient. This is because the Smagorinsky constant, which determines what structures are resolved and which are modeled, ideally has different values for different types of flow. With the new definition for the length scale, the model is better tuned to different types of flow in the boundary layer.

- The SA model performed better than the hybrid models in predicting the velocity profile at some locations. This is interesting because the hybrid models also have the SA model active near the walls. It is expected that the interaction between the RANS and LES content in the boundary layer with the hybrid methods is causing this. In effect, the velocity field in the RANS areas influences the velocity fluctuations in the LES field. This affects the Reynolds stresses and in order to maintain the balance of momentum, the velocity profile is negatively impacted.
- Grid refinement with hybrid methods is non-monotonic. This is due to two reasons. The first one is that with grid refinement the location where the switch takes place between RANS and LES and the whole model of the simulation changes. The second reason is that the IDDES length scale has two different definitions in the region between the wall and the free stream. During a grid refinement process the model might switch between IDDES length scale definitions. This means that when the grid is refined slightly then the length scale will change suddenly by a large amount.
- The hybrid methods are sensitive to unwanted random switching to LES in the boundary layer. This can lead to a reduction in eddy viscosity because the LES resolved more of the turbulence and modeled less. The best remedy that was found for this was to locally decrease the grid spacing, so that switching to LES was less likely to occur.

5.2 Heat Transfer Testcase

A testcase was done in order to gain with heat transfer and OpenFOAM. For this case a turbulent Poiseuille flow with a constant wall temperature difference as the thermal boundary conditions for the walls was chosen. Direct Numerical Simulation (DNS) data for the normalized temperature and velocity was available for this. The DNS computations have been performed by Kawamura et al [15].

A normalization procedure has been applied to the results in order to accommodate the governing equations and to analyze the flow. The flow properties have been non-dimensionalized by the friction velocity u_τ, the kinematic viscosity ν, the channel half-height δ and the friction temperature T_τ. The procedure can be found in the equations below:

$$u_i^+ = \frac{u^i}{u_\tau} \qquad\qquad T^+ = \frac{T}{T_\tau} \tag{5.1}$$

Here u_τ is the friction velocity and T_τ is the friction temperature. They are defined in the equation below. In the equations τ_w is the mean shear stress at the wall and ρ is the density and q_w is the mean heat flux at the wall.

$$u_\tau = \sqrt{\frac{\tau_w}{\rho}} \qquad\qquad T_\tau = \frac{q_w}{\rho c u_\tau} \tag{5.2}$$

The postprocessing for OpenFOAM to obtain y+ only returns the value for y+ of the first cell directly above the wall. The other values for y+ had to be computed directly. This was done using the friction velocity u_τ, the distance to the wall y and the kinematic viscosity ν. The formula

can be found below together with the expression for the fluid flow Reynolds number. Lastly, the definition of θ^+ is in 5.4.

$$y^+ = \frac{u_\tau y}{\nu} \qquad Re_\tau = \frac{u_\tau \delta}{\nu} \tag{5.3}$$

$$\theta^+ = \frac{T_{wall}}{T_\tau} - T^+ \tag{5.4}$$

The test case involved a channel flow with isothermal walls at different temperatures. Buoyancy effects will have to be neglectable as this is also the case with the combustion chamber and the solver that will be used cannot account for buoyancy effects. The testdata that was used is DNS data [15] that was generated for a channel flow with isothermal boundary conditions. The testdata includes the friction velocity and the mean temperature versus the wall normal direction.

In the figure below the domain for the test case can be found. As stated before the walls have isothermal boundary conditions. The inlet, outlet, front and back have cyclic boundary conditions. Next to this the flow has a relative low Reynolds number, in relation to the friction velocity, of $Re_\tau = 180$. This makes the testcase not very computationally demanding. The width of the total domain is 3.2 times the total height and the length is 6.4 longer that the total height. Furthermore the lower wall is being cooled and the upper wall is kept at a higher temperature.

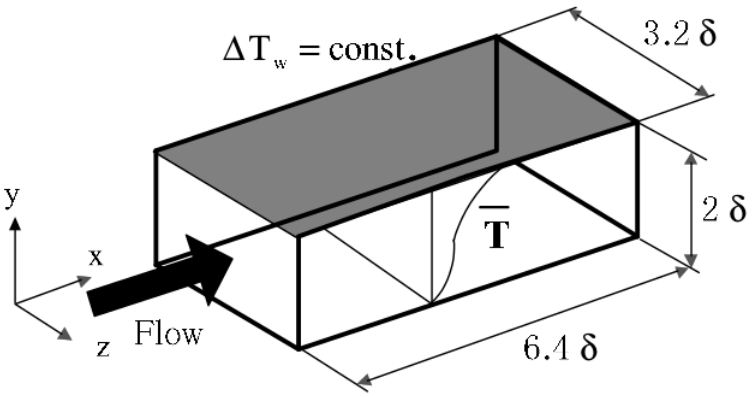

Figure 5.2.1: The domain of the heat transfer testcase [15].

In the following table the mean flow properties of the flow are given. The bulk velocity is denoted by u_b and the velocity in the center of the channel by u_c. The corresponding Reynolds numbers are Re_b and Re_c. The Re_b was used to size the domain. It is defined as $Re_b = 2\mathbf{u}_b\delta/\nu$, so when a kinematic viscosity is assumed of $1.78 \cdot 10^{-5}$ then a half channel height of $3.2 \cdot 10^{-3}$ can be computed

Re_τ	u_b	u_c	u_c/u_b	Re_b	Re_c	C_f
180	15.85	18.5	1.17	5705	3330	$7.98e \cdot 10^{-3}$

Table 5.4: Mean properties of the flow.

5.2.1 Mesh Design and Boundary Conditions

In this section the specifications of the mesh are given. Again details such as the number of cells, minimum angle, determinant and aspect ratio are stated. Next to this the boundary conditions for the SA and LES can be found. In Fig. 5.2.2 one of the LES meshes for the HTF testcase is shown. There is no mesh refinement in the streamwise direction since it is a channel flow and after the flow has settled it should be the same everywhere in the domain. The mesh refinement towards the walls, in order to obtain the desired y+ value, can also be observed.

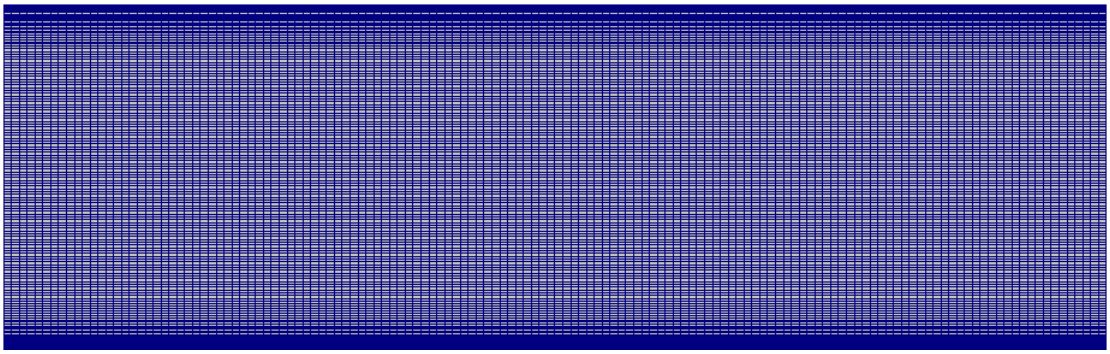

Figure 5.2.2: The LES mesh for the HTF testcase.

The values for the number of cells, minimum angle, minimum determinant and minimum aspect ratio are in Tab. 5.5. In Tab. 5.6 below the boundary conditions for the HTF simulation are stated.

Parameters	**CN 1 Case**	**CN 0.5 Case**	**Laminar Case**
Number of Cells [$\cdot 10^5$]	14.3	6	0.45
Maximum Angle [deg]	0	0	0
Maximum Aspect Ratio [-]	8.0	11.2	32
y+ [-]	0.48	0.55	0.2

Table 5.5: Mesh Specifications

Properties	**Inlet**	**Outlet**	**Upper Wall**	**Lower Wall**	**Sides**
Velocity	cyclic	cyclic	noSlip	noSlip	cyclic
Pressure	cyclic	cyclic	zeroGradient	zeroGradient	cyclic
Temperature	cyclic	cyclic	fixedValue: 328	fixedValue: 298	cyclic
nut	cyclic	cyclic	calculated: 0	calculated: 0	cyclic

Table 5.6: Boundary conditions for LES for the HTF testcase.

5.2.2 Results

During the simulations of the heat transfer case a number of challenges were encountered. It was found that the curve for the mean temperature was too low by a large margin. The value for the mean temperature at y+=1 should equal the Prandtl number, but it was around 0.5 while it should have been 0.71. This meant that the laminar thermal diffusivity was too high. At this point the error could be in solver, rhoPimpleFoam, the transport model, Constant, or in the post-processing procedure. While checking the code for rhoPimpleFoam, it turned out that OpenFOAM uses a different definition for the laminar thermal diffusivity than what is the norm, which was remarkable. OpenFOAM uses $\alpha = \lambda/c_p$ instead of $\alpha = \lambda/(\rho \cdot c_p)$. This would be kept in mind as a possible source of error later on.

Next, it was checked whether the error was in the post-processing. A laminar case was run to properly analyze the effects in the viscous sublayer. These results are in Figs. 5.2.3 and 5.2.4. The mean velocity and temperature profiles match very well in the viscous sublayer. The value for the mean temperature at y+=1 matches the Prandtl number. This shows that the issue was not it the procedure of non-dimensionalizing the results, but in the quantities themselves which are produced by OpenFOAM. Lastly, the laminar model is not able to produce turbulent results. So the focus of these results is only on the viscous sublayer and not on the log-layer.

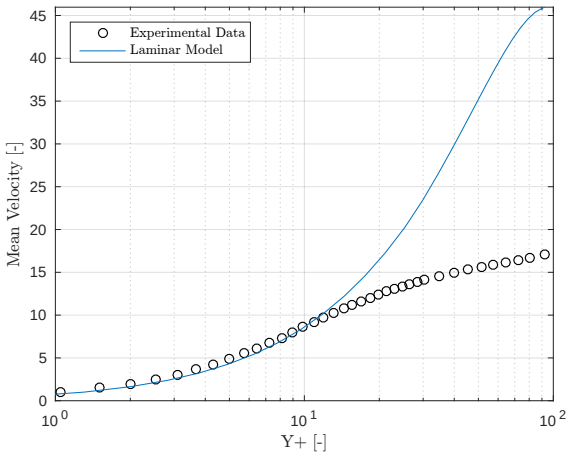

Figure 5.2.3: The mean velocity for the laminar case.

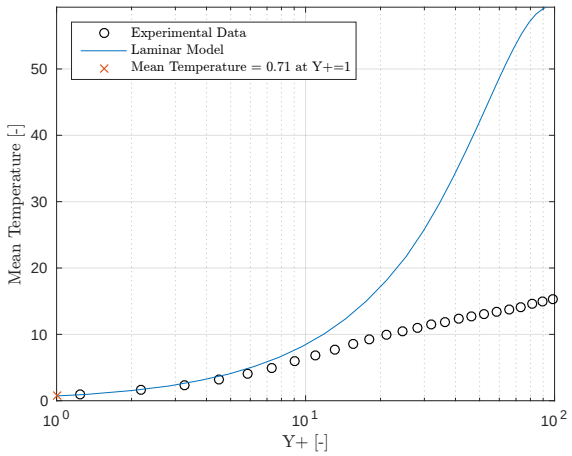

Figure 5.2.4: The mean temperature for the laminar case.

Following this, the values that were output by OpenFOAM and used to plot the figures were checked. The wall shear stress and the wall heat flux were computed by hand. The wall shear stress was the same as the number computed by OpenFOAM. The wall heat flux was around 30% lower however. This resulted in a lower T_τ and therefore a higher mean temperature. Another simulation of the same case was run, but with Sutherland as the transport model. The results for the wall heat flux computed with Sutherland was approximately the same as the value that was computed by hand, confirming that the value that was computed by hand should be correct.

At this point, the results showed that both the mean velocity and temperature were higher

than the experimental results. It indicated that the flow was too laminar and that the numerics that were used were too dissipative. While searching for the error in rhoPimpleFoam, it was found that if the pressure-momentum equation was set to be calculated more often, the simulation would become more stable. This was increased and the CN factor could then be set to 1, so that full second order time differentiation was employed. The results of this step are in Figs. 5.2.5 and 5.2.6.

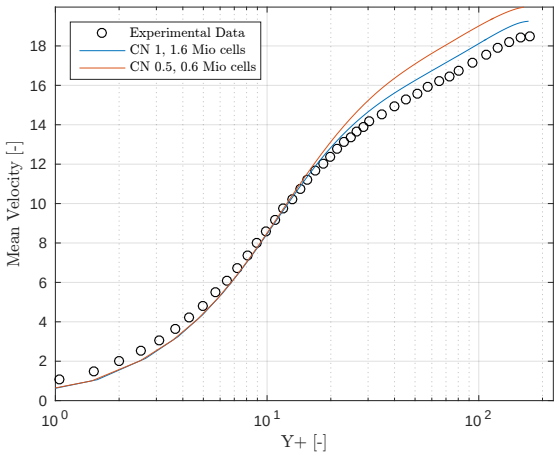

Figure 5.2.5: The mean velocity for the the cases with CN.

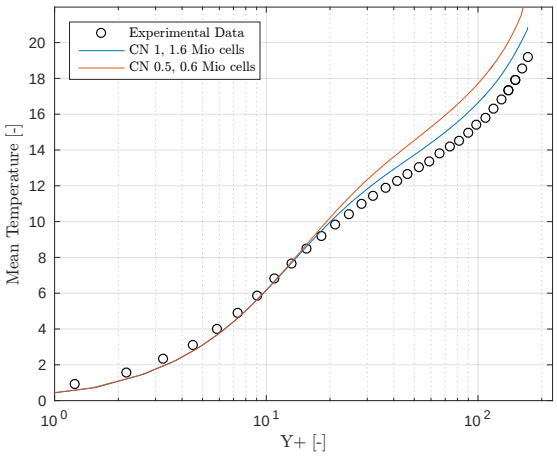

Figure 5.2.6: The mean temperature for the the cases with CN.

It can be seen how the results have improved with the increased order of time differentiation. The trend towards the experimental results is clear. The flow is still slightly too laminar in the center of the channel. It is expected that with more grid resolution and higher order numerics more accurate flow mechanics will be achieved and the experimental results can be matched. As for the results near the wall, it is possible the scaling of the subgrid model towards to wall is causing the results to be slightly off, but this would require further investigation. Lastly, the DNS data was obtained through a graphical selection tool because no numerical data was available. This could also have introduced a small margin of error.

5.2.3 Interim Conclusion HTF Case

In this section the interim conclusions that were found for the heat transfer case are presented.

- There is a strong suspicion that wall heat flux is incorrectly computed with OpenFOAM. This caused the T_τ to be too high and the mean temperature too low. It might be caused by the procedure by which the post-processing utility interacts with the information from the solver, rhoPimpleFoam.
- When the pressure-momentum is computed more often the simulation became more stable. This allowed for higher order time differentiation to be used. Unfortunately this was discovered after the combustion simulations had already been performed, but this knowledge could be used for future research.
- While increasing the order of the numerical schemes, the eddy viscosity increased. This in turn increased the turbulent thermal diffusivity and consequently lowered the mean temperature.

- Another possible culprit for the error could be that OpenFOAM computes the thermal diffusivity in a non-standard way. Whenever there is a deviation from the norm, an error may have sneaked in somewhere in the code.
- It was found that the Sutherland model produced better results in the viscous sublayer, but did not produce overall better results than the constant transport model. It was not completely certain, but it is suspected that the DNS experiments were also performed with the constant transport model.

CHAPTER 6

Results

In this section the results for the computations on the BKD-9 combustion chamber are stated. A mesh convergence study was performed and the simulation was compared to the experiment. Next to this, the mechanics of the flow were more closely analyzed.

6.1 Mesh Design and Boundary Conditions

In this section the mesh design is described in more detail. The front and side view of the mesh are in Figs. 6.1.1 and 6.1.2. The boundary conditions are in Tab. 6.1. For the faceplate and the posttip regions 17 cells with the finest mesh were used to ensure high enough resolution in the area where combustion takes place. Next to this, the mesh was refined near the wall so that a y+ of approximately 1 is obtained at the center of the wall, near the inlet. Due to changing flow conditions the value of y+ increases in the axial direction.

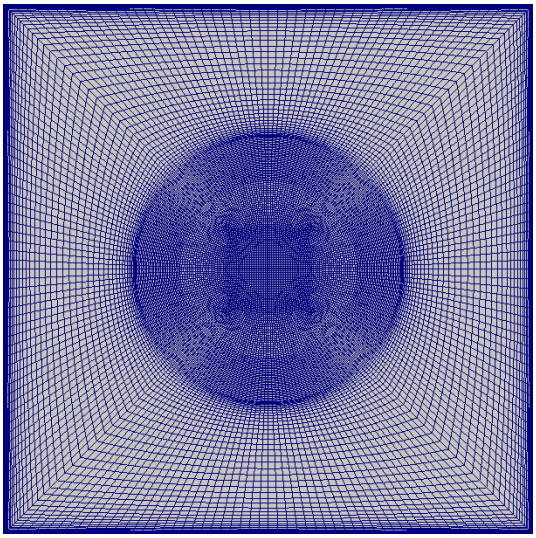

Figure 6.1.1: Front view of the finest mesh.

In Fig. 6.1.2 the side view of the complete mesh can be seen. The area around the inlet is heavily refined. This is because, as earlier stated, proper refinement of the flame near the inlet is of paramount importance to resolve the entire flame correctly.

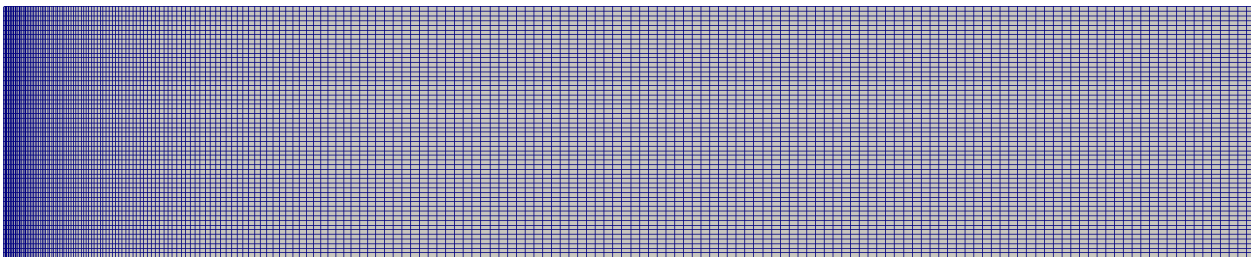

Figure 6.1.2: Side view of the finest mesh of the first 60mm.

In the following table detailed specifications can be found of the 4 meshes that were used. The value for y+ was taken after around the first increase, where the flame is anchored. The maximum angle is the maximum non-orthogonal angle between two cells. This maximum angle is relatively high due to the combined effects of circular blocks in the center of a square chamber and the narrowing domain in the nozzle area. Even though this number does not increase strongly between simulations, the number of cells with a high angle does become greater.

Parameters	**Design 1**	**Design 2**	**Design 3**	**Design 4**
Number of Cells [Mio]	20.3	12.7	5.7	1.7
Maximum Angle [deg]	71.4	71.2	71.2	70.9
Maximum Aspect Ratio [-]	232	117	78.4	88
y+ [-]	1.5	2.7	3.7	5.1

Table 6.1: Mesh Specifications

The boundary conditions for the simulations are stated in Tab. 6.2. The temperature boundary condition for the wall is set with the use of experimental data for the temperature in the axial direction of the combustion chamber. Furthermore, the fuel fraction needs to be specified, this is set to be 0 at the oxygen inlet and 1 at the methane inlet. The scalar dissipation rate, chi, is set to be *calculated: 0* at the inlets and *zeroGradient* on the other boundary conditions. Lastly, fuel fraction variance, varf, is *fixedvalue: 0* at the inlets.

Properties	**Inlet OX**	**Inlet CH4**
Velocity	filteredNIGMF massflow rate: 0.045 kg/s	filteredNIGMF massflow rate: 0.017 kg/s
Pressure	zeroGradient	zeroGradient
Temperature	fixedValue: 278	fixedValue: 269
nut	calculated: 0	calculated: 0
nuTilda	fixedValue: 5.55e-5	fixedValue: 5.55e-5
chi	calculated: 0	calculated: 0
varf	fixedValue: 0	fixedValue: 0
f	fixedValue: 0	fixedValue: 1

Table 6.2: Boundary conditions for the BKD-9 combustion chamber.

Properties	**Faceplate**	**Posttip**	**Wall**	**Outlet**
Velocity	noSlip	noSlip	noSlip	inletOutlet
Pressure	zeroGradient	zeroGradient	zeroGradient	waveTransmissive
Temperature	zeroGradient	zeroGradient	fixedValue: nonuniform List	zeroGradient
nut	nutkwallFunction: 0	nutkwallFunction: 0	calculated: 0	calculated: 0
nuTilda	fixedValue: 1e-10	fixedValue: 1e-10	fixedValue: 1e-10	zeroGradient
chi	zeroGradient	zeroGradient	zeroGradient	zeroGradient
varf	zeroGradient	zeroGradient	zeroGradient	inletOutlet
f	zeroGradient	zeroGradient	zeroGradient	zeroGradient

Table 6.3: Boundary conditions for the BKD-9 combustion chamber.

6.2 Complete Chamber

In this section the instantaneous and mean velocity, temperature and mixture for the entire chamber are reported. These are the results of the simulation with the finest mesh of 20.7 million cells. The axis in the axial direction is scaled by a factor two to make the images more visible.

The instantaneous velocity, temperature and mixture fraction are in Figs. 6.2.1, 6.2.2 and 6.2.3 respectively. The fuel and methane is injected with a velocity of about 160 m/s. As can be seen in Fig. 6.2.1, the velocity starts to increase strongly at about one third of the chamber length. At the same location in the instantaneous mixture fraction field a sharp decrease in fuel

can be observed. As combustion starts to develop, temperature increases, density decreases and the gasses in the chamber are accelerated. Further downstream the flame starts to thicken and hot gases reach the chamber walls, leading to a locally higher wall heat flux. It will be shown later that the highest values of the wall heat flux are found in these locations in the combustion chamber.

As expected the highest temperatures exist at the interface between the fuel and oxygen flows. Since this is where the reaction takes place, the temperature is raised here the most. Lastly, flame wrinkling can be observed at the near injector field where the flame is starting to develop. Flame resolution of the near injector region was found to be determining for the entire development of the flame. This will be discussed in more detail in Sec. 6.3.2. The mean velocity, temperature and mixture fraction are in Figs. 6.2.4, 6.2.5 and 6.2.6 respectively. In the mean velocity field a maximum velocity of 3300 m/s is found in the nozzle of the chamber, which corresponds to a Mach number of around 1.6.

In the mean temperature field a maximum temperature of 2860K is measured. The flame is stabilized by a recirculation zone consisting of hot gases between the oxidizer and fuel streams, this recirculation zone allows the flame to be anchored. A second recirculation zone exists in the corner of the combustion chamber, the mechanics of this zone will be discussed in a later chapter. Furthermore, a thermal boundary layer is present in the mean temperature field near the walls. This is due to the fact that a lower temperature of around 300K is imposed on the walls, therefore lowering the temperature in its direct vicinity. The thermal boundary layer also depends on the thermal diffusivity and so also on the viscosity. A boundary layer with a high viscosity also has a higher thermal diffusivity for the same Prandtl number.

A colder region of gases stretches in the center of the chamber up to one third of its length. The temperature is initially raised the most at the interface between the fuel and oxygen, which is closer to the walls in the near injector region. As the flame develops in the axial direction, the entire chamber is then heated more evenly. Unused fuel still leaves the combustion chamber. At the walls a flow remains with a mixture fraction of 0.35. To some extent this is realistic because not all the fuel will burn during combustion in the chamber. In the center of the channel a mean mixture fraction of 0.2 is present. This means that the mixture has fully burned, since the stoichiometric value for combustion here is 0.2.

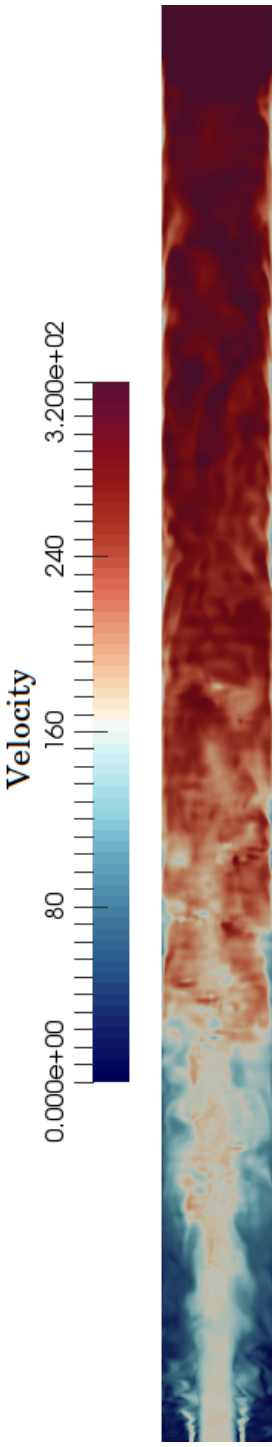

Figure 6.2.1: The instantaneous velocity, scaled by a factor 2.

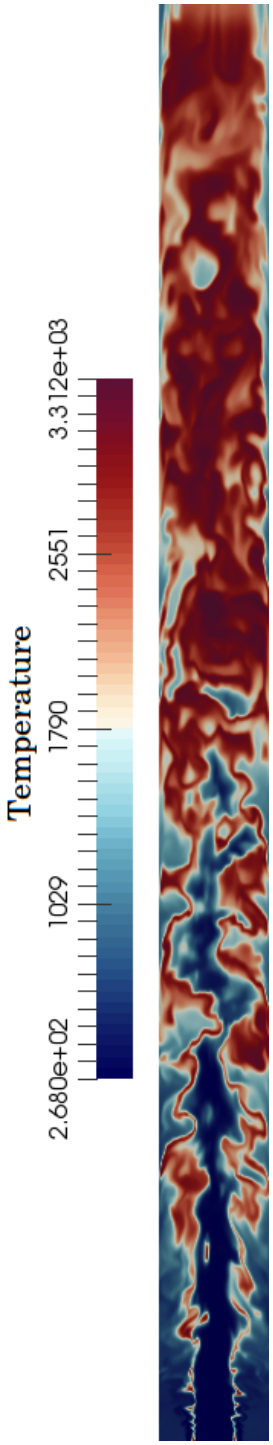

Figure 6.2.2: The instantaneous temperature, scaled by a factor 2.

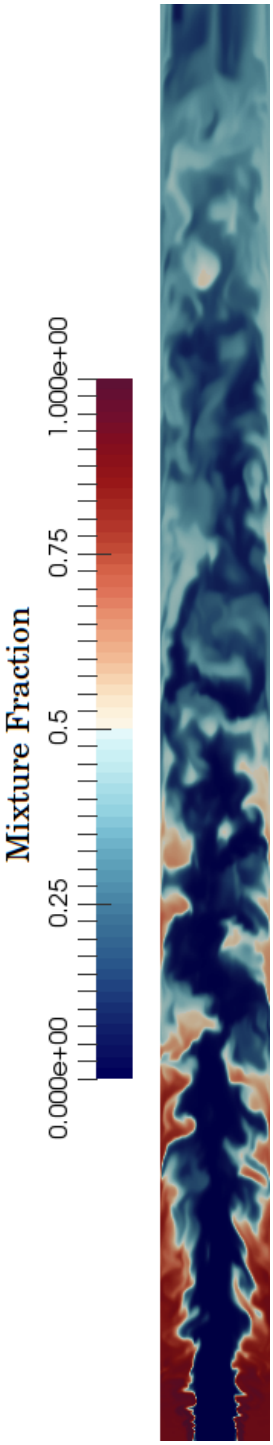

Figure 6.2.3: The instantaneous mixture fraction, scaled by a factor 2.

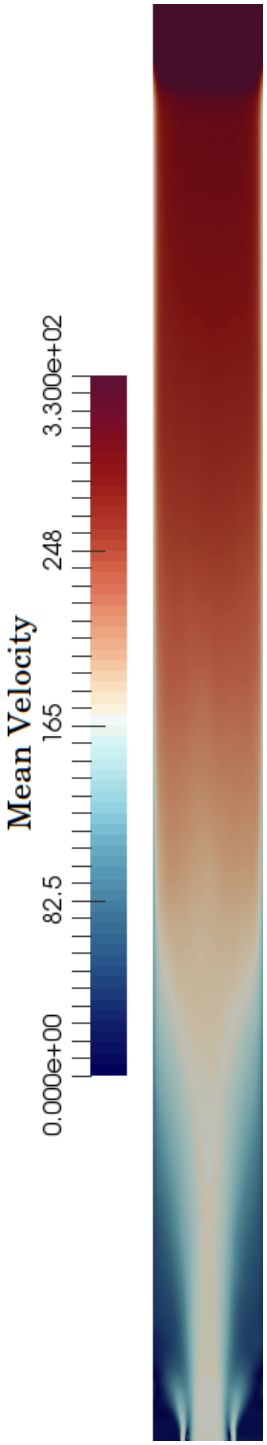

Figure 6.2.4: The mean velocity, scaled by a factor 2.

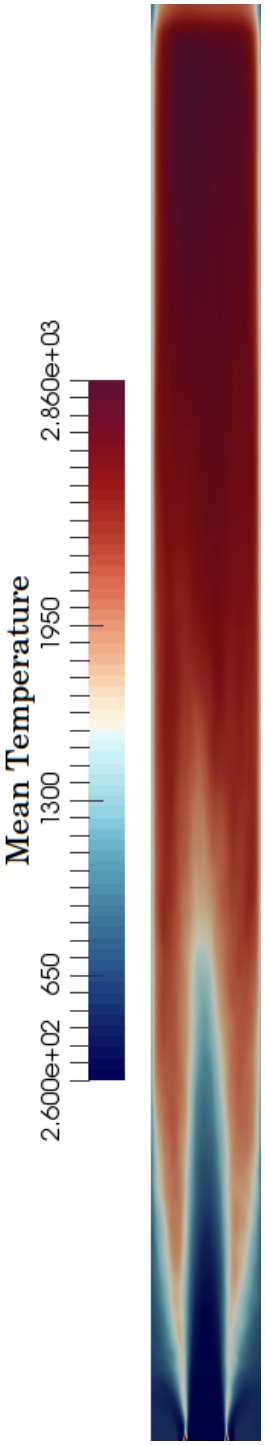

Figure 6.2.5: The mean temperature, scaled by a factor 2.

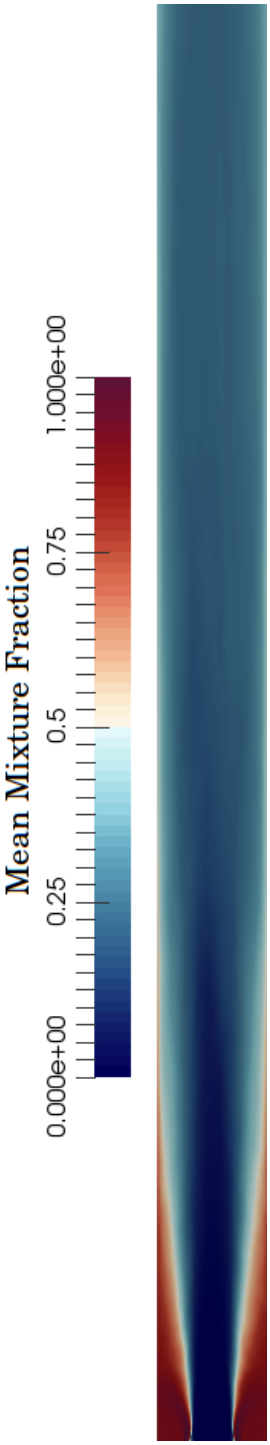

Figure 6.2.6: The mean mixture fraction, scaled by a factor 2.

6.3 Mesh Convergence Study

6.3.1 The Near Injector Region

In this section an investigation of the near injector region will be performed. This includes the region up to 30mm downstream of the faceplate. A comparison will be made for the finest and coarsest mesh. This is done to investigate the effect of mesh refinement on the structure of the flame. The instantaneous axial velocity, temperature and fuel fraction will be compared.

The instantaneous axial velocity for the fine and coarse mesh are in Figs. 6.3.1 and 6.3.2. The flow seems more laminar in the coarse simulation, with considerably less velocity variation in the direction perpendicular to the flow. Next, it can be seen that for the coarser case the recirculation zone is longer. Here this zone stretches for almost 30mm, while for the better resolved simulation the recirculation zone has an approximate length of 15mm. The length of the recirculation zone that is visible in the corner of the chamber is mainly determined by the mixing process of the oxidizer and the fuel and the inlet velocity. The finer mesh allows for better mixing and therefore a shorter recirculation zone.

In the fine case, lower velocities can be observed at the inlet. This is because the inlet boundary condition matches the velocity to the flow field properties at the inlet so that the correct mass flow rate is achieved. Because lower pressures exist for the coarser mesh at the inlet, due to less combustion, a higher inlet velocity is necessary to obtain the correct inlet mass flow rate.

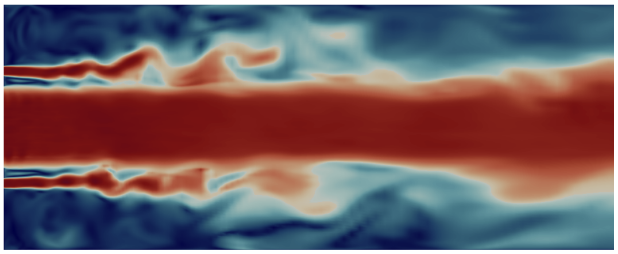

Figure 6.3.1: The axial instantaneous velocity for the finest mesh.

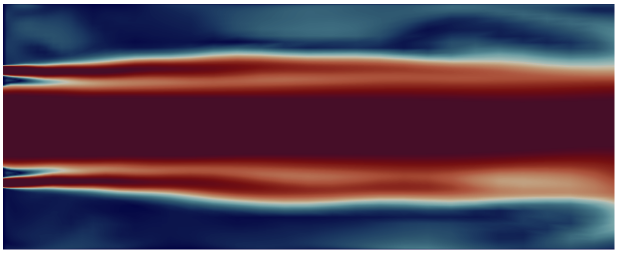

Figure 6.3.2: The axial instantaneous velocity for the coarsest mesh.

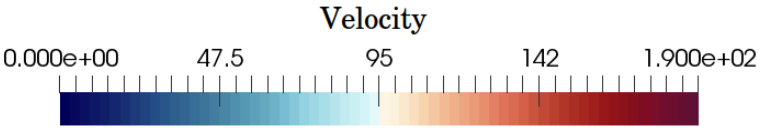

In Figs. 6.3.3 and 6.3.4 the comparison for the instantaneous temperature can be seen. Again the flame is better developed in the near injector area for the finer mesh. More flame wrinkling can be observed as there is more interaction between the fuel and the oxidizer. Furthermore, much higher temperatures can be observed in the fine mesh. Here the maximum temperature is around 3180K compared to the 1510K for the coarse case. The reason for this is that there are more resolved flow structures with the fine mesh and less subgrid contribution. This leads to a lower mixture fraction variance and a higher temperature. For the coarse case higher temperatures are observed further downstream. It can be concluded that the smaller cells of the fine mesh are

better capable of resolving the smaller flame mechanics. This higher resolution results in a better developing flame in the near injector area.

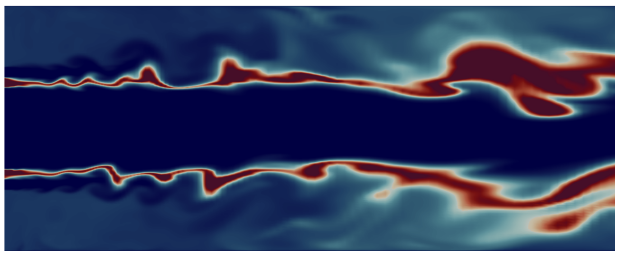

Figure 6.3.3: The instantaneous temperature for the finest mesh.

Figure 6.3.4: The instantaneous temperature for the coarsest mesh.

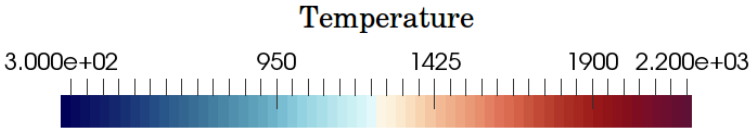

The instantaneous mixture fractions for the fine and coarse mesh are in Figs. 6.3.5 and 6.3.6. As seen before with the instantaneous temperature, there is significantly more interaction between the fuel and oxidizer flows. This is reflected in the observable reduction of the amount of fuel in the flow more downstream for the fine case.

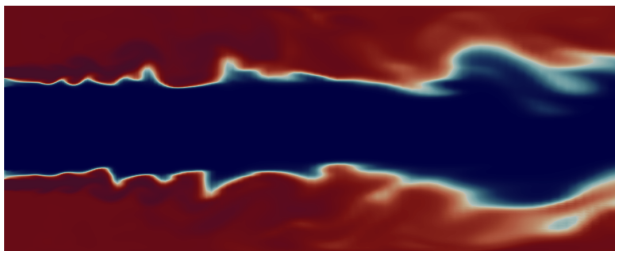

Figure 6.3.5: The instantaneous mixture fraction for the finest mesh.

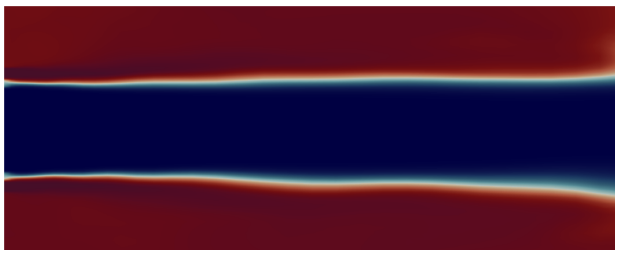

Figure 6.3.6: The instantaneous mixture fraction for the coarsest mesh.

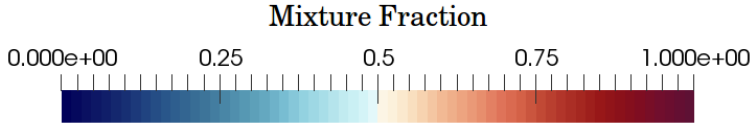

Injection Conditions

The velocity, density and momentum ratio of the propellants at injection conditions are important for the mixing process. In this case the conditions of the injection are designed so there is inadequate mixing, which results in a longer flame. This enables better analysis of the wall heat transfer. In Tab. 6.4 the velocity, density and momentum ratio of the propellants for the simulation with the finest mesh are stated. The momentum ratio between the oxygen and fuel is 3.65.

Propellant	**Velocity** $[m/s]$	**Density** $[kg/m^3]$	**Mass Flow** $[kg/s]$	**Momentum** $[kg \cdot m/s]$
Methane	168	12.9	0.017	2.856
Oxygen	168	25.6	0.062	10.416

Table 6.4: The injection conditions.

6.3.2 Scalar Dissipation Rate and Mixture Fraction Variance in the Near Injector Region

The mean scalar dissipation rate was analyzed for the finest and coarsest mesh in the injector region. These results are in Figs. 6.3.7 and 6.3.8. The values are scaled logarithmically because the scalar dissipation rate mainly has high values in the mixing region and lower values in the other regions. The scalar dissipation rate for the coarsest simulation was much higher. The highest value for the finest simulation was 2875 $\frac{1}{s}$. For the coarsest simulation this was 3970 $\frac{1}{s}$, or a difference of 38%. Four quantities have an effect on the scalar dissipation rate¿ These are the length scale, the mixture fraction variance, the effective viscosity and the density. The mixture fraction variance and the length scale have the most effect on the scalar dissipation rate.

The direct effect of the cell size on the scalar dissipation rate is that it increases with a smaller cell size. This is, as stated in the methodology section, when the distance between the oxidizer and the fuel is decreased in the flamelet, the strain and thus the scalar dissipation rate is increased. An overall decrease in the scalar dissipation rate leads to a higher flame temperature. Effectively, the scalar dissipation is still decreased with a smaller cell size. This is due to the effect of smaller grid resolution on the mixture fraction variance and then consequently again on the scalar dissipation rate. Better resolved combustion leads to a higher effective viscosity and therefore increases the scalar dissipation rate slightly. With increasing combustion the density is lowered, this increases the scalar dissipation rate with a small amount.

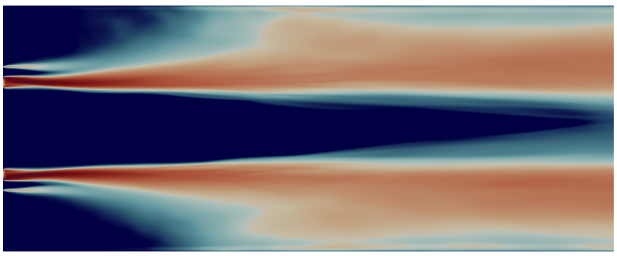

Figure 6.3.7: The mean scalar dissipation rate for the near injector region of the finest mesh.

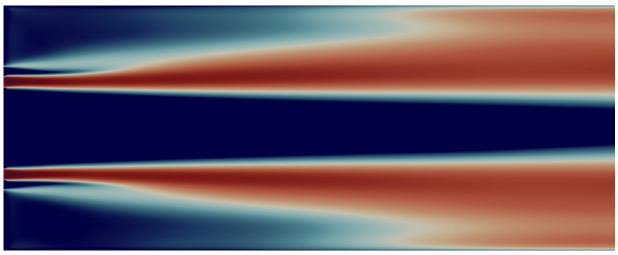

Figure 6.3.8: The mean scalar dissipation rate for the near injector region of the coarsest mesh.

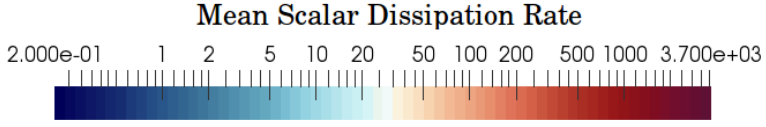

A smaller mixture fraction variance correlates to a smaller scalar dissipation rate, this is because with a smaller mixture fraction variance less strain is placed on the flame. The results for the near

injector region for the finest and coarsest mesh are in Figs. 6.3.9 and 6.3.10. Again the values are logarithmically scaled due to higher values in the mixing region and much lower ones in the other regions.

The reason that the mixture fraction variance is smaller for the finest mesh is that the instantaneous gradients are much better resolved here and with a smaller grid less sub grid effects need to be modeled with the mixture fraction variance. This resolves the flame structure better. The gradients of the mixture fraction iare smaller leading to a lower mixture fraction variance and a better resolved flame. Lastly, what can be seen in the figures is that the flame starts to develop much earlier for the fine mesh. In the case of the coarse mesh, the values for the mixture fraction variance start to grow in a larger axial direction and attain also higher values.

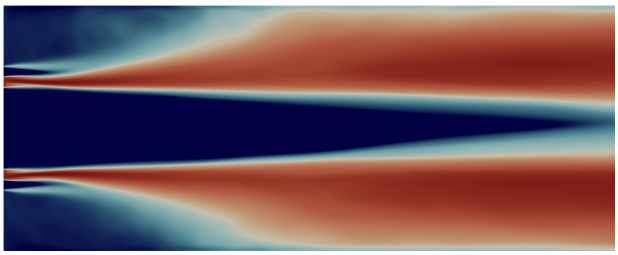

Figure 6.3.9: The mean mixture fraction variance for the near injector region of the finest mesh.

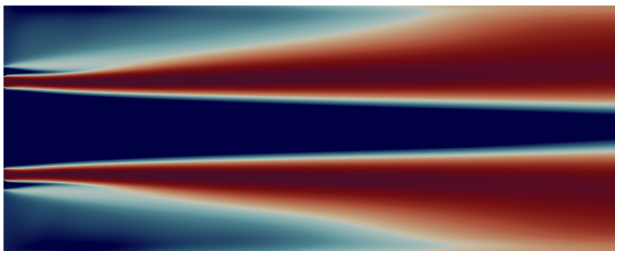

Figure 6.3.10: The mean mixture fraction variance for the near injector region of the coarsest mesh.

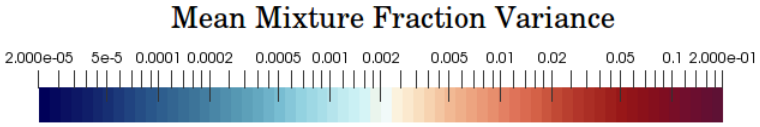

The mixture fraction variance has a larger effect on the maximum flame temperature than the scalar dissipation rate. A lower mixture fraction variance corresponds to a higher flame temperature, next to that it also leads to a lower scalar dissipation rate. The mixture fraction variance is used to model the non resolved fluctuations in the flamelet method. It serves as a subgrid model in the flamelet approach, as much of the small scale chemical and reaction processes occur on a smaller scale than on most hybrid RANS/LES grids. In the model the mixture fraction variance is used in the beta probability density function to compute the combustion variables, as described in the methodology for the flamelet. This PDF basically describes the time that the fluid spends in the vicinity of the state of the mixture fraction. A lower resolution grid requires higher quantities of the fuel fraction variance and it is less capable at computing the gradients of the flame, leading to lower flame temperatures.

6.3.3 Comparison with the Experiment

In this section the pressure and wall heat flux results of all four simulations will be compared to the experimental results. Next to this, the value for y+ will be analyzed. The averaged results for the pressure in the axial direction are in Fig. 6.3.11. It can be seen that increasing accuracy is

achieved with an increase in the number of cells. However, still for the simulation with the finest mesh the simulation underestimates the experimental data. This was due to the fact that for the simulations, the maximum number of cells was limited to 20 million. Furthermore, the simulation results show correspondence with the experiments in showing a peak in pressure at around 50mm. The end of the recirculation zone, where the flame anchors, is causing the peak in the pressure.

The pressure peak moves forward with grid refinement and slightly more to the inlet compared to the experimental results for the finest meshes. This is due to the shortening of the recirculation zone because of better mixing. Next to this, all the simulations show a gradual decrease in pressure towards the outlet. The combustion is accelerating the flow, resulting in a gradual decrease in pressure. The nozzle causes the sharp decrease in pressure. Lastly, the pressure increases more strongly in the near injector region for the finer meshes compared to the coarse mesh. This indicates that more complete combustion is achieved here for the finer meshes.

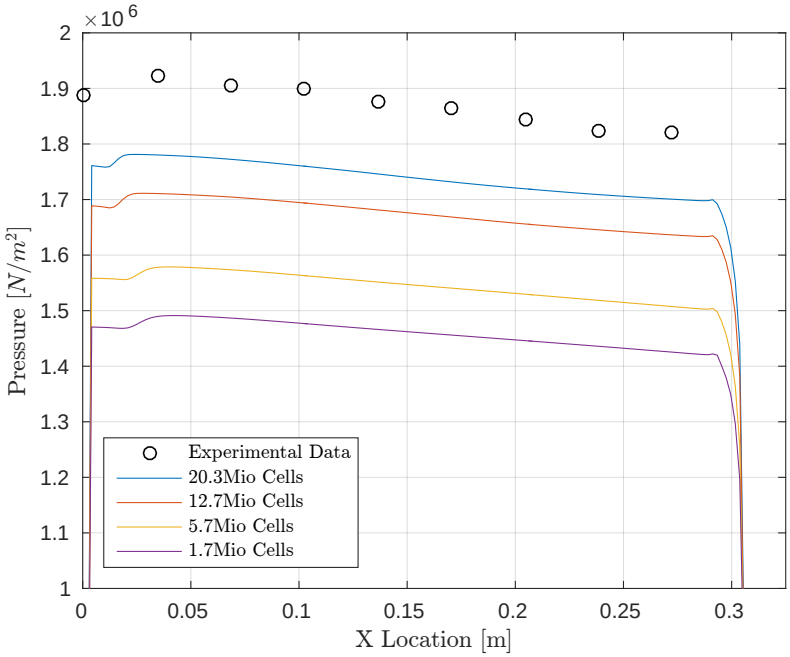

Figure 6.3.11: Circumferentially time averaged pressure results in the axial direction of the combustion chamber.

The time averaged results for the wall heat flux are in Fig. 6.3.12. Again, accuracy for the wall heat flux increases with better grid resolution. With the exception for the results for the coarsest and second coarsest mesh in the rear part of the chamber. This might be due to the fact that the effect of increased thermal diffusivity as a result of more viscosity in the larger RANS regions with the coarser mesh outweighs the effect that combustion is being less resolved with the coarser mesh. The increase in wall heat flux in the injector region is due to the flame developing and being anchored there.

Again it can be seen that with a higher grid resolution the flame is better resolved. This allows for better computation of the instantaneous gradients of the flow, this places less strain on the flame. As a result, the fuel fraction variance and scalar dissipation rate are lower for the finer meshes. The maximum flame temperature is higher for a lower fuel fraction variance and scalar dissipation rate. This leads to higher temperature gradients and therefore a higher wall heat flux for the finer meshes.

It is also good to bear in mind that the wall heat flux does not only depend on the temperature gradient but also on the thermal conductivity, k. This is a property of a material to conduct heat. Among other things this is done by properly modeling the species properties. In order to investigate this, the gas composition of the flow will investigated as well in a later section.

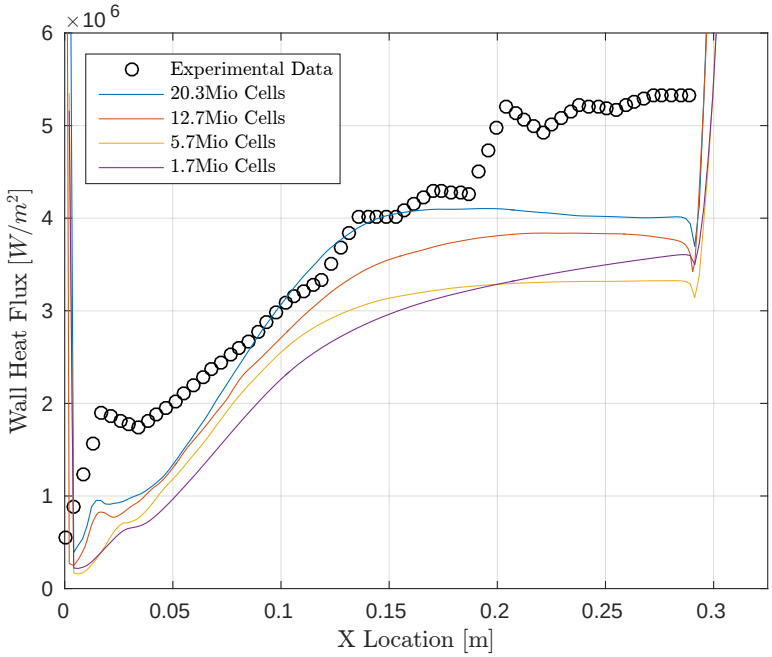

Figure 6.3.12: Circumferentially time averaged wall heat flux results in the axial direction of the combustion chamber

The computed values for y+ for all the simulations are found in Fig. 6.3.13. It can be seen that there is a sharp increase in the value for y+ where the flame is anchored. Following this, the y+ gradually increases towards the end of the combustion chamber. At the nozzle the value of y+ jumps again. Recalling the definition for y+, it depends on the friction velocity on the nearest wall, the distance to the wall and the kinematic viscosity. So these changes are mainly driven by variations in the wall shear stress and the density of the flow.

The parameter y+ is a useful tool in determining whether enough small flow structures are resolved near the wall. It was found that lowering the value for y+ lower than what it is with the finest mesh had an adverse effect on the results. It is suspected that this is a consequence of the mechanics of the SA model, where endless grid refinement towards the wall is not possible.

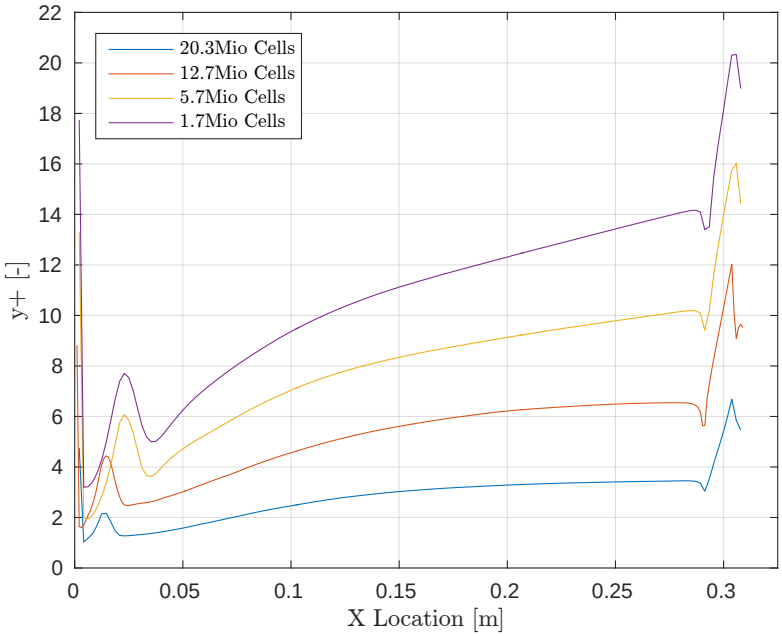

Figure 6.3.13: Time averaged y+ results in the axial direction of the combustion chamber.

6.3.4 Order of Convergence

A grid convergence study was performed to investigate the accuracy of the employed method while refining the grid. This was done for the pressure and wall heat flux as experimental data exists for these quantities. The error was computed per experimental data point and integrated along the length of the chamber. In the figures where the error is integrated, the curves for first and second order convergence is visualized as well. The expected order of convergence is slightly under two. This is because for the time differentation scheme a blending factor of 0.7 for CN is used. Gauss vanLeer is employed as the divergence scheme, this is a limited second order scheme as well. Lastly, grid convergence with a hybrid method is non-monotonic. Every time the grid is refined, the switching location for RANS and LES and the overall model for the simulation is changed.

The results for the grid convergence for the integrated pressure are presented in Fig. 6.3.14. It can be seen that the order of convergence for the simulations increases with grid refinement. The order of convergence of the last simulation is between one and two. For the third simulation around one and for the second simulation under one. It was shown that the mixing region had the largest effect on the fuel fraction variance and scalar dissipation, which in turn defined the flame temperature and structure. This means that if this region is refined more than the other parts of the domain, a higher order of convergence will be found.

The pressure and the wall heat flux are both results of the completeness of combustion in the chamber. This region was refined more than the rest of the chamber during grid convergence and it is expected that the increasing order of convergence is due to this. If no discretization errors have been made then the model errors will remain. These include the governing equations and

the turbulence modeling. The differences that are found here are most likely due to grid issues, turbulence modeling, limited averaging and other factors. In Fig. 6.3.15 the error for the pressure along the axial direction can be seen. The error stays approximately the same in the axial direction for all simulations. This corresponds to the results for the circumferentially averaged pressure in Fig. 6.3.11.

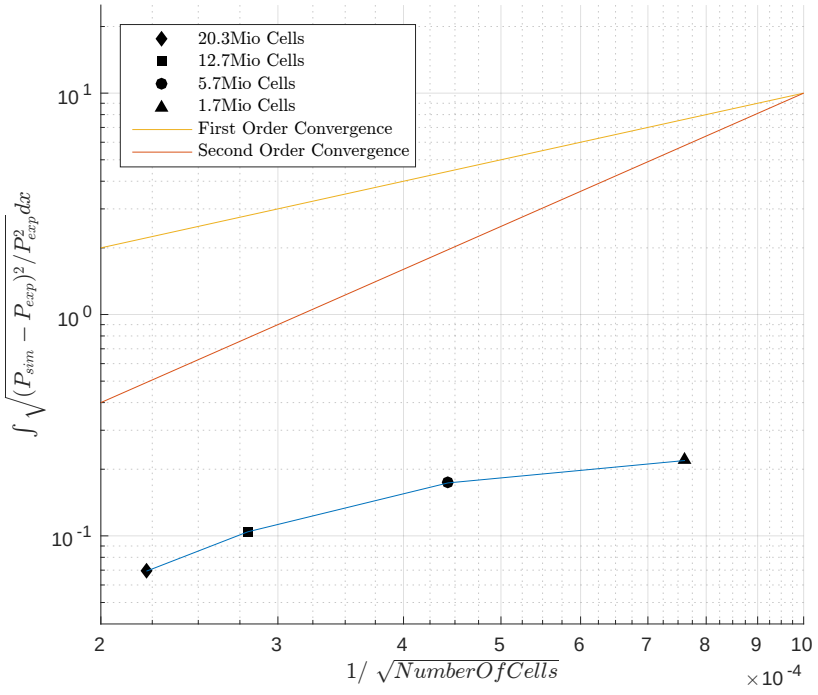

Figure 6.3.14: Grid convergence based on the integrated pressure in the chamber

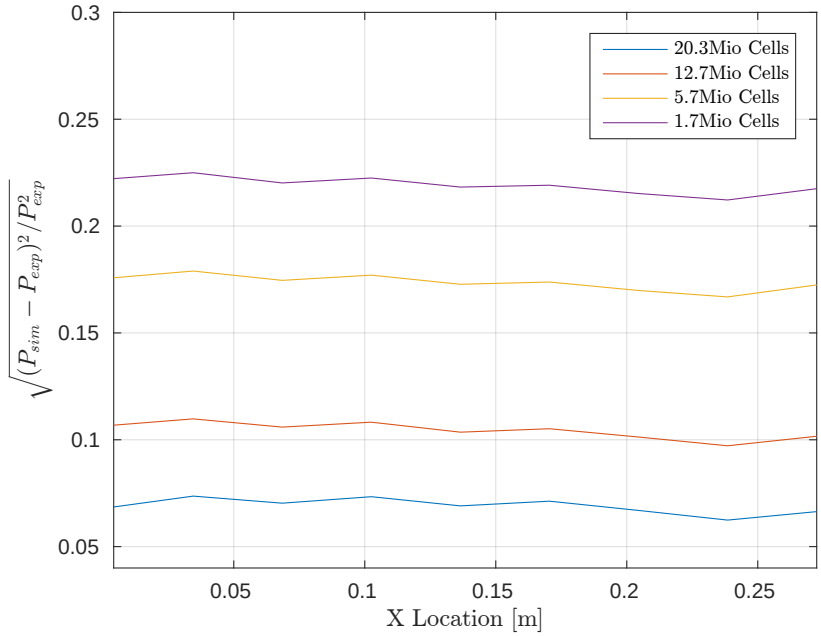

Figure 6.3.15: The error for the pressure in the axial direction.

The results for the grid convergence based on the integrated wall heat flux are stated in Fig. 6.3.16. The order of convergence increases here as well with increased mesh refinement. The curve that is obtained for grid convergence is very similar to the one computed for the integrated pressure. This is not very surprising since both values are directly dependent on the measure of completeness of combustion in the chamber.

The computed error for the wall heat flux in the axial direction can be found in Fig. 6.3.17. Again the error curves for all simulations follow a similar trend. Furthermore, it can be noted the highest error is to be found in the start of the chamber. This is the location where the flame develops and is anchored. It can be deduced that this region especially needs more grid refinement. The error is lowest in the middle of the chamber, around 100 and 150mm. Afterwards the error gradually climbs again.

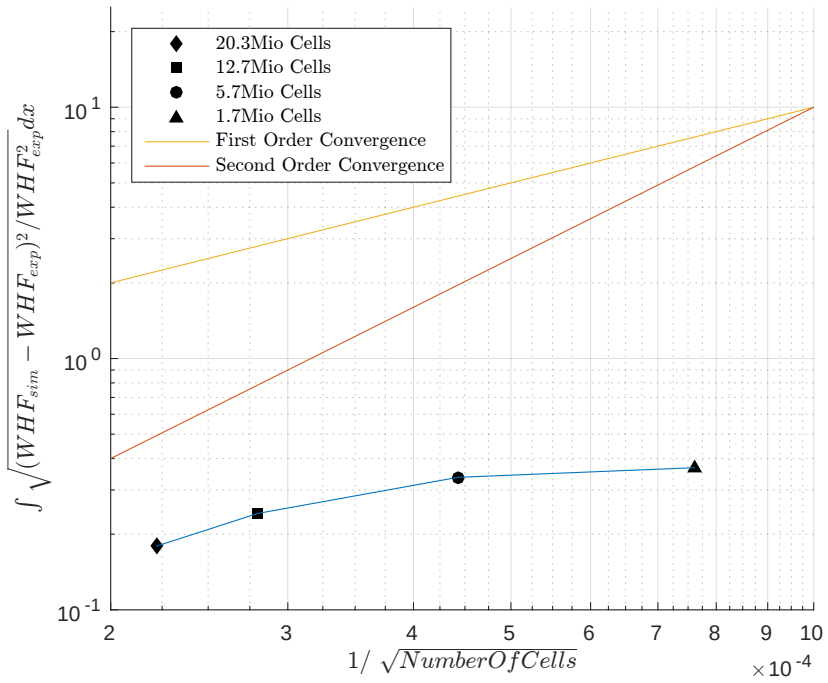

Figure 6.3.16: Grid convergence based on the integrated wall heat flux in the chamber.

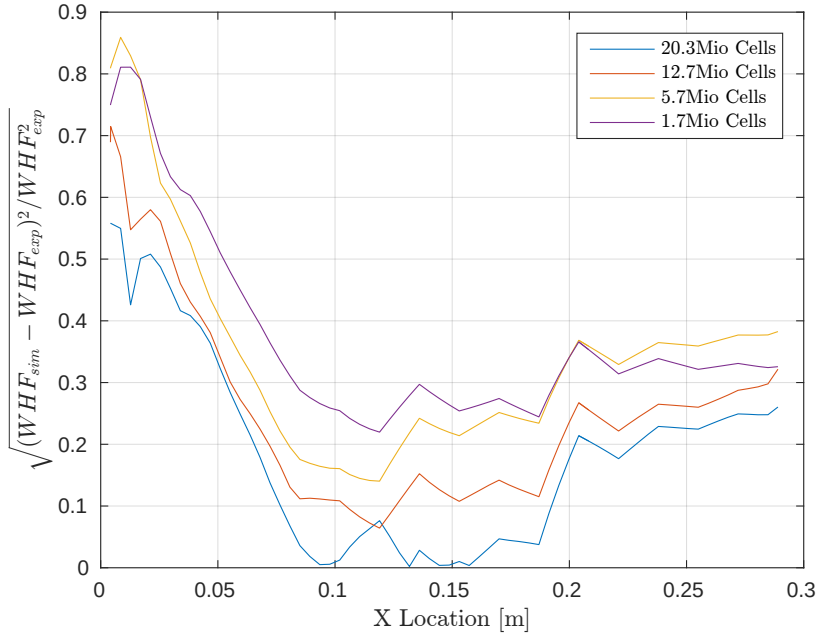

Figure 6.3.17: The error for the wall heat flux in the axial direction.

6.3.5 Expected Results with Further Mesh Refinement and Implications of Underprediction of the Flame

As could be seen in the previous results there is a clear trend in increasing accuracy in predicting the pressure and wall heat flux. The combustion has been underpredicted and results can be further improved with increased mesh resolution. This has the following implications:

- With further mesh refinement the eddy viscosity will decrease since more flow structures will be resolved instead of being modeled. This lowering of the eddy viscosity will lead to a lower turbulent thermal diffusivity. Next to this, it will have a slight effect on the scalar dissipation rate. With a decrease in eddy viscosity, the scalar dissipation rate will decrease slighty. This will lead to a higher maximum flame temperature.
- The turbulent heat flux consists of a resolved and a modeled contribution. The modeled contribution will decrease and the resolved contribution will increase with further mesh refinement. Overall, the turbulent heat flux is expected to increase.
- There is still unused fuel leaving the combustion chamber, completer combustion will most likely be achieved with further mesh refinement. Better resolving of the flame will lead to higher temperatures and wall heat flux.
- A reduction in the increase for the wall heat flux is observed in the results, while the wall heat flux in the experiments is still increasing. This can be due to underprediction of the temperature gradient or incorrect computation of the thermal conductivity.. A plateau in the wall heat flux near the outlet does not mean that increased wall heat flux results cannot be achieved. As can be seen in Fig. 6.3.12, this plateau in the wall heat flux also exists for the coarser simulations. Results will improve in two ways with grid refinement. First of all, the combustion will be better resolved. This will lead to less mixture fraction variance, less chemical modeling and higher flame temperatures. Better resolving of the turbulent structures will lead to more resolved fluctuations, more heat distribution due to turbulence and better mixing.
- For an underresolved flame the scalar dissipation rate and the mixture fraction variance are still too high. This means that the scalar dissipation places too much strain on the flame and lowers the maximum temperature. A high value for the mixture fraction variance means that more of the small scale chemical and processes are modeled. The gradients of the flame are less well resolved in this case and also leads to a lower flame temperature.
- The corner recirculation zone will decrease in size. This is due to two reasons. First of all, with better mixing more complete combustion will be achieved quicker. This caused the flow to expand and the recirculation zone to become shorter. Secondly, more complete combustion will occur at a shorter distance downstream of the inlet. This will lead to an increase in pressure and the boundary condition will decrease the inlet velocity to match the mass flow rate. This reduction of the inlet velocity will in turn lead to a shorter recirculation zone.

In previous studies on this combustion chamber with only LES as the turbulence model, the peak for the wall heat flux at the inlet was successfully obtained [27]. Mesh convergence with hybrid methods could lead to these same results, with a thin layer of RANS at the walls passing through

most of the heat flux generated in the LES regions. The maximum order of convergence would be slightly under two, since both divergence and time schemes are limited second order. As stated before, convergence in the mixing region has the most effect since this is the region that defines the structure of the flame.

6.4 Investigation of Flow Mechanics

6.4.1 3D Streamlines

The streamlines of the axial mean velocity for the fine and coarse mesh are compared. This is done in 3D and can be seen in Figs. 6.4.1 and 6.4.2. The observation that was made before that the recirculation zone is much shorter for the fine mesh is reaffirmed in these figures. Furthermore higher negative velocities exists with the fine mesh. For the fine mesh these are -62 m/s, compared to -46 m/s with the coarse mesh. Next to this, there are 2 corner recirculation zones for the coarser simulation. One around 10mm and the other one around 20mm in the axial direction.

The higher mixing of the flows for the finer mesh that was stated before can be seen again. The streamlines of the finer mesh show more mixing and variation in velocities in the y and z directions. The streamlines that originate in the fuel inlet also can be seen to move more in the area directly downstream of the oxygen inlet. Again the streamlines for the coarse case seem to be much more laminar. Lastly, expansion due to combustion can be seen. The combustion increases the temperature which in turn leads to a lower density and higher velocities.

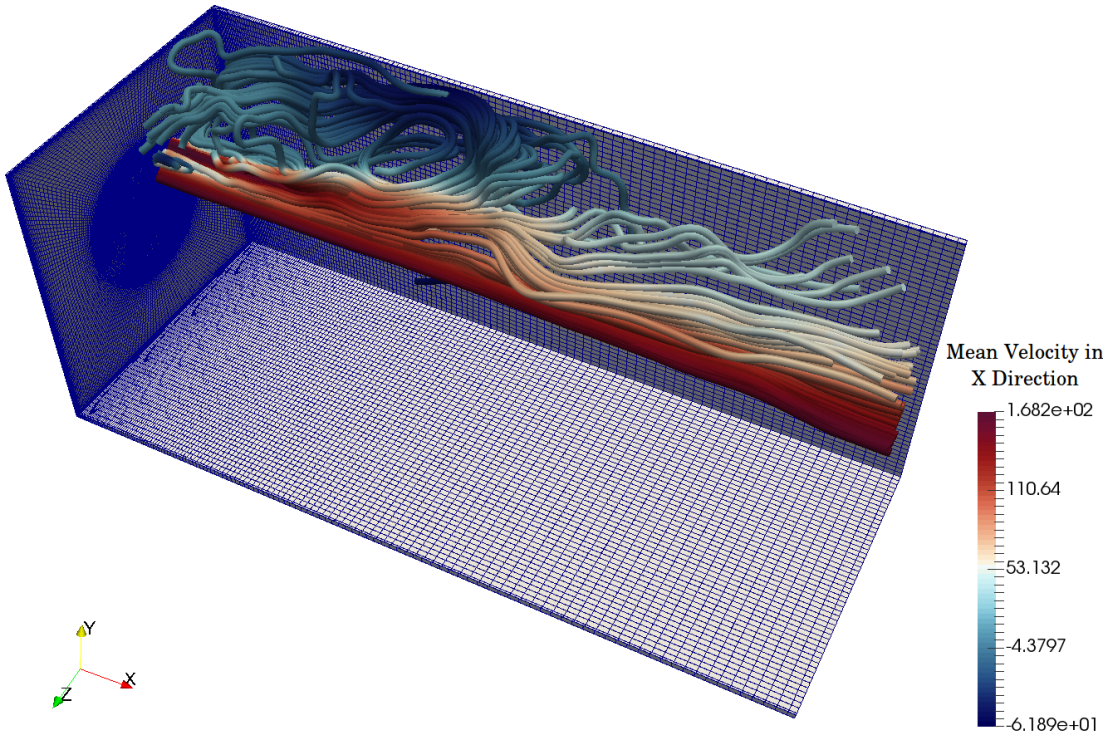

Figure 6.4.1: 3D streamlines of the axial mean velocity for the finest mesh.

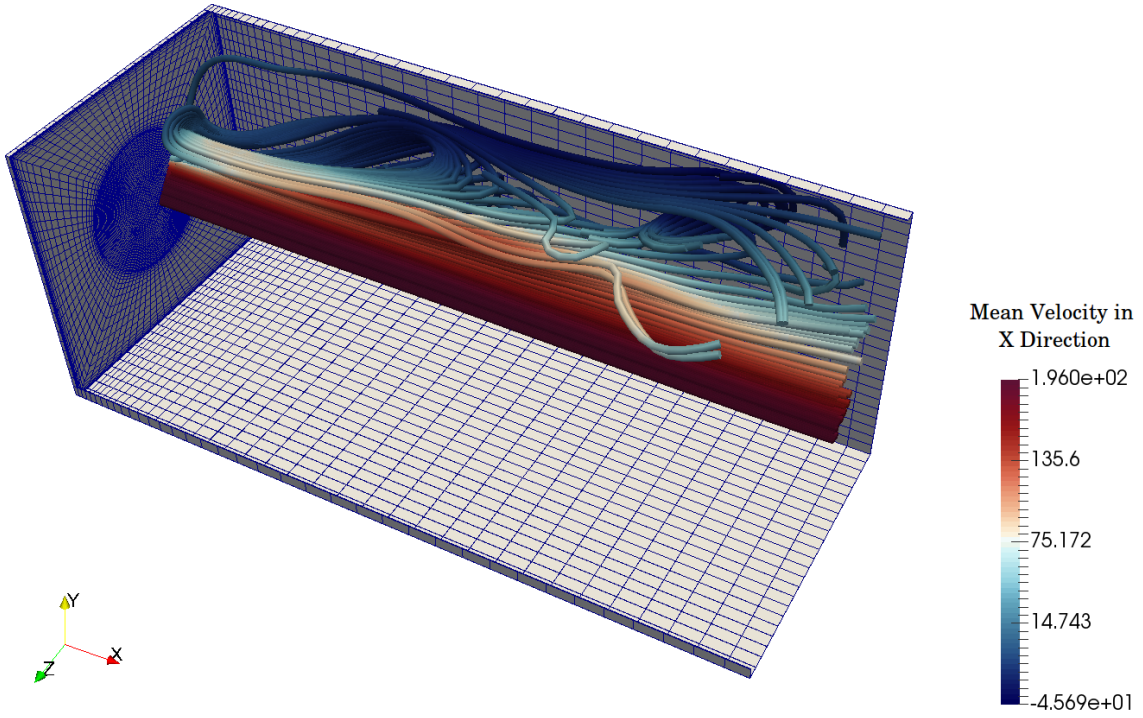

Figure 6.4.2: 3D streamlines of the axial mean velocity for the coarsest mesh.

6.4.2 The Recirculation Zones and Flame Stability

Two recirculation zones exist in the near injector area. The larger one which is visible in Figs. 6.4.1 and 6.4.2 is caused by the square corner geometry of the combustor. The length of this is influenced by a number of parameters. These are the inlet velocity of the reactants, mixing of the oxidizer and fuel and the subsequent combustion. This results in a higher temperature, lower density and higher velocities. The finer mesh has a lower inlet velocity imposed by the inlet boundary condition. This coupled with the higher mixing and more rapidly developing combustion results in a shorter corner recirculation zone.

The other recirculation zone is found at the faceplate, the wall separating the oxygen and methane inlets. This exists due to the geometry of the chamber in relation to the injectors. This recirculation zone plays a large role in flame stability. High temperature flow and ignitable products are supplied here by the recirculation zone as hot products are recirculated and meet fresh reactants. This creates favorable conditions for the ignition of newly injected propellants. This recirculation zone allows the flame to anchor at this location and stabilizes it.

The flame stability is mainly influenced by two components. The first is the recirculation zone at the faceplate. As stated before, an ignitable mixture is supplied here to the flame by the recirculation zone. This allows the flame to be anchored at this location and stabilizes it. It was found during grid refinement that the recirculation zone was increased in size. This longer recirculation zone allows for better mixing and for the ignitable mixture to be presented to the flame over a larger area.

The other component that has an influence on the flame stability is the scalar dissipation rate. As mentioned in the methodology section, this term defines the flame structure. This quantity accounts for strain effects on the flame and is linked to the velocity structure of the flame. With increasing scalar dissipation rate the flame will be strained until combustion is no longer possible and the flame is quenched. This extinguishing of the flame under influence of high scalar dissipation rates was observable in Fig. 4.2.3. It can be seen that for the scalar dissipation rates which are present in this flame, quenching of the flame is no threat.

6.4.3 Thermal Conductivity

The heat flux, $\dot{\boldsymbol{q}}$, is computed using the thermal conductivity, λ, and the temperature gradient, ∇T, with the thermal conductivity acting as the scaling factor for the temperature gradient. The thermal conductivity is a property of the species which are present in the chamber. Therefore, the overall thermal conductivity in the chamber greatly depends on the concentration of the species and their respective thermal conductivities. The thermal conductivity increases with greater temperatures, due to more molecular interaction in the gas. In order to analyze the heat flux further the thermal conductivity is visualized in Fig. 6.4.3, the instantaneous temperature in Fig. 6.4.4, the instantaneous concentration of H2 in Fig. 6.4.5 and the instantaneous concentration of CO2 in Fig. 6.4.6.

It can indeed be seen that higher temperatures lead to higher thermal conductivity. However, the higher temperatures do not account for all the increased thermal conductivity in the domain. Especially near to the walls, where lower temperatures exist, the thermal conductivity still has high values. This is explained by the presence of certain gases in these areas. Hydrogen, a gas with a relatively high thermal conductivity has high concentrations in areas with high thermal conductivity but lower temperatures. It can directly be seen how the presence of the highly thermal conductive gas hydrogen is raising the overall thermal conductivity.

Another gas, CO2, is shown to highlight the effect of the presence of hydrogen on the thermal conductivity. CO2 is a direct product of the combustion and can be seen in high concentration on the interface between fuel and oxidizer. H2 is a byproduct of other reactions and it has higher concentrations where there is less CO2. In these figures it is shown that the overall thermal conductivity is dependent on the temperature and the concentration of species in the chamber. The overall thermal conductivity, temperature and concentrations of most reactant species was found to increase with grid refinement due to better resolving of combustion in the chamber. For the proper functioning of combustion models, properly computing the concentrations of reaction products is of paramount importance to obtain correct results, as the figures show.

For completeness the thermal conductivities of a number of individual species are presented in Tab. 6.5. These values were found on the website of the National Institute of Science and Technology [28]. Unfortunately no data was available for the temperatures that are present in the chamber, but it does give information about the relative thermal conductivities of the species. For higher temperatures the thermal conductivities will increase. The testdata is for a pressure of 1.8 MPA, around the same pressure as for the finest mesh. Hydrogen has the highest thermal conductivity when compared to the other species, even when accommodating for the lower temperatures of CO

and CH4.

Species	H20	H2	O2	CO	CO2	CH4
Thermal Conductivity $[W/m \cdot K]$	0.13	0.52	0.08	0.04	0.075	0.094
Temperature $[K]$	1250	1000	1000	500	1100	620

Table 6.5: The thermal conductivity for a number of species.

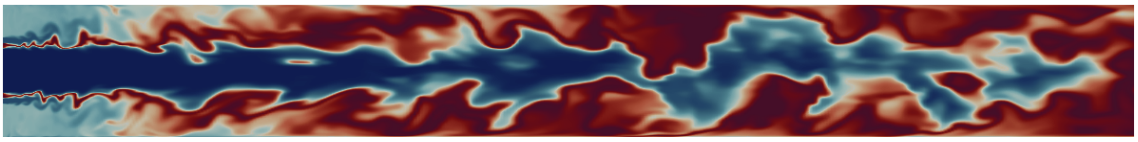

Figure 6.4.3: The instantaneous thermal conductivity for the first 150mm of the finest mesh, scaled by 1.5.

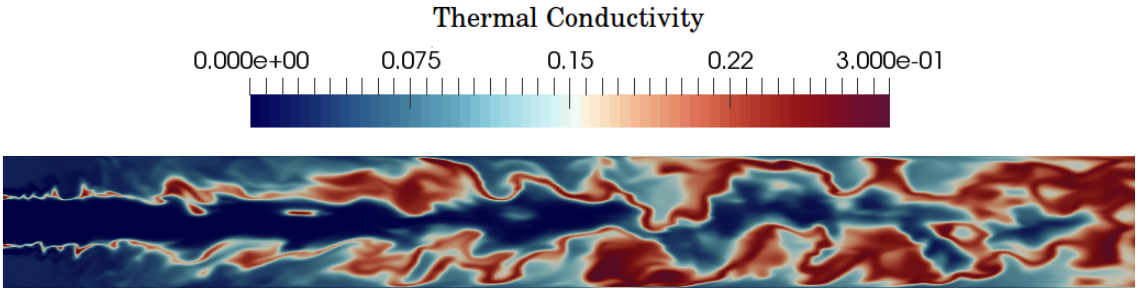

Figure 6.4.4: The instantaneous temperature for the first 150mm of the finest mesh, scaled by 1.5.

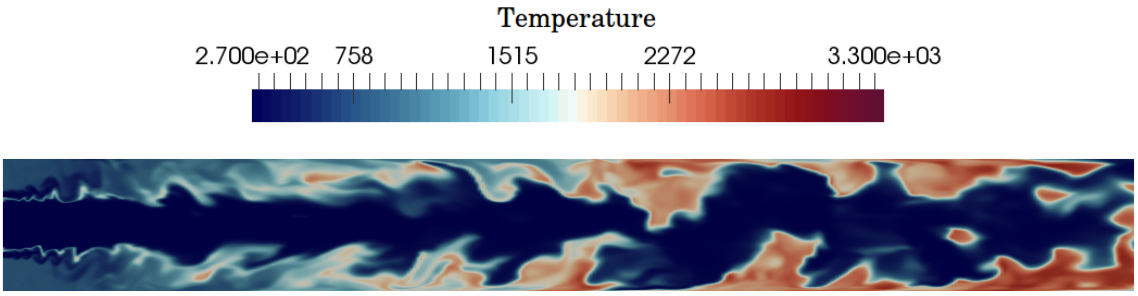

Figure 6.4.5: The instantaneous concentration of H2 for the first 150mm of the finest mesh, scaled by 1.5.

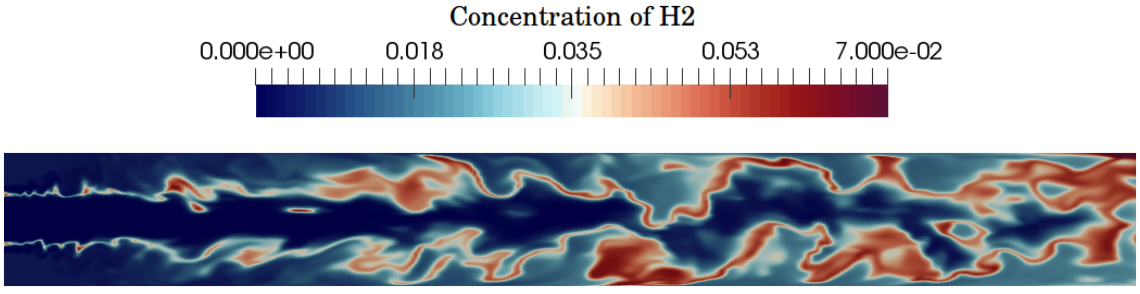

Figure 6.4.6: The instantaneous concentration of CO2 for the first 150mm of the finest mesh, scaled by 1.5.

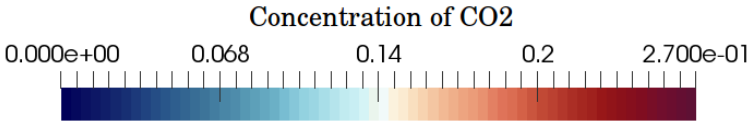

6.4.4 The Damköhler Number

One of the assumptions of the SLFM is that the Damköhler number must be high. The Damköhler number characterizes the behavior between mixing and reacting components in a mixture. It is defined as the ratio between the turbulent and the chemical timescale, or τ_f/τ_c. For a high Damköhler number the flame preserves a laminar shape inside of the turbulent structures. If this is not the case then the turbulent structures interact with the flame, causing flame wrinkling, instabilities at the flame front and the laminar flame structure to be distorted [29]. In more extreme cases the turbulent structures can penetrate the flame and destroy it.

When the flamelet is not laminar anymore, the fluctuations of the species mass fractions and the reaction rate cannot be assumed to be very small. This means that the assumption to only use the mean values of these quantities in the entire flamelet is not valid anymore. In order to check this, the Damköhler number for the combustion case was computed. For the SLFM model to be justified, the following should hold true.

$$Da = \frac{\tau_f}{\tau_c} >> 1 \tag{6.1}$$

With turbulence theory it is assumed that turbulent processes occur over a large range of scales. With this in mind, the integral turbulent timescale is very important because it represents the turbulent scales with the highest turbulent energies. The scale does not represent the largest turbulent scale, but it is in the same order of magnitude [30]. The Kolmogorov length scales represent the turbulent time scale on the other side of the spectrum. Most of the turbulence will take place between these two time scales. The Damköhler number of both scales will be analyzed. The integral time scale, t_{int}, and the Kolmogorov timescale, t_{kol}, are defined as follows:

$$t_{int} = \frac{k}{\epsilon} \qquad\qquad t_{kol} = \sqrt{\frac{\nu}{\epsilon}} \tag{6.2}$$

Here k is the turbulent kinetic energy and ϵ is the turbulent dissipation rate. Between these two scales the most important turbulent processes take place. In the regions in the combustion chamber where the velocity gradient is very high, the turbulent timescales decrease rapidly. Information on the chemical time scale is not available with the SLFM model, since it is assumed that the chemical reaction is instant.

Furthermore, the turbulent and chemical processes do not have one distinct timescale but it varies throughout the domain with a very strong dependency on temperature. Often detailed reaction mechanisms are required to precisely compute it. To estimate the chemical timescale several methods exist. In [31] it is shown by Prüfert et al. that the chemical timescale can be approximated with the progress variable, C, and the chemical production rate ω_c. The definition is in Eq. 6.3.

$$\tau_c = \left.\frac{\Delta C}{\omega_c}\right|_{st} \tag{6.3}$$

The progress variable is defined as the sum of the mass fractions of the main species. These are taken as the sum of the main species CO2, H20, H2 and CO, as well as the radicals OH, H and O. ω_c is the chemical source term. It is obtained by disturbing the laminar flamelet with a small ΔC

and then measuring the derivative of the chemical production rate. For the flamelet used in the thesis this procedure has resulted in a chemical time scale of $3.36 \cdot 10^{-8}$.

In Tab. 6.6 the computed Damköhler numbers for the integral and Kolmogorov length scale are reported. The timescale for the smallest turbulent structures is 107, which shows that the assumption that the flame structures are laminar holds. Although only the smallest turbulent structures can penetrate the flames, interaction between the turbulent and chemical components occurs across the whole turbulent spectrum, which is why the Damköhler number for the integral timescale is computed as well for completeness.

Properties	**Timescale** $[s]$	**Damköhler number**
Kolmogorov timescale	$3.6 \cdot 10^{-6}$	107
Integral timescale	$5 \cdot 10^{-4}$	14,880

Table 6.6: The timescales and Damköhler numbers for the integral and Kolmogorov timescales.

6.4.5 Cross Section of the Flame

In this section the cross sections of the flame shape at multiple locations along the combustion chamber are analyzed. This is done to gain a deeper understanding of how the flame structure is developing in the axial direction. In the following figures the cross sections of the mean values for the temperature and fuel fraction are given. They are taken at locations x = 5, 50 and 100.

In Figs. 6.4.7, 6.4.8 and 6.4.9 the results for the cross section of the mean temperature are shown. First of all it can be seen how in the near injector region flame shape is still circular due to the shape of the injector. More downstream, at x = 100, the flame shape is markedly square due to the shape of the combustor. Combustion is not complete yet which can be seen in the colder core. The areas with the lower temperature are in the center and near the walls. This is due to the fact that the interface of the fuel and oxidizer will lead to highest temperature. The flame front developing in the axial direction will reach these places last. Lastly, a thermal boundary layer can be seen in the figures. This is due to enthalpy losses at the walls caused by the lower wall temperatures and increased thermal diffusivity in the boundary layer.

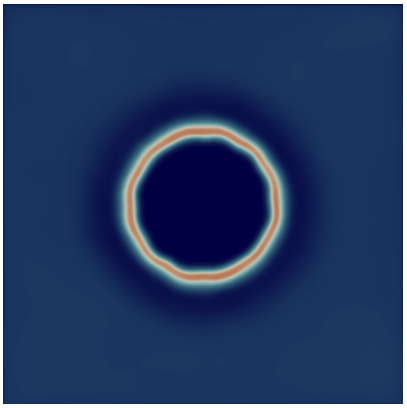

Figure 6.4.7: Mean temperature at x=5mm.

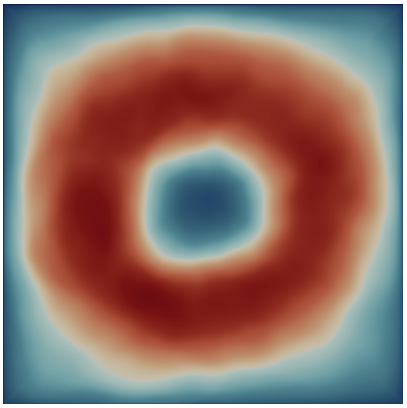

Figure 6.4.8: Mean temperature at x=50mm.

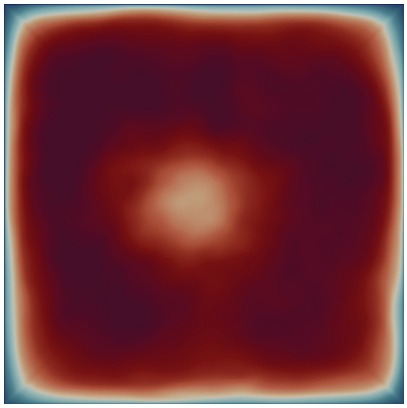

Figure 6.4.9: Mean temperature at x=100mm.

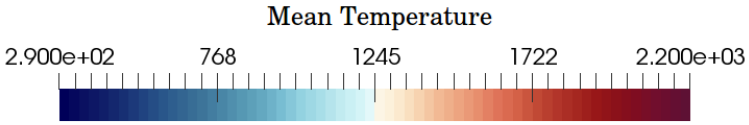

In Figs. 6.4.10, 6.4.11 and 6.4.12 the results for the mean mixture fraction can be found. This gives insight into mixing and the completeness of combustion inside of the chamber. It can be seen that regions of high mixture fraction heap up at the walls. This is because there is lower mixing in these regions of fuel and oxidizer. Again, the progress of combustion in the axial direction can be observed through these 3 figures. At a distance of 5mm large regions of fuel exist due to the heaping up of methane in the recirculation zone of the chamber. This distribution of mixture fraction and consequently the rate of combustion in the chamber was found to have a significant effect on the circumferential distribution of the wall heat flux.

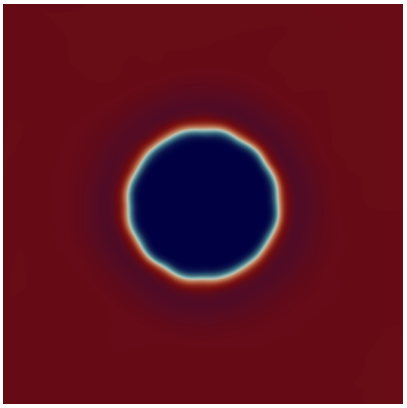

Figure 6.4.10: Mean mixture fraction at x=5mm.

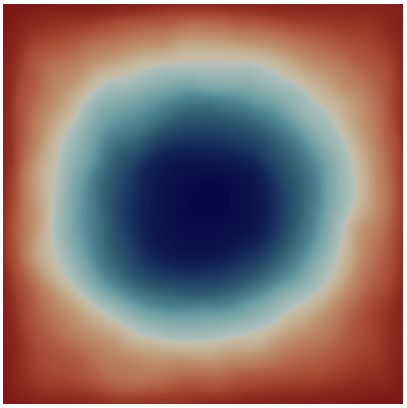

Figure 6.4.11: Mean mixture fraction at x=50mm.

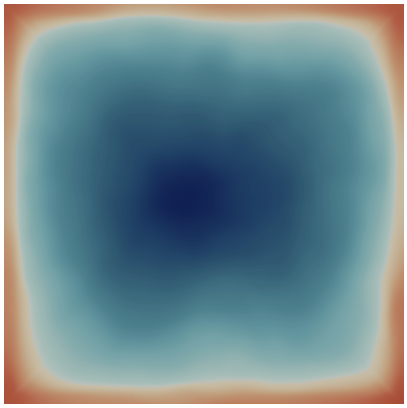

Figure 6.4.12: Mean mixture fraction at x=100mm.

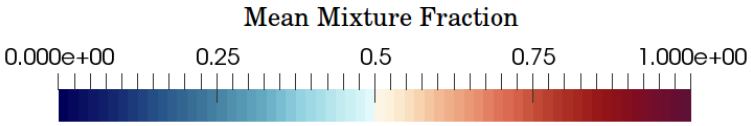

6.4.6 Turbulent Heat Flux

The turbulent heat flux was visualized to analyze the heat distribution due to turbulence. It is defined as $\mathbf{u}'T'$, or the product between the fluctuation of the velocity and the fluctuation of the temperature. It is shown for the fine mesh in Fig. 6.4.13 and for the coarse mesh in Fig. 6.4.14.

The turbulent heat flux is considerably higher for the finest mesh. This is due to two reasons. First of all, the smaller length scale that is being used with the higher resolution simulation leads to more turbulent structures being captured. This results in more fluctuation in the velocity. The higher amount of turbulence in the flow creates more heat distribution due to turbulence structures. Secondly the temperature fluctuation was found to be higher as well for the higher resolution simulation. When recalling the difference in the instantaneous temperature between the fine and coarse mesh in Figs. 6.3.3 and 6.3.4, there is hardly any flame wrinkling or variation in the instantaneous temperature for the coarse. This is reflected in turbulent heat flux for the coarse mesh, where it is practically zero in the inlet area. The higher mixing of the flame is causing in its turn a higher temperature variation.

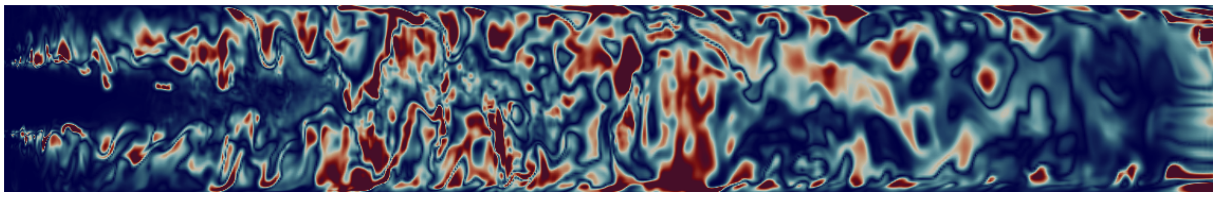

Figure 6.4.13: The turbulent heat flux for the finest mesh.

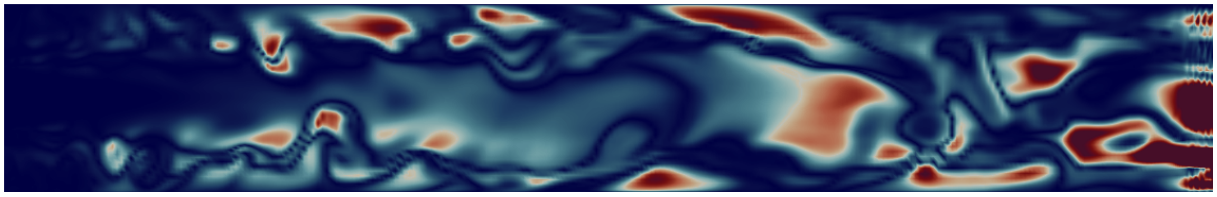

Figure 6.4.14: The turbulent heat flux for the coarsest mesh.

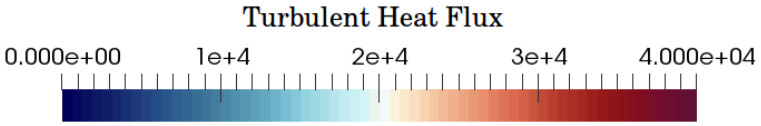

6.4.7 Corner Vortices

Due to the square cross section of the combustion chamber turbulent secondary flows are induced. To visualize this, the velocity surface vectors that are parallel to the cross section are calculated with Paraview. The cross section is taken at an axial distance of 150mm. The result can be found in Fig. 6.4.15. Two symmetry axes can be discerned in the figure, with four locations of higher velocity in the vicinity of the corners. Furthermore, the surface vectors directionally seem to originate from the center of the chamber. Next to this, there is a flow from the center of the chamber towards the corners.

This is due to the fact that the flow experiences inhomogeneous interaction with the chamber walls. The flow is then funneled towards the corners where it is then blocked. Following this, the flow streams out of the corner parallel to the walls. When the flow reaches the midpoint of the chamber wall, it flows towards the center again and the cycle is repeated.

These secondary flows also have an influence on the wall heat flux. This is because of the interaction of the flow with the walls and the high temperature it is carrying due to the ongoing combustion. Lastly, the expansion in the chamber due to combustion is discernible. This increases the temperature and lowers the density. This in turn increases the velocity and accelerates the velocity towards the walls.

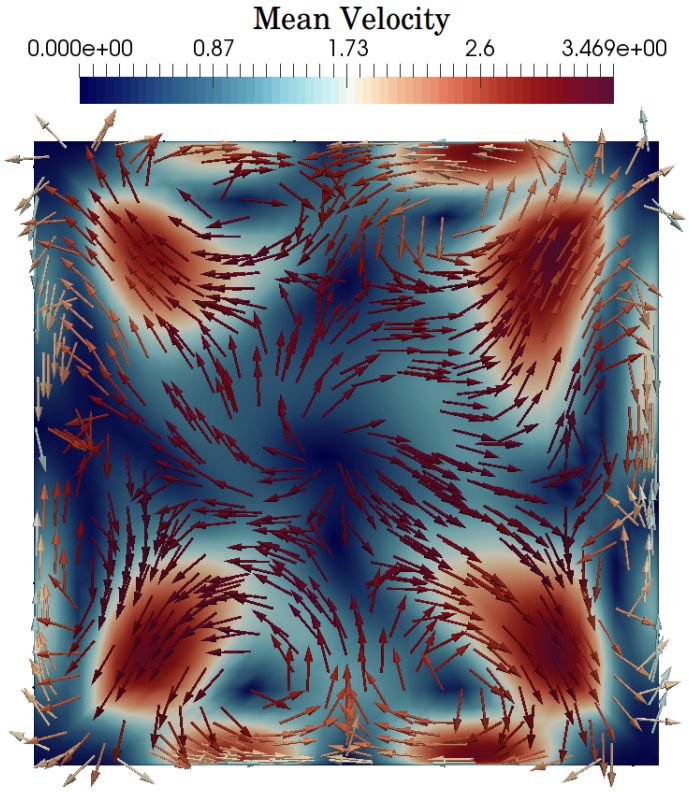

Figure 6.4.15: Visualization of the velocity surface vectors at x=150mm.

What can be seen in Fig. 6.4.16 is the wall heat flux visualized on a part of the chamber between x=145mm and x=155mm. The wall heat flux is the lowest in the corners of the combustion chamber. As seen in Fig. 6.4.9 the temperature is lowest in the corners, this is because the majority of the reaction does not place there. Due to a lower temperature gradient the wall heat flux is consequently lower in the corners. What then can be observed is a peak in the wall heat flux in the upper and lower quartiles of the chamber followed by a reduction in the wall heat flux in the middle of the chamber.

This is due to the turbulent secondary flows which exist because of the square geometry of the chamber. It causes a prolonged interaction of the hot circulating gasses with the chamber walls. This phenomenon allows for a higher wall heat flux at these locations. As the flow moves back into the center of the channel the magnitude of the wall heat flux decreases. Lastly, what can be observed is an absolute increase in wall heat flux in the axial direction. This happens since combustion is developing and more heat is generated.

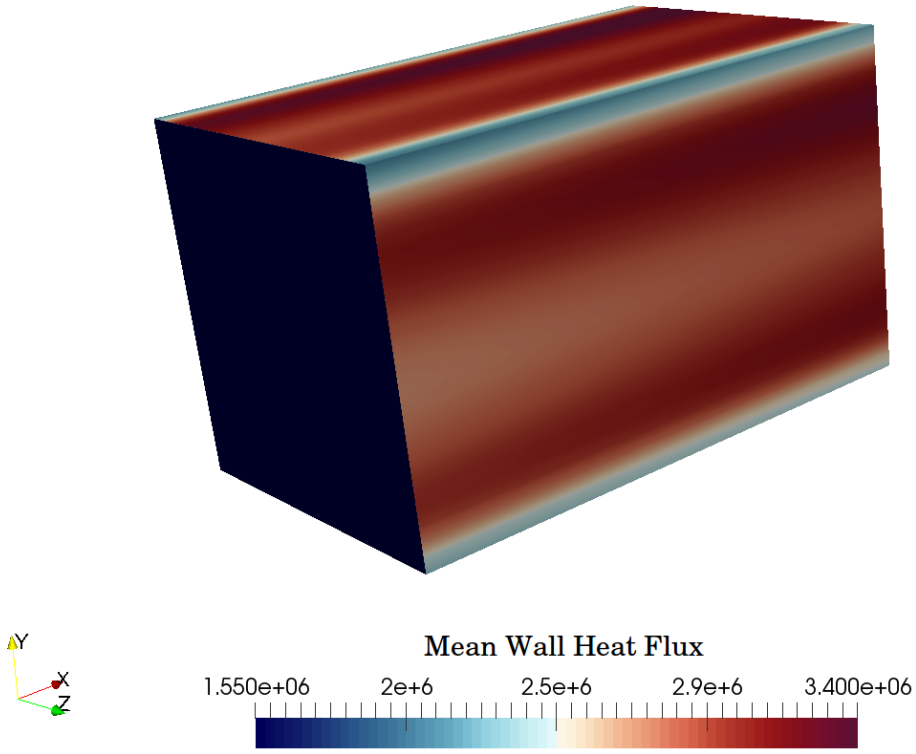

Figure 6.4.16: Wall heat flux visualized on the walls over a section of the chamber.

6.4.8 RANS and LES Content in the Combustion Chamber

As with the testcases, the RANS and LES content was also visualized with the simulations for the combustion chamber. This was done in order to gain knowledge whether RANS and LES content is active in the areas where they should be active. One of the problems with hybrid methods is that when flow comes out of RANS and into LES then there are no turbulent structures yet. Partially wrong results might be obtained. An unwanted switch to LES content in the boundary layer can lead to a reduced eddy viscosity or in the worst case separation induced by this error. The results can be seen in Fig. 6.4.17 and 6.4.18. The images have been scaled by a factor 4 in the axial direction in order to better visualize the results. A value of 1 for the IDDES switching function corresponds to pure LES and 0 to pure RANS. In the figures the instantaneous values of the IDDES switching function have been visualized.

The first thing one notices when looking at the figures is how much smaller the RANS region is for the fine mesh compared to the coarse mesh. Due to the switching mechanism, where the model will switch to LES mode when the grid spacing is smaller than the distance to the wall, smaller cells will lead to more LES areas. This of course leads to a much more accurate solution of the simulation. Furthermore, no unwanted LES content is present inside of the RANS. This means that the grey areas which sometimes plague hybrid methods, where an unwanted switch to LES occurs in RANS areas, have been successfully avoided.

Figure 6.4.17: Visualization of RANS and LES content for the finest mesh.

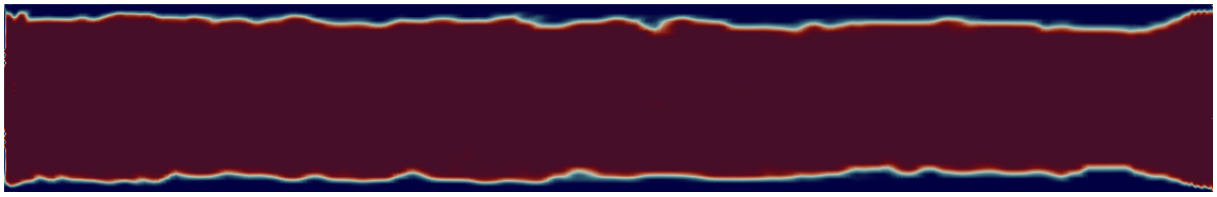

Figure 6.4.18: Visualization of RANS and LES content for the coarsest mesh.

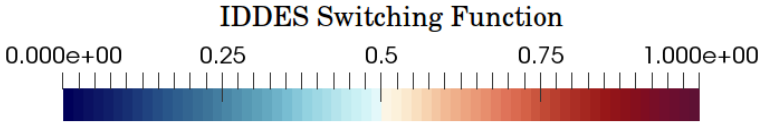

The next step is to visualize the effect on the simulation with the difference in RANS and LES computed solutions. The eddy viscosity was chosen for this because it gives insight in the modeled solution. This has been done in Figs. 6.4.19 and 6.4.20. The direct correspondence between the values for the eddy viscosity and the RANS areas can be seen, especially for the coarse mesh. This is interesting because a higher eddy viscosity will lead to a higher turbulent thermal diffusivity. A higher thermal thermal diffusivity will of course lead to more heat transfer, but the coarser mesh actually displays a lower amount of heat transfer. The most likely explanation is that this increase in heat transfer caused by the increase in eddy viscosity is offset by the better resolution and more complete combustion of the fine mesh. This better resolution of the flame results in higher temperatures and heat transfer, as could also be seen in the figures for the turbulent heat flux.

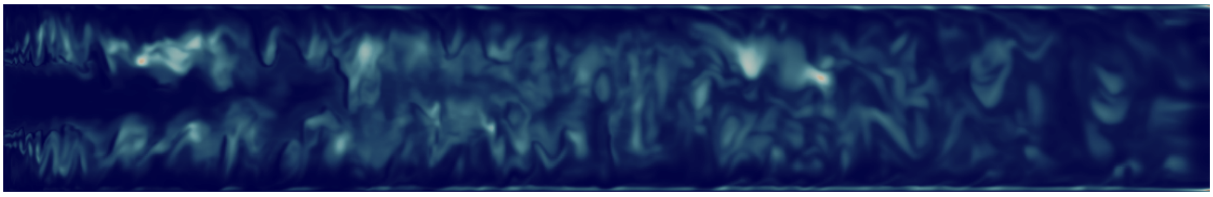

Figure 6.4.19: Visualization of the eddy viscosity for the finest mesh.

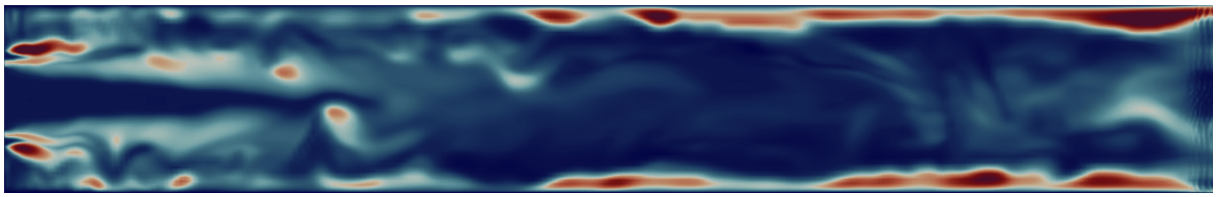

Figure 6.4.20: Visualization of the eddy viscosity for the coarsest mesh.

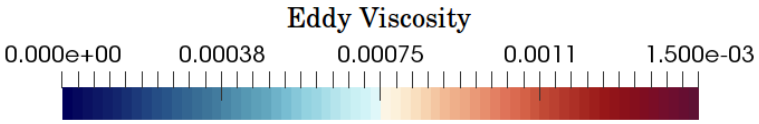

CHAPTER 7

Conclusions and Recommendations

The goal of this thesis was to investigate the accuracy in predicting the pressure and wall heat flux in the BKD-9 combustion chamber. The used turbulence model was the IDDES hybrid method, to model combustion the SLFM was employed. In this section the obtained conclusions and recommendations for the thesis will be reported.

7.1 Conclusions

1. The simulations show an increasing accuracy in predicting the pressure and the wall heat flux with increasing grid refinement. It is concluded that using the hybrid IDDES turbulence model together with the SLFM aproach is a viable option in simulating combustion in the BKD-9 case. The final results do show some underpredictment of the results, but further refinement will improve the prediction of combustion. This improvement takes place in two ways. First, the combustion will be better resolved. The gradients of the flame will be better computed, more of the chemical processes will be resolved and less strain will be placed on the flame, this will lead to higher flame temperatures. Secondly, the turbulence will be resolved more accurately. This will lead to better mixing and higher turbulent heat flux, or heat distribution due to turbulence.

2. The component that impacted the flame temperature the most was the mixture fraction variance. The mixture fraction variance serves as a SGS model in the flamelet approach and is used to model the small scale chemical and reaction processes which occur on a smaller scale than most RANS/LES grids. Due to better resolving of the small scale chemical effects with grid refinement, the flame temperature increased with decreasing mixture fraction variance.

3. The scalar dissipation rate had the second largest impact on the maximum flame temperature. It determines the strain and structure of the flame. The components that have an effect on the scalar dissipation rate are the mixture fraction variance, the IDDES length scale, the effective viscosity and the density. With a lower mixture fraction variance, the gradients of the flame and the strain are decreased. With a smaller IDDES length scale the distance between the oxidizer and the fuel are decreased in the flamelet and the scalar dissipation rate

is increased. With increasing combustion the viscosity is increased, the density is decreased and both lower the scalar dissipation rate slightly.

4. Two recirculation zones exist in the inlet area of the combustion chamber. One exists due to the corner geometry of the chamber, similar to the BFS. The length of this recirculation was to found to become shorter with grid refinement. Two components impacted this length, the mixing of the gasses and the inlet velocity of the injectors. The other recirculation zone existed in between the fuel and oxygen injectors, it existed due to the geometry of the chamber in relation to the injectors.

5. The recirculation zone in between the injectors played a large role in the flame stability. High temperature flow and ignitable products are supplied there by the recirculation zone. Hot products are recirculated and meet fresh reactants. This creates favorable conditions for the ignition of newly injected gasses. The second aspect that impacted the stability was the scalar dissipation rate. With increasing scalar dissipation rates the flame will be strained until combustion is no longer possible and the flame is quenched. It was shown that in this case this was not an issue.

6. It was found that the chemical time scales were small enough compared to the turbulent time scale to result in a enough Damköhler number. This means that the assumption that the flame preserves a laminar shape inside of the turbulent structure holds.

7. It was affirmed that erroneous switching between RANS and LES was successfully avoided in the combustion case. These issues are prone to occur with hybrid methods and can result in incorrect Reynolds stresses. Next to this, heat distribution due to turbulence was shown to increase with grid refinement.

8. The secondary turbulent structures of the flow in the chamber were analyzed. These were generated due to inhomogeneous interaction with the chamber walls. These effects also locally increased the wall heat flux where they interacted with the chamber walls.

9. Analyzing the cross section of the flame showed how the combustion developed in the axial direction. A thermal boundary layer developed at the wall due to enthalpy losses and fuel heaped up in the corners due to low mixing there.

10. While simulating the BFS it was found that grid refinement with a hybrid method was a challenging assignment. This is because with grid refinement the switching location between RANS and LES changes and therefore the whole model for the simulation will be different. Furthermore, abrupt switching might occur because the IDDES has two definitions for the length scale, depending on the cell step size and the distance to the wall.

11. From the HTF case it can be concluded that computing the wall heat flux with OpenFOAM resulted in a wrong amount. Computing it by hand and increasing the time differentiation scheme allowed for the simulation results to accurately approximate the experimental data.

7.2 Recommendations

1. Results could most likely be improved with a better definition for the scalar dissipation rate in RANS computations. When the SA model is used then the necessary length scale could

be based on the distance to the wall or the eddy viscosity.

2. When another definition for the RANS scalar dissipation is used a blending function should be introduced to orchestrate the switching between RANS and LES in the hybrid method. This is important because with hybrid methods some areas have both RANS and LES content. This blending function could be based on the available IDDES blending function.

3. Using the k-omega SST as the RANS model could increase the accuracy of the results. This model is superior to the SA model in predicting flow separation, flow reattachment and high pressure gradients. Unfortunately no tested version was available for use with IDDES. Furthermore, the original formulation for the RANS scalar dissipation uses the turbulent kinetic energy and dissipation rate. So the formulation for the RANS scalar dissipation rate does not have to be rewritten when the SST model is used.

4. It was found at the end of the thesis that the stability of the simulation could be improved by increasing the number of iterations of the pressure-momentum equation in the PIMPLE loop, through nOuterCorrectors. The tolerances for the pressure need to be adjusted then as well so the simulation will not have too much increased computational time. When this is done the order of time discretization can be increased without the simulation crashing. With a higher order time discretization more accurate results will be obtained. This way also the time consuming process of step wise increasing the CN number can be bypassed. Possibly the divergence and gradient schemes can be improved to full second order schemes instead of the limited second order schemes that are being used right now. This should also be investigated.

5. Increasing the mesh resolution will lead to improved results. The simulation underpredicted the results, due to a restriction in cell number. In a previous LES study the WHF was correctly predicted at the inlet, but underpredicted it more downstream. This mesh was already constructed with 90 million cells, compared to the 20 million that are used in this research. As a rough estimation, a factor 10 more cells could be necessary to accurately simulate the BKD-9 case.

6. During the thesis only verification and validation was performed of non-reacting cases. In order to properly identify modeling errors it is recommended to also perform a verification and validation analysis of combustion cases.

7. Handling of simulation cases through OpenFOAM could be more user friendly. Through a user interface it could be quicker to work on simulations and would decrease the chance of errors in the simulation. For example, an option to automatically start averaging the solution after a set time would be welcome.

8. Other models for turbulence and combustion or CFD software could be considered for more accurate results.

9. Further investigation into the interaction between LES and RANS with the hybrid model is recommended. The IDDES method is quite complex and finding out the modeling errors is very challenging. Further points that should be investigated are the interaction between RANS and LES during grid refinement and the computed turbulence properties in grey areas.

Bibliography

[1] Frei, W., "Which Turbulence Model Should I Choose for My CFD Application?" *COMSOL*, 2017, `https://www.comsol.com`, Visited 4/1/18.

[2] Dongue, D., "LES Turbulence Models in CFD," *Dongue Fluid Science*, 2017, `http://dyfluid.com/LES.html`, Visited 4/12/17.

[3] Hickel, S., "Lecture Notes on Course: CFD for Aerospace Engineers," *TU Delft*, 2017.

[4] de Villiers, E., "The Potential of Large Eddy Simulations for the Modeling of Wall Bounded Flows," *PhD Thesis, Imperial College*, 2006.

[5] Spalart, P. R., Deck, S., Shur, M. L., Squires, K. D., Strelets, M. K., and Travin, A., "A new version of detached-eddy simulation, resistant to ambiguous grid densities," *Theor. Comput. Fluid Dyn., Pages 181–195*, 2006.

[6] Shur, M. L., Spalart, P. R., Strelets, M. K., Deck, S., and Travin, A., "A hybrid RANS-LES approach with delayed-DES and wall-modelled LES capabilities," *International Journal of Heat and Flow, Pages 1638-1649*, 2008.

[7] Piomelli, U., Balaras, E., Pasinato, H., Squires, K. D., and Spalart, S., "The inner–outer layer interface in large-eddy simulations with wall-layer models," *International Journal of Heat and Fluid Flow, Pages 538-550*, 2003.

[8] Piomelli, U. and Balaras, E., "Wall Layer Models For Large Eddy Simulation," *Annu. Rev. Fluid Mech,Pages 437-446*, 2002.

[9] ANSYS, "Ansys CFX-solver Theory Guide. Ansys CFX Release 11.0," *ANSYS Europe*, 2006.

[10] Mueller, H., Ferraro, F., and Pfitzner, M., "Implementation of a Steady Laminar Flamelet Model for non-premixed combustion in LES and RANS simulations," *International OpenFOAM Workshop, South Korea*, 2013.

[11] Zhang, L., Zhao, G., Dong, G., Li, S., and Wang, G., "Bubble morphological evolution and surface defect formation mechanism in the microcellular foam injection molding process," *Royal Society of Chemistry Advances, Pages 70032–70050*, 2017.

[12] Christian, M., "Time-resolved measurement and simulation of local scale turbulent urban flow." *PhD Thesis ETH Zurich*, 2016.

[13] Celano, M. P., Silvestri, S., Schlieben, G., Kirchberger, C., Haidn, O. J., Dawson, T., Ranjan, R., and Menon, S., "Experimental and numerical investigation of GOX-GCH4 shear-coaxial injector element," *Space Propulsion Conference, Cologne*, 2014.

[14] Rumsey, C., "Backwards Facing Step," *NASA Turbulence Modeling Resource*, 2012, `https://turbmodels.larc.nasa.gov/backstep_val.html`, Visited 1/3/17.

[15] Kawamura, H., Abe, H., and Shingai, K., "DNS of turbulence and heat transport in a channel flow with different Reynolds and Prandtl numbers and boundary conditions," *3RD CED Int. Symp. on Turbulence, Heat and Mass Transfer*, 2000.

[16] Batchelor, G., *An Introduction to Fluid Dynamics*, ISBN 0-521-66396-2, Cambridge University Press, Cambridge, UK, 1967.

[17] Spalart, P. R. and Allmaras, S. R., "A One-Equation Turbulence Model for Aerodynamic Flows," *30th Aerospace Sciences Meeting and Exhibit Reno, NV, U.S.A.*, 1992.

[18] Zhiyin, Y., "Large-Eddy Simulation: Past, present and the future," *Chinese Journal of Aeronautics, Pages 11-24*, 2014.

[19] Spalart, P. R., Jou, W. H., Strelets, M., and Allmaras, S. R., "Comments on the feasibility of LES for wings and on a hybrid RANS/LES approach," *Conference: Advances in DNS/LES: Direct numerical simulation and large eddy simulation, Ruston, LA, U.S.A*, 1997.

[20] Menter, F. and Kuntz, M., "Adaptation of eddy-viscosity turbulence models to unsteady separated flow behind vehicles," *From Book: The Aerodynamics of Heavy Vehicles: Trucks, Buses, and Trains, Pages 339-352*, 2004.

[21] Hamba, F., "Log-layer mismatch and commutation error in hybrid RANS/LES simulation of channel flow," *International Journal of Heat and Fluid Flow, Pages 20-31*, 2009.

[22] Peters, N., *Turbulent Combustion*, ISBN 9780511612701, Cambridge University Press, Cambridge, 2000.

[23] Greenshields, C. J., "OpenFOAM User Guide," *OpenFOAM Foundation Ltd*, 2016.

[24] Crank, J. and Nicolson, P., "A practical method for numerical evaluation of solutions of partial differential equations of the heat conduction type," *Proc. Camb. Phil. Soc.*, 1947.

[25] Nilsson, H., "A pimpleFoam tutorial for channel flow with respect to different LES models," *Chalmers University CFD Course*, 2011.

[26] Chemnitz, A., Sattelmayer, T., Roth, C., Haidn, O., Daimon, Y., Keller, R., Gerlinger, P., Zips, J., and Pfitzner, M., "Numerical Investigation of Flow and Combustion in a Single-Element GCH4/GOX Rocket Combustor: Aspects of Turbulence Modeling," *52nd AIAA/SAE/ASEE Joint Propulsion Conference*, 2016.

[27] Müller, H., Zips, J., Pfitzner, M., Maestro, D., Cuenot, B., Selle, L., Ranjan, R., Tudisco, P., and Menon, S., "Numerical Investigation of Flow and Combustion in a Single-Element GCH4 /GOX Rocket Combustor: A comparative LES study," *52nd AIAA/SAE/ASEE Joint Propulsion Conference*, 2016.

[28] NIST, "NIST Chemistry WebBook, SRD 69," *U.S. Department of Commerce*, 2017, `http://webbook.nist.gov/chemistry/fluid/`, Visited 4/1/18.

[29] Isaac, B. J., Parente, A., Galleti, C., Thornokc, J. N., Smith, P., and Tognotti, L., "A Novel Methodology for Chemical Time Scale Evaluation with Detailed Chemical Reaction Kinetics," *American Chemical Society, Energy and Fuels, Pages 2255–2265,*, 2013.

[30] Ivancic, B. and Mayer, W., "Time- and Length Scales of Combustion in Liquid Rocket Thrust Chambers," *Journal of Propulsion and Power, Pages 247-253*, 2002.

[31] Prüfert, U., Hunger, F., and Hasse, C., "The analysis of chemical time scales in a partial oxidation flame," *Combustion and Flame*, 2014.